UNIVERSITY OF CALIFORNIA

Los Angeles

Multi-Height-Based Lensfree On-Chip Microscopy for Biomedical Applications

A dissertation submitted in partial satisfaction of the requirements for the degree Doctor of Philosophy in Electrical Engineering

by

Alon Grinbaum

2014

© Copyright by

Alon Grinbaum

2014

ABSTRACT OF THE DISSERTATION

Multi-Height-Based Lensfree On-Chip Microscopy for

Biomedical Applications

By

Alon Grinbaum

Doctor of Philosophy in Electrical Engineering

University of California, Los Angeles, 2014

Professor Aydogan Ozcan, Chair

Computational resources are constantly becoming faster, cheaper and more portable. Coupled with mass production and the use of sophisticated hardware components in the consumer electronics market, the abundance of computational power opens numerous opportunities in reducing the cost and extending the capabilities of traditional biomedical imaging and sensing devices. Toward this end, myriad computational imaging methods have been devised; among them is lensfree holographic imaging that provides a portable, cost-effective and yet powerful alternative to traditional bright field microscopy tools. Additionally, lensfree microscopy provides significantly larger fields-of-view (e.g., 30mm^2) when compared to a typical bright-field transmission microscope with comparable resolution (e.g., 60-100× objective lens with a numerical aperture of 0.8-1.0).

This dissertation introduces the unique architecture of lensfree on-chip microscopy, its computational reconstruction methods, and several biomedical-imaging applications that utilize on-chip imaging. Lensfree microscopy has a distinct architecture when compared to other imaging systems. First, rather than recording a direct image of the specimen, an on-chip in-line hologram is acquired. In addition, the sample is positioned in close proximity to the image sensor (typically sub-mm); and finally, lenses are not used between the object and the image sensor. These unique attributes enable the simplification of the microscope's hardware to solely an image sensor and a partially coherent light source (both temporally and spatially), thus resulting in a cost-effective and portable microscope where hardware is replaced with computational reconstruction methods. These computational methods can push the resolution of the on-chip microscope to a deeply sub-micron range (e.g., 225 nm) by employing pixel-super-resolution, a method that synthesizes one high-resolution image from various lower resolution images of the same object. Additionally, to image dense and confluent samples, multi-height-based phase-recovery is introduced in partially coherent holography. This iterative method recovers the lost phase of an optical field from few intensity measurements, each captured with a different sample-to-sensor distance. Lastly, to provide accurate colorization, especially challenging for holographic methods, two different algorithms are utilized, one based on Dijkstra's shortest path algorithm, and the other based on the YUV color space. Based on these computational reconstruction blocks, the performance of lensfree on-chip microscopy can be demonstrated in various biomedical imaging applications that require both high-resolution and high-throughput, including Papanicolaou smears, human breast cancer slides and sickle cell anemia blood smears.

The dissertation of Alon Grinbaum is approved.

Bahram Jalali

Oscar M. Stafsudd

Dino Di Carlo

Aydogan Ozcan, Committee Chair

University of California, Los Angeles

2014

Table of Contents

Chapter 1 Introduction to lensfree on-chip imaging 1

1.1 Key components of a lensfree holographic on-chip microscope 3

1.2 Reconstruction techniques 5

1.3 Gigapixel imaging using lensfree on-chip microscopes 7

1.4 Future challenges and opportunities for lensfree on-chip microscopes 10

Chapter 2 Improving spatial resolution in lensfree imaging 18

2.1 Introduction 18

2.2 Results 21

2.3 Discussion 28

2.4 Theory and methods 30

Chapter 3 Imaging dense specimen using lensfree on-chip holographic microscopy 38

3.1 Introduction 38

3.2 Results 39

3.3 Discussion 48

3.4 Theory and methods 50

Chapter 4 Lensfree color imaging 57

4.1 Introduction 57

4.2 Results 61

4.3 Discussion 64

4.4 Theory and methods 68

Chapter 5 Imaging of pathology slides using lensfree microscopy 72

5.1 Introduction 72

5.2 Results 75
5.3 Discussion 80
5.4 Theory and methods 88
Chapter 6 Field-portable pixel super-resolution color microscope 94
6.1 Introduction 94
6.2 The design of a field-portable color lensfree microscope 96
6.3 Results 98
6.4 Discussion 100
Chapter 7 Conclusions 104

Acknowledgements

First and foremost I would like to thank Prof. Aydogan Ozcan, for his absolute dedication, invaluable mentorship, great enthusiasm and support. I feel very fortunate to have had the opportunity to learn from Prof. Ozcan, and be part of his flourishing laboratory. I am extremely grateful to work under such a unique scholar, whose open mindedness, creativity and charisma were utterly inspiring and instrumental to my professional development. Additionally, I would like to thank my doctoral committee members, Prof. Dino Di Carlo, Prof. Bahram Jalali, and Prof. Oscar Stafsudd, for their support.

I would like to acknowledge Prof. Yael Hanein, my previous advisor, whose guidance and wisdom well equipped me for this journey. I highly value Prof. Hanein's ongoing support and mentorship.

A special thanks to my colleagues and extraordinary lab members, whose camaraderie played a significant role in this process. Working with Hongying Zhu, Euan McLeod, Derek Tseng, Onur Mudanyali, Serhan O. Isikman, Justin Su, Bahar Khademhosseini, Ikbal Sencan, Waheb Bishara, Gabriel Biener, Myungjun Lee, Wei Luo, Zoltan Gorocs, Sam Mavandadi, Liang Xue, Uzair Sikora, Qingshan Wei, Hatice C. Koydemir, Ertan Salik, Yujing Qian, Yan Lok Chan, Shouyu Wang, Alborz Feizi, Yibo Zhang, Ping-Luen Chung, Mustafa Uğur Daloğlu, Umut Dincer, Najva Akbari, Michael Wu, Steve Feng and Jose C. Contreras-Naranjo, has been a great experience.

Last but not least, I would like to thank my wonderful family for their unconditional love and support; to my amazing wife Nelly, my parents, and my brothers, Lior and Chen.

Vita

Alon Greenbaum holds his BS and MS degrees in Electrical Engineering (EE) from Tel Aviv University, Israel. In 2010, he started pursuing a Ph.D. degree in EE at the University of California, Los Angeles (UCLA), where he conducts biophotonics research under Prof. Aydogan Ozcan. His research focuses on high-resolution and high-throughput microscopy for biomedical applications. Alon has received several prestigious awards and fellowships, including the Howard Hughes Medical Institute (HHMI) International Student Research Fellowship and the SPIE Optics and Photonics Education Scholarship. He has authored or co-authored more than twenty-five peer reviewed research articles in major journals and conferences.

Selected Publications

1. Greenbaum, A., Sikora, U. & Ozcan, A. Field-portable wide-field microscopy of dense samples using multi-height pixel super-resolution based lensfree imaging. *Lab Chip* **12,** 1242–1245 (2012).
2. Greenbaum, A. *et al.* Imaging without lenses: achievements and remaining challenges of wide-field on-chip microscopy. *Nat Meth* **9,** 889–895 (2012).
3. Greenbaum, A. *et al.* Increased space-bandwidth product in pixel super-resolved lensfree on-chip microscopy. *Sci. Rep.* **3,** 1717 (2013).
4. Greenbaum, A. & Ozcan, A. Maskless imaging of dense samples using pixel super-resolution based multi-height lensfree on-chip microscopy. *Optics Express* **20**, 3129-3143 (2012).
5. Greenbaum, A., Feizi, A., Akbari, N. & Ozcan, A. Wide-field computational color imaging using pixel super-resolved on-chip microscopy. *Optics Express* **21**, 12469-12483 (2013).
6. Greenbaum, A., Akbari, N., Feizi, A., Luo, W. & Ozcan, A. Field-portable pixel super-resolution colour microscope. *PLoS ONE* **8,** e76475 (2013).
7. Mudanyali, O. *et al.* Wide-field optical detection of nanoparticles using on-chip microscopy and self-assembled nanolenses. *Nat Photon* **7,** 247–254 (2013).

Chapter 1 Introduction to lensfree on-chip imaging

Parts of this chapter have previously been published in Greenbaum, A. *et al.* Imaging without lenses: achievements and remaining challenges of wide-field on-chip microscopy. *Nat Meth* **9,** 889–895 (2012).

Lensfree on-chip imaging refers to using a digital opto-electronic sensor array, such as a CCD or CMOS chip to directly sample the light transmitted through a specimen without the use of any imaging lenses between the object and the sensor planes[1–25]. Such an imaging geometry is significantly simpler in hardware and much more compact and light-weight than conventional lens-based microscopes. In addition, this geometry, as will be detailed later on, can decouple imaging field-of-view (FOV) and resolution from each other, creating unique microscopes where improved resolution and FOV can be achieved at the same time with new sensor chips that are being introduced in consumer electronics products, in particular cellphones and high-end digital cameras.

For a lensfree on-chip microscope there are various design choices that one can select from. Leaving the discussion of lensfree fluorescent on-chip imaging techniques[26–29] to next sections, in general we can categorize bright-field lensfree microscopes into two main streams: (1) contact mode shadow imaging based microscopes[16–19]; and (2) diffraction based lensfree microscopes[1–15]. The first group of lensfree microscopes aims to minimize the distance between the sample and the active region of the sensor array (or an aperture array in some cases[16,17]) so that diffraction can be significantly reduced. Therefore these contact mode lensfree optical microscopes sample the transmitted light through the objects that are placed on a sensor-array, effectively capturing the shadows of the objects. Under the assumption that optical diffraction within the object body

and between the object and the sensor active region can both be ignored, these object shadows represent 2D images of the specimens. To mitigate pixelation related artifacts in digital sampling of these transmission shadow images, earlier designs of such lensfree microscopes utilized the motion of the specimens within e.g., a micro-fluidic channel, so that a smaller effective pixel size can be created from a time sequence of shadow images, improving the spatial resolution[16,17]. For stationary or slowly moving samples on a chip, however, source-shifting[6,7] can be utilized to digitally control the movement of these lensfree object shadows on the sensor-array as a function of the source position, also leading to the synthesis of higher resolution shadow images[20].

On the other hand, the second category of lensfree microscopes relies on computation (based on e.g., digital holography[1–15] or coherent diffractive imaging techniques[30–35]) to partially undo the effects of diffraction that occurs between the object and the detector planes. Therefore, unlike contact mode shadow imaging approaches, a sizeable distance between the objects and the sensor chip can be accommodated, which also permits imaging of large sample volumes. In this second group of lensfree microscopes, the scattered light from each object interferes with itself and with the unscattered background light (if it exists) to create an interference pattern, which is then digitally processed to reconstruct an image of the object[1–8,10–14,36–41].

In this chapter, I will expand on lensfree holographic microscope designs, some of which use a spatially and temporally coherent light source such as a laser that is filtered by a small pinhole (e.g., ≤1-2μm)[1–4], while some others rely on partially-coherent illumination provided by e.g., light-emitting-diodes (LEDs)[5–11,42]. More specifically, I will focus on the latter and present the unique features of such partially-coherent lensfree optical microscopy tools that operate under unit magnification, where the sample is “on-chip” (see Fig. 1.1) and report some of the emerging results that they provide for wide-field imaging needs, achieving e.g., an numerical aperture (NA)

of ~0.8-0.9 with a half-pitch resolution of ~300-350 nm across an FOV of >20 mm^2 (i.e., >5 mm × 4 mm) or an NA of ~0.1 across an FOV of ~18 cm^2 (~4.9 cm × 3.7 cm), corresponding to an image with more than 1.5 billion useful pixels. I will also present some of the current challenges that these computational on-chip microscopes face, and compare different approaches to shed more light on their future directions and applications.

1.1 Key components of a lensfree holographic on-chip microscope

In a partially-coherent holographic on-chip microscope (Fig. 1.1) the source can simply be an LED or an array of LEDs[5,7,24]. In case wavelength tunability is desired, a monochromator can also be used that is coupled to e.g., a multi-mode fiber. The spectral bandwidth of the source can vary between a few nanometers to e.g., 20-30 nm depending on the sample-to-detector distance and the resolution requirement of the system. Because the sample plane is rather close to the detector plane (e.g., ≤0.1-2 mm), the scattered light rays and the background light can still interfere at the sensor chip, even though the temporal coherence lengths of such broadband sources are significantly shorter compared to e.g., a laser.

In addition to temporal coherence requirements, spatial coherence of the illumination is also critical in lensfree holographic microscopy (which is also true for contact imaging as will be detailed later on). Under unit fringe magnification, since the lensfree holographic shadows of objects do not spread across the entire sensor active area, the spatial coherence diameter that is required at the sampling plane is significantly smaller[5]. This implies that an LED can simply be butt-coupled to a large-core fiber-optic cable or a simple pinhole (e.g., 50-100 μm in diameter) without the use of any mechanical alignment stage or light-coupling optics. This makes alignment and operation of a partially-coherent lensfree holographic microscope straight-forward. Since coherence is now used as a gating function, this choice of partial-coherence, besides

simplicity of alignment and cost-effectiveness, also helps us reduce speckle and multiple reflection interference noise terms as well as cross-interference among the diffraction patterns of objects, which is in general a source of artifact for holography[43].

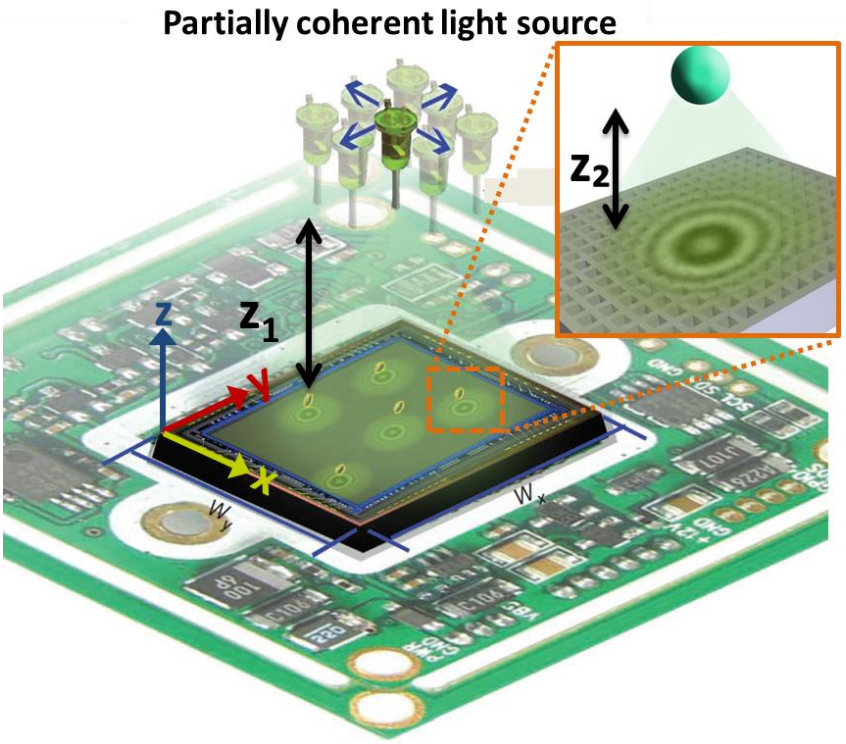


Figure 1.1 Partially coherent lensfree on-chip microscope. Schematic diagram of a partially coherent lensfree transmission microscope that operates under unit magnification, such that the active area of the imager chip (for example, a CCD or CMOS sensor array) is the same as the object FOV.

Apart from the illumination end, the other key component involved in a lensfree holographic microscope is the opto-electronic sensor array that is used to sample the transmitted light pattern from each specimen. Under unit magnification, the imaging FOV of a lensfree microscope is equal to the active area of the sensor chip, which implies that using state-of-the-art CCD and CMOS chips (monochrome or color) one can achieve a wide range of FOVs varying from e.g.,

20 mm^2 to >15 cm^2. These numbers constitute significantly wider imaging areas compared to what standard objective-lenses employed in conventional optical microscopes offer.

In addition to the FOV or active area of the sensor chip, another key feature is the pixel size, which directly influences the spatial resolution that can be achieved. For both holographic and contact mode lensfree on-chip imaging techniques, a smaller pixel size will in general help us achieve better resolution, unless the pixel design exhibits severe angular distortions that create aberrations for oblique rays, corresponding to high numerical apertures. Since the area of the pixel shrinks with the square of its size, to claim a large active area or imaging FOV, more megapixels would also be needed for an ideal lensfree on-chip microscope. Fortunately, adding more megapixels to image sensors is already a major trend in consumer electronics, mostly driven by the massive volume of camera-phones, which are now employing ~40 megapixel imagers.

1.2 Reconstruction techniques

For lensfree on-chip imaging in general there are two important reconstruction blocks that are needed to visualize an object's image. The first one of these computational blocks, termed "pixel super-resolution[44–46]", is used to overcome the resolution limitation due to the pixel size and is required to achieve sub-pixel spatial resolution in lensfree on-chip imaging[6–9]. Note that the term "pixel super-resolution" refers to "de-aliasing" that is used to mitigate the unit magnification of on-chip imaging geometry and should not be confused with the recent literature on beating the diffraction limit of light. Contact mode and holographic lensfree microscopes share this common step to digitally embed more pixels to an image by e.g., shifting the light source and capturing multiple (typically ~10-100) sub-pixel shifted lensfree images of the same static object[6,7]. Alternatively, the motion of the object within, e.g., micro-fluidic devices can also

be used for the same pixel super-resolution step to resolve finer features of an object[8,12,19]. The technical implementation of pixel super-resolution will be detailed in Chapter 2.

The second reconstruction block, which follows the "pixel super-resolution" step, is only required for diffraction based lensfree microscopes, where there is a considerable distance between the objects and the detector array, such that diffraction cannot be ignored at optical frequencies. In this second computation step, the image of the specimen can be reconstructed from its super-resolved interference pattern by employing e.g., iterative phase reconstruction[47] or twin-image elimination algorithms[48] that are commonly used in digital holography literature, as well as other reconstruction algorithms borrowed from e.g., coherent diffraction imaging techniques[36–41]. As a result of this step, both amplitude and phase images of the object can be generated, where the latter might be especially important to image weakly scattering transparent specimens such as sub-micron bacteria or parasites[7]. I will elaborate on iterative phase-recovery methods in Chapter 3.

On the top of these reconstruction blocks, lensfree on-chip microscopy can also employ additional computational tools to move from 2D cross-sectional images to a lensfree tomogram of the object by e.g., merging the spatial frequency information of different illumination angles[12,25,49]. Here we should emphasize that the ability of lensfree in-line holography to digitally propagate a field over a long depth of focus does not immediately permit 3D imaging of objects unless e.g., multi-angle illumination[25], ptychographic tomography[50], or a compressive holography[13,51] based approach is employed.

Note also that such computational blocks are not needed for a conventional lens-based microscope, which can provide immediate visualization of specimen through e.g., the eye-piece. While this can be considered an important limitation of computational microscopy tools in

certain settings, the recent advances in micro-processors such as graphics processing units (GPUs) that are now appearing even on our cellphones make computation extremely cost-effective and widely accessible globally, which we believe would be a key enabler for lensfree imaging techniques to scale up.

1.3 Gigapixel imaging using lensfree on-chip microscopes

After going over some of the basic features of lensfree on-chip microscopes in general, next I would like to give examples of their state-of-the-art performance; the technical implementation will be discussed in Chapter 2. Lensfree computational microscopy permits imaging at an exceedingly large space-bandwidth product, corresponding to a reconstructed image with e.g., more than 1 gigapixels. Using for instance a state-of-the-art CCD enables imaging an ultra-wide FOV of ~18 cm^2 (~4.9 cm × 3.7 cm) with a half-pitch resolution of ~2.19 μm, which contains >1.5 billion useful pixels, assuming 2 pixels define the minimum feature size (see Fig. 1.2). In this case, the monochrome CCD chip itself (Kodak, KAF-39000) has ~40 megapixels, where each pixel is physically 6.8 μm wide. However, by employing pixel super-resolution, a deeply sub-pixel resolution corresponding to an NA of ~0.1 can be achieved across the entire active area of the CCD chip (i.e., an FOV of ~18 cm^2 – Fig. 1.2). In comparison, a conventional objective-lens with a similar NA would typically have an FOV that is a few square millimeters. While a customized microscope lens design based on conventional optics[52] and/or mechanical scanning of the sample or the lens could be used to enlarge the FOV, it would be a relatively complicated and costly solution to achieve such a wide imaging area. On the other extreme, using a state-of-the-art CMOS chip, instead of a CCD, enables achieving <350 nm half-pitch resolution in air (illumination wavelength: 530 nm) across an FOV of ~20.5 mm^2 (i.e., ~5.21 mm × 3.94 mm). In this case (Fig. 1.3), the CMOS chip (from Sony Corp.) is a 16 megapixel color (RGB) sensor

with a pixel size of ~1.1 μm that is manufactured to be used in e.g., cellphone cameras. Once again, using pixel super-resolution (only for the green pixels of the color CMOS chip) enables achieving deeply sub-pixel resolution, corresponding to an NA of ~0.8 (in air) across the entire active area of the CMOS sensor chip (i.e., FOV > 20 mm^2 – see Fig. 1.3).

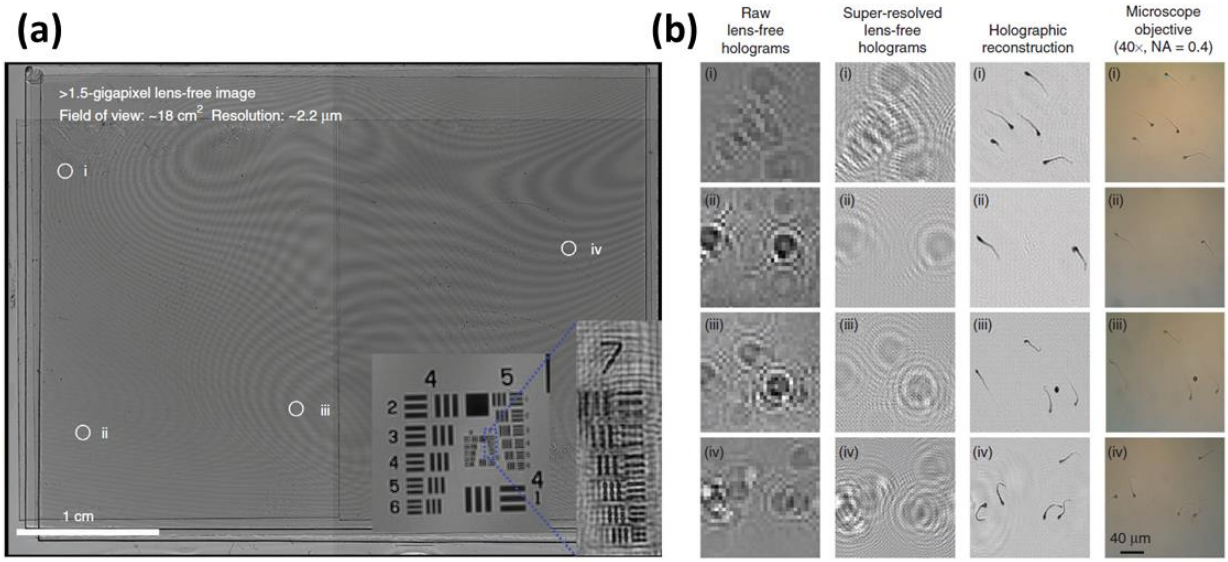


Figure 1.2 Lensfree gigapixel imaging using a CCD sensor chip. **(a)** A super-resolved lensfree image obtained by a partially coherent holographic on-chip imaging platform with a FOV of ~18 cm^2 (~4.9 cm × 3.7 cm) and >1.5 billion pixels. The inset images show a lensfree hologram and its reconstruction results for a resolution target (USAF 1951 test chart) to demonstrate a half-pitch resolution of ~2.19 μm corresponding to an NA of ~0.1. **(b)** Four selected areas of interest (corresponding to the circles and roman numerals in (a)) shown at higher magnification. The first column shows raw lensfree holograms of human sperm (immobilized on a glass slide[9]). Because the physical pixel size of this monochrome CCD chip is 6.8 μm, severe undersampling of holograms is observed. The second column shows the pixel super-resolved lensfree holograms for the same regions, which are digitally synthesized by combining 36 (6 × 6) subpixel-shifted raw lensfree holograms. The third column illustrates the reconstruction results for these pixel super-resolved lensfree holograms. The fourth column shows the same region imaged with a conventional microscope.

One of the most unique aspects of lensfree computational on-chip imaging is the fact that these quoted numbers will immediately improve as new sensor arrays become available. The rapid advancement that we experience in sensor array technologies is driven mostly by the cellphone and digital camera manufacturers, which produce more than 1 billion new camera

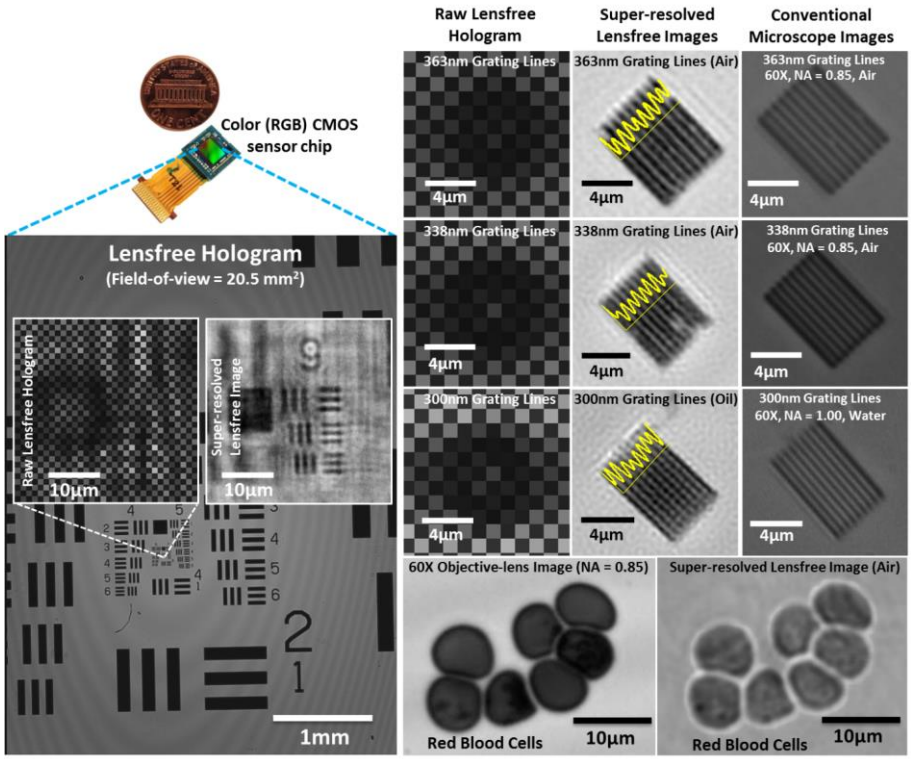


Figure 1.3 Partially-coherent lensfree imaging results using a color RGB CMOS sensor chip (16 megapixel, 1.12 μm pixel size) are summarized and compared against conventional objective lenses (0.85 NA and 1.00 NA). This lensfree imaging platform achieves an NA of ~0.8 (in air) together with a half-pitch resolution of <350 nm over an FOV of ~20.5 mm^2 (~5.21 mm × 3.94 mm). Using oil-immersion between the sample and the sensor-array, a half-pitch resolution of ~300 nm is also achieved, corresponding to an effective NA of ~0.9 (illumination wavelength: 530 nm). Note that the raw lensfree holograms exhibit the Bayer pattern of the color CMOS sensor, where only the green pixels were used in our image reconstructions. Pixel super-resolved images of human red blood cells, a USAF 1951 Test Chart and custom fabricated gratings (milled onto a glass substrate using Focused Ion Beam - FIB) are shown to demonstrate the imaging performance of this lensfree on-chip microscope. We employed up to 100 (10 × 10) sub-pixel shifted raw lensfree holograms in these pixel super-resolution results.

modules every year, placing lensfree on-chip microscopy on a sweet spot to follow this trend. Equally important is that the imaging geometry of Fig. 1.1 decouples spatial resolution from FOV. Stated differently, as more megapixels are introduced onto the same chip, while keeping the pixel size the same (*or even smaller*), we can achieve a larger FOV without sacrificing resolution (*or keep the same FOV with improved resolution*). Therefore, the current trend in image sensor industry toward smaller pixel size and larger megapixel imager chips will continue to improve the resolution and FOV of such lensfree computational microscopes providing us a unique on-chip microscopy platform, where the resolution and FOV are *not* necessarily tied to each other.

1.4 Future challenges and opportunities for lensfree on-chip microscopes

Resolving micro-scale features of specimen in both space and time, lensfree on-chip microscopes could impact almost all the fields that their conventional lens-based counterparts are used, including imaging, screening and tracking of cells and other micro-organisms for various applications ranging from high-throughput screening to lab-on-a-chip technologies[5–11,18,53]. Since conventional wide-field optical microscopy has itself gone through a renaissance over the last two decades, an extensive comparison between lensfree on-chip microscopy tools and conventional lens-based optical microscopes would need to be rather detailed to be fair. However, one can in general highlight: (*i*) decoupling of FOV from resolution, which enables the space-bandwidth product of the on-chip microscope to 'easily' scale up with rapid advancements in opto-electronic sensor-array technologies; (*ii*) larger FOV and depth-of-field for 3D screening of enlarged volumes; (*iii*) compactness and lighter weight which lead to e.g., better integration with lab-on-a-chip platforms; and (*iv*) design simplicity and cost-effectiveness as some of the important features and relative advantages of on-chip microscopes over their conventional lens-

based counterparts. On the other hand, compared to conventional microscopy, there are still several key challenges that lensfree on-chip microscopy faces, such as limited spatial resolution, difficulty in imaging fluorescent and thick specimens, or lack of standardized computational tools, 'practically' limiting the reconstruction and image visualization times. To further improve the performance of on-chip microscopy and widen its application areas, such remaining challenges will need to be addressed, which I will discuss next.

Spatial Resolution: Despite their large imaging areas, the state-of-the-art resolution for lensfree on-chip microscopy is still not diffraction limited. Improving the numerical aperture from its current level of e.g., ~0.8 to 1 or even higher could potentially be achieved using higher index liquids (e.g., oil-immersion[1]) filling in air gaps between the object and detector planes to increase the spatial frequency pass-band of the system. As a matter of fact, Fig 1.3 illustrates that based on this oil-immersion idea and a 1.1 μm CMOS imager, one can improve the numerical aperture to ~0.9, corresponding to a half-pitch resolution of ~300 nm under an illumination wavelength of 530 nm.

Further resolution improvements would probably necessitate new sensor chips that have sub-micron pixel sizes. While this seems to be on the horizon especially with the next-generation CMOS imager chips, an important factor that is less demanding for main-stream use of sensor arrays (e.g., in digital cameras) is angular distortion of pixels. At high numerical apertures, the pixels of a sensor array would typically exhibit artifacts since oblique light rays would experience much higher losses (as a function of e.g., angle) and more importantly could end up generating a signal in neighboring pixels, which would distort accurate sampling of lensfree transmission patterns. Therefore, special attention has to be given to the design of lensfree imager chips in terms of their angular response, which is not as critical for cellphone camera

applications due to the presence and the lower NA of the imaging lens. To reduce pixel related imaging aberrations and get closer to the diffraction limit, new sensor chips that have sub-micron pixel size and a decent external quantum efficiency which is not a strong function of illumination angle are needed.

In addition to these, new signal processing approaches that rely on sparse signal recovery and compressive sampling algorithms[13,14,26,36] are also promising directions that can be combined with pixel super-resolution schemes to further improve the resolution of lensfree on-chip microscopes.

Sample density: Because lensfree on-chip microscopy is a transmission imaging modality, sample density can cause issues in our imaging performance, for both holographic and contact imaging schemes. For contact shadow imaging, if the density of the specimen increases in 3D, it creates aberrations since the objects will effectively move away from the sensor active area, increasing the contribution of diffraction to shadow images, which directly reduces the resolution and creates aberrations using pixel super-resolution algorithms[18,19]. In case of density increase for planar 2D objects (where thickness of the specimen can be ignored, e.g., $\leq$1 μm), contact imaging would still exhibit aberrations/artifacts due to: (1) shadow stretching at the active plane of the sensor chip as a function of illumination angle; (2) change of object cross-section and its shadow as a function of illumination angle; and (3) partial interference of these dense object shadows with each other. The first two limitations mentioned above are unavoidable since contact imaging of static objects requires large illumination angles (e.g., up to ±60°) to achieve sub-pixel shadow shifts[18]. The third limitation is related to partial-coherence of illumination and needs to be carefully analyzed in high-resolution contact imaging even if the coherence diameter at the active region of the detector array is e.g., less than 1-2 μm. Stated differently, contact

mode lensfree imaging that uses pixel super-resolution techniques could exhibit 'artificial' sub-micron features under even a very small coherence diameter that is for example an order of magnitude narrower than the spatial coherence diameter provided by the Sun on Earth.

Similar limitations also apply to holographic lensfree on-chip imaging in the case of dense samples. For lensfree in-line holographic imaging geometry, as the density of the samples gets higher, the background light (which acts as a reference wave) gets distorted. One potential solution for this issue is to increase the distance between the sample and the detector chip so that a beam splitter can reflect an unscattered reference beam onto the sensor array[54]. This, however, would necessitate the use of increased temporal and spatial coherence for illumination and relatively complicate the setup in terms of alignment and size. Due to significantly increased distance between the sample and sensor planes, it would also reduce the effective FOV, especially for large area CCD chips.

Another solution to this object density issue that has been applied to wide-field on-chip holographic microscopy is multi-height lensfree imaging, where the sensor array records the lensfree diffraction holograms of the specimen at different heights. By iteratively propagating back and forth between e.g., 3-5 different heights, phase and amplitude images of dense objects can be reconstructed without the need for any spatial filtering[24,40,55]. The disadvantage of this approach is that more measurements are now required for the same sample, which also necessitates the use of additional computation to align the FOV of each multi-height lensfree hologram to others. This approach will be discussed in more detail in Chapter 3.

Reflection imaging: While dense and transparent specimen can be handled using lensfree on-chip microscopy tools, opaque samples cannot be imaged using the above discussed approaches. For relatively thick and non-transparent samples, such as thick tissue, reflection imaging would

be needed. There are previous reports on lensfree reflection imaging methods[15,56], however, these approaches have relatively smaller FOV, which is mostly due to significantly increased distance between the specimen and the detector array in reflection imaging geometry. Furthermore, while these reflection imaging approaches are lensfree, they still rely on a beam splitter cube to channel the reflected object field onto a sensor array. As the active area of the sensor chip gets larger (e.g., >10 cm^2) the size of such a beam splitter would also grow, which would further increase the distance between the specimen and the detector planes, causing signal-to-noise ratio limitations for sub-micron features of the object. Therefore, unlike its transmission counterpart, lensfree reflection microscopy is less suitable to reach extreme FOVs (>10-20 cm^2) that are enabled by e.g., the state-of-the-art CCD chips.

Fluorescent imaging: Our lensfree imaging discussions so far have been limited to bright-field microscopy on a chip. Fluorescent imaging, however, is another important modality that needs to be merged onto the same lensfree on-chip microscope for various applications that demand e.g., the use of molecular probes to bring additional functionality, specificity and sensitivity to the imaging platform. For this end, there have been some efforts to create dual-mode lensfree microscopes that can switch back and forth between bright-field and fluorescent imaging[29]. However, the resolution and image quality of these existing lensfree fluorescent imaging solutions are not yet as competitive as their bright-field counterparts[26,27,57]. There are several reasons behind this limited performance of lensfree fluorescent imaging. *First*, fluorescent emission is not directional and therefore the signal strength drops much faster as a function of vertical distance in a lensfree imaging geometry. This lower signal-to-noise ratio demands placing the labeled specimens rather close to the sensor chip surface (e.g., <400-500 μm). *Second*, decent filtering of the excitation light on a chip is challenging. In a lensfree

configuration, thin-film based standard fluorescent filters would not work as desired since the randomly scattered excitation light would not be collimated unlike conventional lens-based fluorescent microscopes. This requires relatively thicker absorption-based filters to be used, which would increase the distance between the sample and the detector active area, reducing the achievable resolution. *Third*, fluorescent emission is spatially and temporally incoherent, and therefore holographic digital reconstruction and related pixel super-resolution techniques that are based on e.g., source shifting are not useful in this case. While recently emerging sparse signal recovery techniques (based on e.g., compressive sampling) have been used to decode lensfree fluorescent images[27], their resolution level is still relatively coarse (~3-4 μm), which is mostly due to reduced signal-to-noise ratio of fluorescent on-chip imaging.

While the issues discussed above are creating technical obstacles for fluorescent imaging to achieve sub-micron resolution over a large imaging area, which is the characteristic signature of lensfree on-chip imaging, these difficulties do not constitute fundamental challenges. Systematic improvements in: (1) detection signal-to-noise ratio through e.g., actively cooled sensor chips; (2) absorption filter performance by use of better dyes; (3) smarter illumination schemes involving e.g., the use of structured excitation light; and (4) better incoherent signal recovery algorithms that exploit sparsity of fluorescent images could help us achieve high-resolution dual-mode lensfree on-chip microscopes that can switch between fluorescent and bright-field imaging of large FOVs. Once combined with color sensor arrays (e.g., RGB CMOS chips – see Fig. 1.3) multi-color lensfree fluorescent imaging could also be achieved, which might further expand the application of these on-chip microscopes into e.g., fluorescent cytometry.

Imaging speed: Imaging speed of lensfree on-chip microscopes is limited by the frame rate of the sensor array, which varies from ~1 fps to >50 fps depending on the exposure time and the

megapixel count of the sensor chip. Under appropriate illumination conditions, which can be satisfied even by an LED, the frame rate can be significantly increased to e.g., >200-300 fps by digitally selecting a smaller FOV within the active area of the chip. This also implies that *high-throughput scanning of large sample areas and volumes at high frame rates* can be achieved by digitally moving the region of interest within the active area of the chip. This could be quite useful for e.g., observing spatio-temporal dynamics of fast moving micro-organisms such as sperms[11], across large sample volumes to collect massive statistics about their natural swimming behavior as well as their response to various external stimuli.

Regarding the imaging speed, an important note is that the surface temperature of the sensor chip can easily go above 40°C at *continuous* operation, and therefore places an important temporal limitation for especially contact imaging approaches, which might not succeed in cooling the immediate top surface of the imager chip despite the use of cooling circuitry or heat sinks. This concern is also true for lensfree holographic approaches, to a lesser degree however, due to the increased distance (e.g., 1-2 mm) between the sample and the sensor chip.

Standardization of reconstruction techniques: The landscape of lensfree on-chip microscopes is relatively complicated with various designs. What makes this picture even more confusing is that the reconstruction methods/algorithms also vary depending on the imaging architecture. An important obstacle for wide-scale use of such emerging computational microscopy tools, especially in biomedical sciences, can be overcome through standardization of reconstruction algorithms by creating modular blocks (running on e.g., GPUs) that are integrated to each other for handling various possible lensfree imaging configurations. As a starting base toward this end, an open source computational wave optics library for holographic reconstruction is already available[58]. Once successfully scaled up, lensfree computational on-chip imagers could

lead to generation of massive amounts of microscopic data within various disciplines, which would present its own challenges, adding more to our existing "Big Data" problem[59]. This challenge, however, will also create new opportunities for microscopic analysis in general and could potentially be addressed through machine learning as well as crowd-sourcing strategies.

In conclusion, lensfree computational imaging tools are becoming more powerful in their capabilities to create wide-field microscopic images of transparent specimen on a chip, and I believe that they will continue to find broader applications/use in physical and biomedical sciences among others.

In the chapters to follow I will elaborate on my contribution to lensfree imaging: Chapter 2 presents the resolution improvement in lensfree imaging using an investigated pixel-function and color image sensors, Chapter 3 demonstrates the ability to reconstruct dense and confluent samples using multi-height phase recovery technique. Chapter 4 introduces novel colorization techniques to create color lensfree images, and Chapter 5 exhibits the translational value of lensfree microscopy by imaging pathology slides. Lastly, Chapter 6 demonstrates a field portable and cost-effective lensfree microscope that utilizes the presented computational methods, thus making it especially suitable for field settings and point-of-care use.

Chapter 2 Improving spatial resolution in lensfree imaging

Parts of this chapter have been previously published in Greenbaum, A. *et al.* Increased space-bandwidth product in pixel super-resolved lensfree on-chip microscopy. *Sci. Rep.* **3,** 1717 (2013).

In this chapter, I will describe how pixel-size limitation of lensfree on-chip microscopy can be circumvented by utilizing pixel-super-resolution techniques to synthesize a smaller effective pixel, improving the resolution. Here I report that by using the two-dimensional pixel-function of an image sensor-array as an input to lensfree image reconstruction, pixel-super-resolution can improve the numerical aperture of the reconstructed image by ~3 fold compared to a raw lensfree image. This improvement was confirmed using two different sensor-arrays that significantly vary in their pixel-sizes, circuit architectures and digital/optical readout mechanisms, empirically pointing to roughly the same space-bandwidth improvement factor regardless of the sensor-array employed in our setup. Furthermore, such a pixel-count increase also renders our on-chip microscope into a Giga-pixel imager, where an effective pixel count of ~1.6-2.5 billion can be obtained with different sensors. Finally, using an ultra-violet light-emitting-diode, this platform resolves 225 nm grating lines and can be useful for wide-field on-chip imaging of nano-scale objects, e.g., multi-walled-carbon-nanotubes.

2.1 Introduction

The setup of a lensfree microscope is simple and compact (see Fig. 1.1); a partially coherent and quasi-monochromatic light source (center wavelength, λ) illuminates a specimen that is positioned onto an optoelectronic image sensor-array[60–62]. The scattered light transmitted through the specimen interferes with the unperturbed background light and creates an in-line hologram that is sampled and digitized by the image sensor-array (see inset Fig. 1.1). Since this on-chip

microscope design has unit magnification, when capturing a raw lensfree hologram, the spatial sampling period and the sampling function are determined by the sensor's pixel pitch and its 2D pixel responsivity map within each pixel (which we refer to as the ***pixel function***). Stated differently, it is the pixel function of an opto-electronic sensor-array that fundamentally affects the spatial resolution and image distortions/aberrations in a lensfree holographic on-chip microscope. Different sensor chips have different pixel functions (with various pixel widths/heights and 2D functional forms), and therefore the nature of the spatial undersampling and convolution operations that occur at the sensor plane is highly dependent on the sensor choice[6].

In this chapter I demonstrate that by incorporating the 2D pixel function of an image sensor chip into lensfree holographic image reconstruction steps, one can improve the numerical aperture (NA) of the reconstructed images by a factor of ~3 compared to a raw lensfree image. Note that the term 'pixel super-resolution' here[6,7], together with other techniques[63] implemented in holographic imaging, refers to improving the NA of an imaging system within the diffraction limit, and thus should not be confused as surpassing the diffraction limit. This improvement is achieved using computational techniques (e.g. pixel super-resolution and hologram deconvolution), and is found to be, by and large, independent of the sensor chip design. Toward this end, we worked with both a monochrome CCD and a color CMOS image sensor chip that had a physical pixel size of e.g., 6.8 μm (Fig. 2.1(a)) and 1.12 μm (Fig. 2.1(b)), respectively. We used experimental and numerical techniques to estimate the 2D pixel function of each sensor-array, which in general would also be applicable for characterization of other opto-electronic sensors. Based on the information of this 2D pixel function, we experimentally found that using

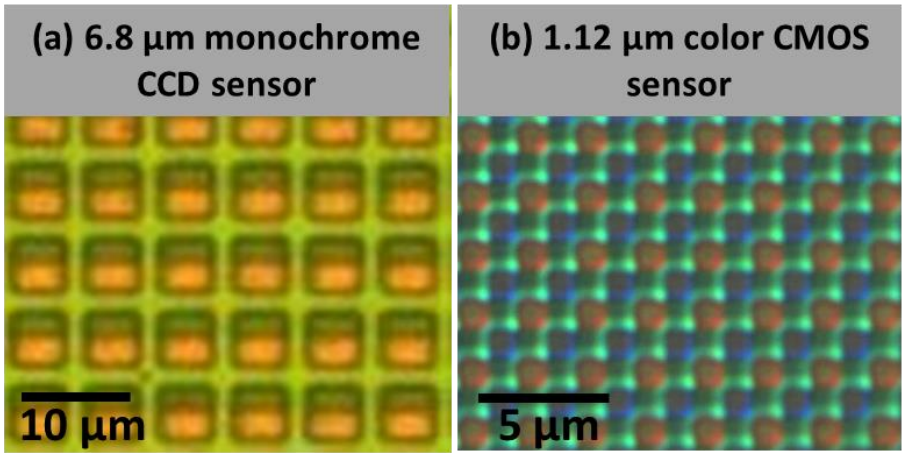


Figure 2.1 CCD and COMS image sensor chips. **(a)** Shows an optical microscope image (20× objective, NA = 0.5) of a 6.8 µm monochrome CCD image sensor chip. **(b)** Shows an optical microscope image (100× Water immersion objective, NA = 1) of a 1.12 µm color CMOS image sensor chip, where the Bayer pattern can be readily seen.

a CCD image sensor chip with a physical pixel size of 6.8 µm, in our reconstructed super-resolved images an NA of ~0.14 across an ultra-large FOV of ~18 cm^2 can be achieved, yielding a super-resolved effective pixel size of $\lambda/0.56$, where λ is the illumination wavelength. Under the same lensfree on-chip imaging geometry, using a CMOS image sensor chip that has a physical pixel size of 1.12 µm, we achieved an NA of ~0.83 across a FOV of ~ 20 mm^2, yielding a super-resolved effective pixel size of $\lambda/3.32$. Compared to the pixel count (i.e., megapixel value) of each native sensor chip, these pixel super-resolved lensfree images (under unit magnification) demonstrate a pixel density increase of $(3.81\mu m/\lambda)^2$ and $(3.72\mu m/\lambda)^2$, for the CCD and CMOS imagers respectively, which empirically point to roughly the same space-bandwidth improvement factor regardless of the sensor chip architecture used in our lensfree on-chip imaging setup. With these results, we achieved an effective pixel count of 2.52 billion with the 6.8 µm-pitch CCD image sensor; and obtained an effective pixel count of 1.64 billion with the 1.12 µm-pitch CMOS image sensor.

Finally, I also demonstrate that by utilizing a light emitting diode with a short illumination wavelength (λ = 372 nm), this pixel super-resolution based lensfree on-chip microscope can resolve periodic grating lines with a line-width of 225 nm. To better illustrate the capabilities and the potential applications of this wide FOV high-resolution lensfree microscopy platform we also imaged helical multi-walled carbon nanotubes (MWCNTs) with a diameter of ~160 nm.

2.2 Results

The resolution improvement of lensfree on-chip imaging is achieved by incorporating the estimated pixel function of a sensor array into the computational steps that are used in lensfree imaging (see Fig. 2.2(a)). In the next sub-sections, we will report estimation of the pixel function of CCD (pixel size: 6.8 μm) and CMOS (pixel size: 1.12 μm) image sensors, using an experimental and a numerical approach, respectively (see Fig. 2.2(b)). These pixel functions are then used to deconvolve the high-resolution lensfree holograms to undo distortions and enhance high spatial frequency components that were suppressed during lensfree hologram recording. Following this deconvolution step, each lensfree hologram is reconstructed to retrieve both the phase and the amplitude images of the object (see section 2.4). We present lensfree imaging results of a resolution test chart (1951 USAF), periodic grating lines fabricated by focused ion beam (FIB) milling and helical MWCNTs to demonstrate the resolution improvement on both of these CCD and CMOS image sensors.

Pixel function estimation of 6.8 μm CCD image sensor: To measure the pixel function of our monochrome CCD image sensor, a scanning microscopy system was assembled from a bright field microscope, a LED (λ = 470 nm) and an X-Y-Z piezo stage (see section 2.4). The scanning microscope illumination spot had a full width at half maximum (FWHM) of ~1.4 μm in

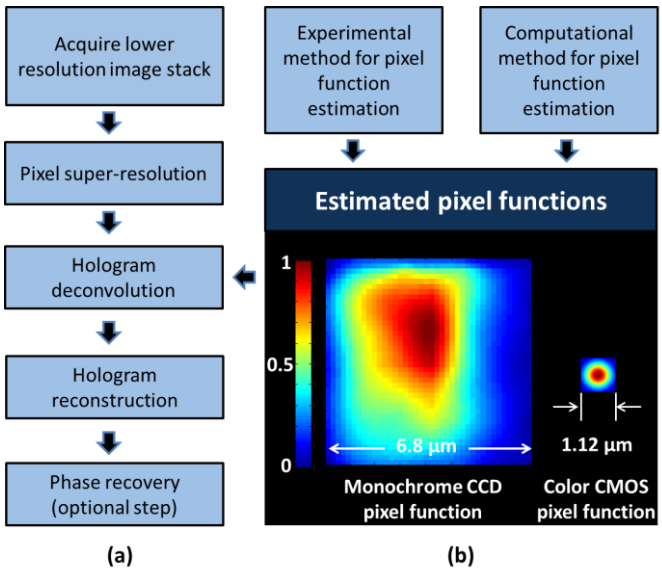


Figure 2.2 Image processing block diagram of lensfree on-chip microscopy. **(a)** Illustrates the block diagram of the computational methods that are used in creating a high-resolution image. In the hologram deconvolution step, either an experimental or a computational approach can be used to estimate the pixel function of the image sensor. **(b)** Shows two different pixel functions obtained with different methods: the left pixel function is obtained with an experimental method for the 6.8 µm monochrome CCD image sensor; and the right pixel function is obtained with a computational methods for 1.12 µm color CMOS image sensor.

both axes (Fig. 2.3(a)), which is much narrower in comparison to the pixel size of the image sensor-array (6.8 µm). This illumination scheme allowed the measurement of the pixel function by probing different positions within the area of a single pixel and recording the pixel response at each position. Fig. 2.3(b) shows a microscope image (20× objective lens, NA = 0.5) of a single pixel and the illumination spot (i.e., the bright spot on the upper right corner). Using the pixel output recorded from 54 measured sub-pixel locations (shown in Fig. 2.3(b)), an initial estimate of the pixel function of the CCD image sensor was obtained (Fig. 2.3(c), see section 2.4). Since the illumination spot size (~1.4 µm) cannot be treated as a spatial delta function, further refinement of this initial pixel function could be achieved. Toward this end, we deconvolved the

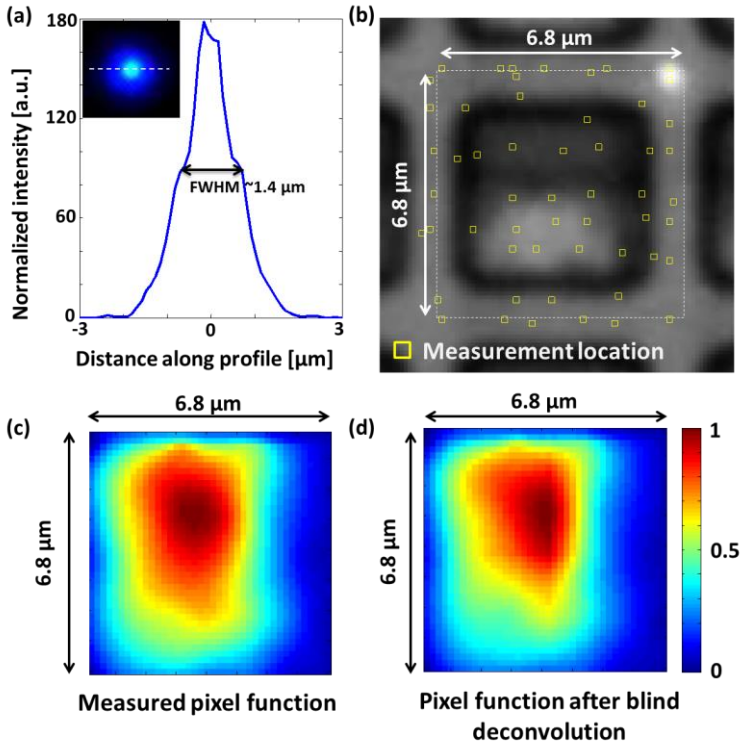


Figure 2.3 Experimental approach for pixel function estimation using a scanning microscope. **(a)** Shows a cross section of the illumination spot (see inset) of the scanning microscope, which is used to probe the pixel function of the 6.8 µm CCD image sensor. **(b)** Shows the illumination spot (the bright spot on the upper right corner) over the CCD image sensor. To estimate the pixel function of the CCD chip, 54 different locations were probed, as marked by yellow hollow rectangles. **(c)** Shows the measured pixel function after spatial interpolation. **(d)** Shows the resulting pixel function after blind deconvolution.

lensfree hologram of a known test object (e.g., 1951 USAF resolution test chart) using a blind deconvolution algorithm (built-in MATLAB routine: *deconvblind*), which provides maximum likelihood estimation for *both* the pixel function and the unblurred image[64–66]. After 35 iterations of this blind deconvolution algorithm a refined pixel function was obtained for our CCD image sensor as illustrated in Fig. 2.3(d).

This asymmetrical CCD pixel-function reported in Fig. 2.3(d) is also in agreement with the literature that reports the architecture of this sensor-array[67,68]. The KAF 39MP CCD image

sensor has two gate electrodes for each pixel; one is built using Indium Tin Oxide (ITO), while the other gate electrode is built from doped Polysilicon. ITO is more transparent, and therefore the light collection within the ITO region should be more efficient then in the doped Polysilicon gate electrode[67]. This is also confirmed by the optical microscope image of the pixel (Fig. 2. 1(a)), which clearly shows its asymmetrical structure: the dark rectangle is the ITO gate electrode and bright rectangle is the doped Polysilicon. Furthermore, the KAF 39MP pixel architecture includes a lateral overflow drain (LOD), which allows off-chip draining of the excessive signal. Accordingly, this LOD region does not collect light; and we believe that its position, which is not visible in the microscope image shown in Fig. 2.1(a), corresponds to the area of the pixel function that is not sensitive to light.

Pixel function estimation of 1.12 μm CMOS image sensor: It is experimentally challenging to directly measure the pixel function, when the pixel size of image sensor approaches a micrometer scale. Therefore we adopted a *computational* approach instead, to estimate the pixel function of the 1.12 μm CMOS image sensor (see section 2.4 for details). This computational method generates various pixel functions, and for each pixel function the holograms of known test objects are deconvolved and reconstructed. By evaluating these reconstructed images one can quantify the effect of the estimated pixel function, and the pixel function with the best performance can be treated as an approximation to the real pixel function. Based on the reported architecture of the image sensor[69] and the morphology of the lens-array installed on this CMOS imager (see Fig. 2.1(b)), it is physically necessary to apply two constrains on the structure of the pixel function. (1) Similar to the morphology of the microlenses, the pixel function possesses a circular symmetry. (2) The crosstalk between neighboring pixels is negligible; and therefore the size of the pixel function equals the pixel pitch. Accordingly, we approximated the pixel function

of our CMOS sensor-array with a two-dimensional Gaussian distribution within a 1.12 μm square area. Four parameters of the Gaussian pixel function were optimized: the X-Y coordinates of its center position and the FWHM of the Gaussian in both the vertical and the horizontal directions. We digitally scanned the values of these parameters to generate various responsivity distributions within the pixel area, and fed each 2D distribution into the hologram deconvolution step (Fig 2.4(a)). As shown in Fig. 2.4(b), the objects reconstructed from the deconvolved holograms are evaluated by either measuring the modulation depths (grating lines), or the width of averaged cross-section profiles (helical MWCNTs). We combined all these evaluation results from various objects, and used this combination as the 'cost function' for pixel function optimization. By minimizing this cost function, our estimate of pixel function converged to a 2D Gaussian distribution, which has both a vertical and a horizontal FWHM of ~550 nm as illustrated in Fig. 2.4(b).

Lensfree on-chip imaging results obtained with 6.8 μm CCD image sensor: Using the CCD sensor-array, we imaged a 1951 USAF resolution test chart to quantify the resolution improvement of our holographic microscope, when pixel super resolution and hologram deconvolution steps are utilized. In these experiments, the illumination wavelength was 480 nm (illumination bandwidth ~4 nm) and the objects were located at ~390 μm away from the CCD image sensor active area. Fig. 2.5(a) shows the amplitude image of a reconstructed hologram obtained from only one lensfree hologram measurement i.e., without pixel super resolution. The thinnest resolved grating lines are within Group 6 Element 4, which corresponds to a half-pitch resolution of ~5.52 μm and an NA of ~0.04. After applying ***only*** pixel super- resolution, the

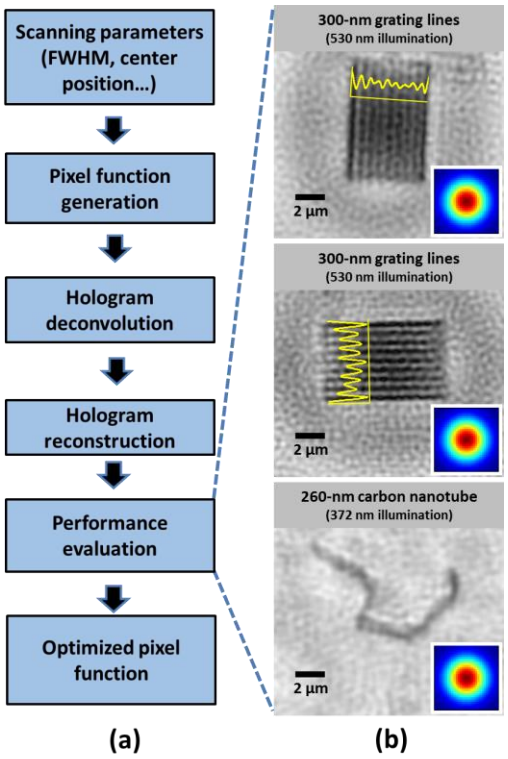


Figure 2.4 Computational approach for pixel function estimation. **(a)** Shows the block diagram of our pixel function estimation steps using a computational method. **(b)** Shows the reconstructed images when an optimized pixel function is used in the hologram deconvolution step. Three representative objects are illustrated: horizontally and vertically oriented grating lines (top and middle), and a helical multi-walled carbon nanotube (bottom). The insets show the estimated pixel function of the 1.12 μm CMOS sensor chip.

amplitude image of a reconstructed hologram exhibits a major improvement in resolution (see Fig. 2.5(b)). The entire group 7 can now be resolved, which translates to a half-pitch resolution of ~2.2 μm and an NA of ~0.11. In group 8, the horizontal lines of elements 1 and 2 are also resolved, while the vertical lines cannot be resolved as indicated by yellow cross sections in the same figure. Fig. 2.5(c) shows the amplitude image of a reconstructed lensfree hologram after applying hologram deconvolution. To deconvolve the image we used 35 iterations of MATLAB

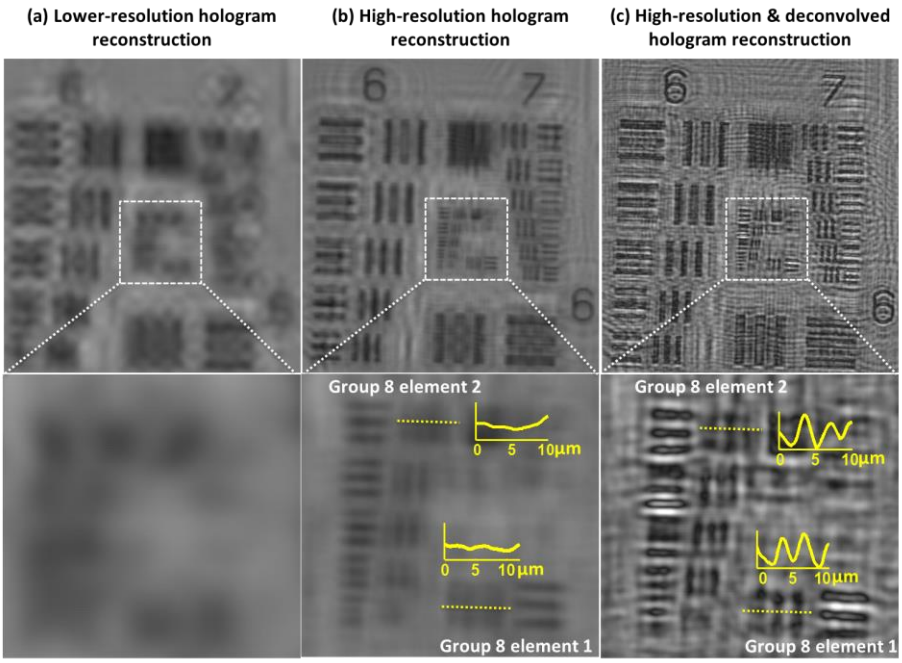


Figure 2.5 Lensfree on-chip imaging results obtained with a 6.8 µm CCD image sensor demonstrating an NA of ~ 0.14 over a field-of-view of ~18 cm^2. **(a)** Shows a lensfree amplitude image, which was reconstructed from a single lensfree hologram without using pixel super-resolution. **(b)** Shows a lensfree amplitude image, which was reconstructed from a pixel super-resolved lensfree hologram *without the deconvolution step*. The horizontal lines of group 8 elements 1 and 2 were resolved, while the vertical lines were not resolved as indicated by the yellow cross sections in the image. **(c)** Shows a lensfree amplitude image, which was reconstructed from a pixel super-resolved hologram *with* the deconvolution step using the estimated pixel function (see Fig. 2.3(d)) before the final reconstruction step. The vertical lines in group 8 elements 1 and 2 are now resolved as indicated by the cross sections in the image, which corresponds to half pitch resolution of ~1.74 µm and an NA of ~0.14.

built-in routine *deconvblind*, using the measured pixel function described earlier as the initial guess[64,65]. The horizontal and vertical lines in group 8 elements 1 and 2 are now resolved as indicated by the cross sections in the image, which translates to a half-pitch resolution of ~1.74 µm and an NA of ~0.14. Overall, after applying pixel-super resolution and hologram deconvolution with the 2D pixel function, the NA of the lensfree holographic microscope

improves by a factor of ~3 compared to a single lensfree hologram. Therefore, the effective pixel size is also reduced from λ/0.16 to λ/0.56, yielding an increase in the pixel count by a factor of ~12. Moreover, this resolution improvement does not compromise the FOV, and therefore with our 6.8 μm 40 Mega-pixel CCD image sensor, the effective pixel count over a FOV of 18 cm^2 reaches to ~2.52 Giga-pixels when e.g., 480 nm illumination wavelength is used.

Lensfree on-chip imaging results obtained with 1.12 μm CMOS image sensor: Using the 1.12 μm CMOS image sensor, we imaged 225 nm grating lines (fabricated using FIB) and helical MWCNTs at an illumination wavelength of 372 nm. With hologram deconvolution based on the estimated pixel function (Fig. 2.2(b)), both the grating lines and the helical MWCNTs can be clearly resolved as illustrated in Fig. 2.6. At an illumination wavelength of 372 nm, resolving a grating of 225 nm line-width corresponds to an NA of ~0.83, which once again confirms an improvement factor of ~3 compared to a single lensfree holographic image. Stated differently, using pixel super-resolution and hologram deconvolution steps on the 1.12 μm CMOS sensor chip, the effective pixel size can be reduced from λ/1.08 to λ/3.32. Such pixel size reduction yields an increase in the effective pixel density by a factor of ~9.4. Therefore, with our 16.4 Mega-pixel CMOS image sensor we achieve an effective pixel count of 1.64 billion over a FOV of ~20 mm^2 when e.g., 372 nm illumination wavelength is used.

2.3 Discussion

The image sensor properties play a critical role in lensfree imaging performance, especially for implementing pixel super-resolution. In this work, we shed more light onto this affect and reported that by using an estimated 2D pixel function of an image sensor-array as an input to lensfree holographic image reconstruction steps, pixel super-resolution can improve the NA of the reconstructed images by a factor of ~3 compared to a raw lensfree image. We confirmed this

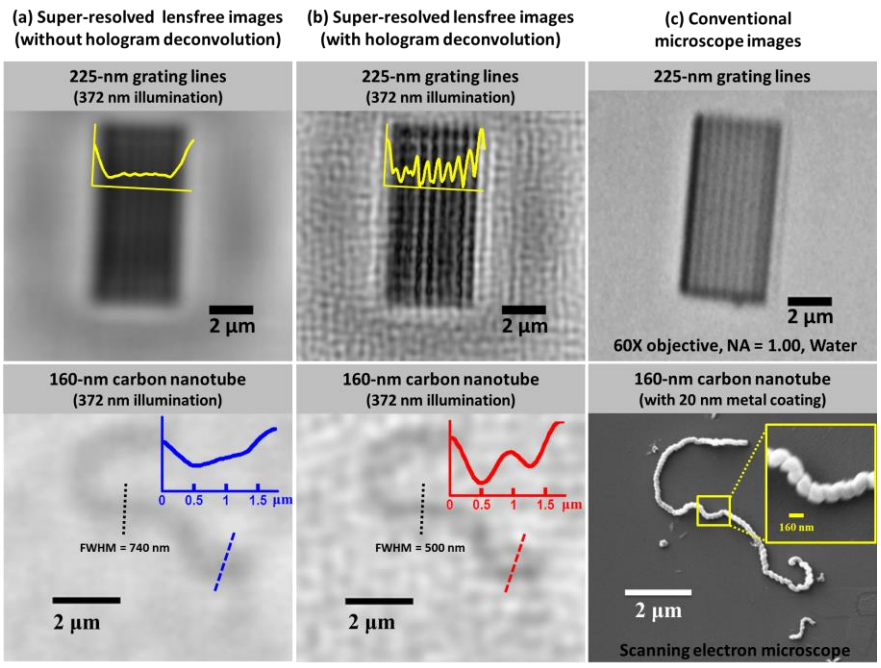


Figure 2.6 Lensfree on-chip imaging results obtained with a 1.12 µm CMOS image sensor demonstrating an NA of ~ 0.83 over a field-of-view of ~20 mm^2. **(a)** Shows lensfree images reconstructed from super-resolved holograms without deconvolution. **(b)** Shows lensfree images reconstructed from super-resolved and deconvolved holograms using the optimized pixel function shown in the inset of Fig. 2.4(b) **(c)** Top: a conventional optical microscope image (60× water immersion objective, NA = 1) of a grating with 225 nm line-width. Bottom: an SEM image of a helical carbon nanotube that is 160 nm in diameter. Note that in the SEM image, the carbon nanotube is coated with 20 nm metal coating and therefore the observed carbon nanotube diameter is thicker.

improvement factor using two different image sensors that significantly vary in their designs, i.e., a monochrome CCD and a color CMOS image sensor. Using the CCD image sensor-array (pixel size of 6.8 µm), we achieved an NA of ~0.14 across an ultra-large field-of-view of ~18 cm^2 yielding a super-resolved effective pixel size of λ/0.56; whereas using the CMOS image sensor-array (pixel size of 1.12 µm), we achieved an NA of ~0.83 across a FOV of ~ 20 mm^2, yielding a super-resolved effective pixel size of λ/3.32. Furthermore, by adopting a short illumination wavelength (λ = 372 nm) a record high spatial resolution for lensfree on-chip imaging is

obtained with the same CMOS sensor: a grating with a line-width of 225 nm is resolved and a helical MWCNT with a diameter of ~160 nm is successfully imaged.

An interesting observation in these results is a sensor-chip independent NA improvement factor of ~3, which is achieved by utilizing pixel super-resolution and hologram deconvolution. Furthermore, compared to the original pixel count of each sensor-chip, our pixel super-resolved lensfree images demonstrate a pixel count increase of $(3.81\mu m/\lambda)^2$ and $(3.72\mu m/\lambda)^2$, for our CCD and CMOS imagers respectively, which empirically point to roughly the same space-bandwidth improvement factor. I believe that a similar level of space-bandwidth improvement can in general be maintained in lensfree on-chip imaging even if the image sensors differ in their technologies (CMOS vs. CCD), pixel-pitches, detection architectures (e.g., back illuminated vs. front illuminated), and imaging applications (color vs. monochrome).

Finally, I would like to emphasize that in our hologram deconvolution process, higher spatial frequencies that are normally undersampled and suppressed are now boosted; and as a direct consequence of this, the noise is also amplified. Different deconvolution algorithms might better handle this noise amplification problem, and therefore future research on optimization of hologram deconvolution steps could improve our results since most of the existing deconvolution codes are optimized for photography applications and not for holography[66].

2.4 Theory and methods

Image formation in lensfree imaging: The setup for capturing an in-line hologram and the Cartesian coordinate system are shown in Fig. 1.1. The light from the partially coherent source vertically propagates towards the sample with a distance of ~4-10 cm (Z_1 distance see Fig. 1.1), and impinges on the specimen. The scattered light transmitted through the specimen $O(x, y, z)$ interferes with the unperturbed background light $R(x, y, z)$ and creates an in-line hologram that

is sampled and digitized by an image sensor-array. Note that the image sensor records only intensity:

$$I(x,y,0) = |R+O|^2 = |R|^2 + |O|^2 + R^*O + RO^*. \qquad (2.1)$$

The first term on the right hand side of equation (2.1) is the intensity of the background illumination, which is approximately a plane wave; hence it is a constant that can be subtracted digitally. The second term is the intensity of the scattered light by the object. It is commonly assumed in holography that the object is a weak scatterer, and therefore in comparison to the other terms ($|O| \ll |R|$) this term is small and can be ignored. The last two heterodyne terms (the object wave and the object conjugate wave) are the holographic terms. The object conjugate wave is an error term commonly referred as the twin-image artifact. This artifact is inevitably present in all in-line holographic imaging systems due to the loss of the optical phase information during the intensity recording process. Sparse objects that slightly perturb the illumination wavefront are less affected by the twin image noise, whereas dense objects such as connected tissue slides are generally affected to a larger degree. Nevertheless, these terms contain the full complex information of the scattered object wave, and enable digital focusing of the object.

Back propagation of holograms: To digitally focus the object, the hologram in equation (2.1) is reconstructed. The reconstruction process starts by multiplying the hologram with a reference wave, which can be approximated as a plane wave, and followed by propagation of the field to the object plane (Z_2 plane see Fig. 1.1) using the Rayleigh-Sommerfeld diffraction integral[70,71]:

$$U_2(x',y',z_2) = \int_{-\infty}^{\infty}\int_{-\infty}^{\infty} U_1(x,y,0)\frac{e^{i\frac{2\pi}{\lambda}r_1}}{r_1}\cdot\frac{z_2}{r_1}\left(\frac{1}{2\pi r_1}+\frac{1}{i\lambda}\right)dx\,dy. \qquad (2.2)$$

Where U_1 is the scalar complex field on the sensor plane, which is reconstructed from equation (2.1), U_2 is the field in the specimen plane, and $r_1$is defined in equation (2.3):

$$r_1 = \sqrt{(x' - x)^2 + (y' - y)^2 + {z_2}^2}. \quad (2.3)$$

A close examination of equation (2.2) reveals that the integral can be rewritten as a 2D convolution integral using a kernel $h(x, y, z)$, which is defined in equation (2.4):

$$h(x, y, z) = \frac{e^{i\frac{2\pi}{\lambda}r}}{r} \cdot \frac{z_2}{r}\left(\frac{1}{2\pi r} + \frac{1}{i\lambda}\right) \quad (2.4)$$

where r is now defined in equation (2.5):

$$r = \sqrt{x^2 + y^2 + z_2^2}\,. \quad (2.5)$$

Therefore equation (2.2) can be readily solved in the frequency domain, by applying the convolution theorem:

$$U_2(x, y, z_2) = F^{-1}\{F\{U_1(x, y, 0)\} \cdot F\{h(x, y, z)\}\}, \quad (2.6)$$

where F and F^{-1} are the 2D Fourier transform and its inverse respectively. The Fourier transform of the convolution kernel h is commonly known as the free space transfer function and it can be written as[72]:

$$H(f_x, f_y, z_2) = \begin{cases} e^{i2\pi z_2\sqrt{\frac{1}{\lambda^2} - f_x^2 - f_y^2}} & , f_x^2 + f_y^2 \leq \frac{1}{\lambda^2} \\ 0 & , f_x^2 + f_y^2 > \frac{1}{\lambda^2} \end{cases}, \quad (2.7)$$

where f_x and f_y are the spatial frequencies.

Object-support based phase recovery: The resulting back-propagated field also contains a noise term commonly referred to as the "twin image" noise see equation (2.1), which is unavoidable for in-line holography geometry. This twin image noise can be mitigated by using an object support based phase-recovery approach; an iterative process that iterates between the object and the hologram planes, enforcing a unique constraint in each one of these planes[5,6]. For example, in the hologram plane the enforced constraint is the measured intensity, while in the

object plane the enforced constraint suppresses the field to a constant value outside the object support, also keeping the field unchanged within the object support[5,6]. The object support can be evaluated by a simple threshold in the object domain and this phase recovery process typically converges after ~10-15 iterations. Recently, a multi-height based lensfree imaging technique has also been demonstrated for on-chip microscopy to entirely eliminate this object support step, which is especially superior for imaging of dense and connected specimen[24]. This approach will be further discussed in Chapter 3.

Implementation of pixel super-resolution in lensfree on-chip holography: Pixel super-resolution is a computational method to overcome undersampling of an image, due to for example the physical pixel size of the image sensor-chip[7,44,46]. Therefore, it aims to generate a high-resolution image from a stack of lower resolution images. Each image in the lower resolution stack should be of the same object; however, each image should also be translated from the other images in the stack, thus containing new undersampled information about the object of interest. In our experimental setup we used lateral movements of the light source, which was mounted on an X-Y stage (Newport, SMC100PP) in order to achieve sub-pixel shifts of the lensfree holograms on the sensor-chip. The high-resolution lensfree hologram is then synthesized by first digitally estimating the shifts between the acquired lensfree holograms in the stack using an iterative gradient method[6]. After these shifts are calculated, we use a non-iterative method to synthesize the high-resolution lensfree hologram (with a much smaller effective pixel size), while preserving the optimality of the reconstruction in maximum-likelihood sense[46]. Pixel super-resolution performs very well with either monochrome or color image sensors (see e.g., Figs. 2.5 and 2.6); however, for color image sensors minor modifications are required[73].

Experimental setup for measuring the pixel function: The scanning microscopy system used for CCD pixel function measurement was composed of a bright field microscope in reflection mode (Olympus, BX51), an X-Y-Z piezo stage (PI, 611.3S) and a LED (λ = 470 nm, Mightex, FCS-0470-000) that was butt-coupled to a single mode fiber (ThorLabs, P1-630A-FC2). To create the illumination spot, the eyepiece of the microscope was removed and the fiber end was mounted instead of the eyepiece, while allowing movement of the fiber in only one axis (toward and away from the microscope). In this configuration the image of the fiber end is demagnified and projected on the object plane. The demagnification factor used in our setup was 20×, as determined by the objective lens in use. To independently verify the illumination spot size and to focus the spot on the KAF 39MP image sensor active plane, a calibration step was performed. In this step, the focal plane of the projected image of the fiber end was calibrated to coincide with the focal plane of the bright field microscope in reflection mode. The calibration was done by placing a reflective metal surface on the microscope stage and focusing the bright field microscope on this reflecting surface. Then, the microscope lamp was turned off, while the LED was turned on, thus creating a spot on the reflective surface. By moving the fiber in the eyepiece toward and away from the microscope, the minimum spot size was found. The fiber is then fixed to the position that corresponds to the minimum illumination spot size, in order to ensure that the illumination focal plane would coincide with the microscope focal plane. The FWHM of the illumination spot after this calibration step was ~ 1.4 μm as shown in Fig. 2.3(a).

Next, the CCD image sensor chip was placed on the top of the X-Y-Z stage, which was itself placed onto the microscope stage. By turning the LED on and observing the image sensor using the reflection microscope, the spot position within the pixel area could be determined. As an example, Fig. 2.3(b) shows the reflection microscope image and the illumination spot (bright

spot on the upper right corner). To probe a specific location within a single pixel area, the X-Y-Z piezo stage was used to change the relative position of the illumination spot and to correct for possible focus drifts. A non-uniform scanning pattern was applied in order to probe with more measurements regions (e.g. edges) that showed fast transitions in responsivity. After a specific location was selected, the bright field microscope illumination was turned off while the LED (positioned in the eyepiece) was kept on. In this configuration, a narrow spot illuminates only a single pixel while the KAF 39MP image sensor acquires an image. To reduce noise, multiple measurements/frames (~10) were averaged for the same spot location. It should also be noted that to reduce the intensity of the illumination spot and to avoid saturation while capturing a CCD image, a neutral density filter, which was placed in the filter cube of the microscope, was brought into the illumination path of our setup.

From raw CCD measurements to pixel function estimation: After probing the area of a single CCD pixel at 54 locations (see Fig. 2.3(b)) the pixel function was estimated using the following steps. First, the relative position of each measurement was determined by finding the correlation peak between a Gaussian spot and the blue channel image of the microscope image. The blue channel was selected since the illumination spot contrast was higher in comparison to the pixel structure. Second the image was shifted by three pixels to compensate for a systematic bias caused by the positioning of the neutral density filter in the illumination path. Third, the measurements were interpolated in 2D to obtain the resulting pixel function shown in Fig. 2.3(c).

To deconvolve the lensfree holograms of the test objects with the estimated pixel function, we used a built-in MATLAB routine *deconvblind*. This routine implements maximum likelihood estimation for both the blur kernel (the pixel function in our case) and the unblurred image using the expectation-maximization algorithm[64]. The measured pixel function (Fig. 2.3(c)) serves as an

initial guess for the algorithm and after 35 iterations the unblurred hologram and the modified pixel function (see Fig. 2.3(d)) are provided as outputs.

Computational method for 1.12 μm CMOS sensor pixel function estimation: Based on the assumption that a 2D Gaussian distribution can be used for estimation of our CMOS pixel function, we optimized the vertical and horizontal FWHM values of this distribution and its center position within the pixel area. During this optimization process, both the FWHM values and the center position were numerically scanned, and their corresponding 2D Gaussian distributions were used in hologram deconvolution step using Wiener deconvolution algorithm[74]. The deconvolved holograms were then back-propagated using an angular spectrum approach to reconstruct the objects[5,72]. By evaluating all the reconstructed images one can find an optimized Gaussian distribution, which can be considered as an approximation to the actual CMOS pixel function.

To evaluate the reconstruction results, two types of known objects were chosen: (1) periodic grating lines fabricated onto a glass substrate using focused ion beam (FIB) milling; and (2) helical MWCNTs (CheapTubes Inc.), which were smeared on a thin glass substrate (~50 μm). During the lensfree imaging process, the vertical distance between the objects and the image sensor surface was on the order of 50-150 μm. This gap between the substrate and image sensor planes is filled with a refractive index matching oil to minimize reflection losses and increase the effective NA.

Grating lines exhibit a strong signal-to-noise ratio (SNR) at specific spatial frequencies due to their periodic structure. As expected, the reconstruction results of grating lines show a strong orientation dependency: when the vertically oriented grating lines are imaged, the parameters of horizontal pixel distribution drastically affect the reconstructed image, while parameters of

vertical pixel distribution do not exhibit such a strong effect on the reconstruction results. Considering this orientation sensitivity, in our lensfree imaging experiments each set of grating lines has been imaged in horizontal and vertical orientations in order to find the optimized pixel parameters in both directions. The reconstructed images are then evaluated by measuring the corresponding modulation depth at the period of the grating lines.

We should also emphasize that the gratings lines are not sufficient for searching the globally optimized pixel parameter space since gratings are inherently limited in terms of their spatial frequency contents, which might lead to locally optimized pixel functions. To avoid such a bias, besides grating lines with various periods, we also used the helical MWCNTs for pixel function parameter scan. These helical MWCNTs vary in their widths (e.g., ~100-200 nm) and morphologies, and therefore are quite rich in spatial frequency content. To verify our results, the same MWCNTs imaged with our lensfree microscope were also imaged using scanning electron microscopy (SEM) to confirm their widths and morphologies. After reconstruction of a lensfree amplitude image, cross-section profiles are taken across the entire imaged MWCNT and the average width of these cross-sections is used for evaluation of the success (i.e., the cost function) of our reconstruction.

During the digital search for the optimal pixel function, each individual object might yield its own ‘locally optimized’ pixel distribution. Since the pixel function should be independent of the objects, we combined of all the evaluation results for different objects within our cost function and searched for a ‘globally optimized’ pixel distribution. The pixel distribution which gave the maximum overall modulation depth in grating samples and the minimum overall line-width in MWCNT samples is considered as our converged pixel function.

Chapter 3 Imaging dense specimen using lensfree on-chip holographic microscopy

By and large, in-line holography is limited to relatively low-density samples. To mitigate this limitation and to provide lensfree microscopy the ability to image connected tissue, I demonstrate in this chapter an on-chip imaging approach based on pixel super-resolution and phase recovery. The phase recovery approach iterates among multiple lensfree intensity measurements, each having a slightly different sample-to-sensor distance. By digitally aligning and registering these lensfree intensity measurements, phase and amplitude images of dense and connected specimens can be iteratively reconstructed over a large field-of-view of ~24 mm^2 without the use of any spatial masks. I demonstrate the success of this multi-height in-line holographic approach by imaging dense Pap smears and blood samples. Parts of this chapter have been previously published in Greenbaum, A. & Ozcan, A. Maskless imaging of dense samples using pixel super-resolution based multi-height lensfree on-chip microscopy . *Optics Express* **20**, 3129-3143 (2012).

3.1 Introduction

The super-resolved in-line hologram that is reconstructed in the previous chapter, still suffers from twin-image artifact, which is common to all in-line hologram recording geometries[72]. In our group earlier work, we demonstrated the use of an iterative object-support based phase recovery method[75,76] to eliminate this twin-image artifact creating wide-field microscopic images of samples. This twin-image elimination method, however, requires as input the location estimations of the objects within the imaging field-of-view. For this end, a simple threshold or a segmentation algorithm can be used to automatically estimate the objects' locations (creating the

object-support) for relatively sparse samples. However, in denser specimens, this object support is difficult to estimate which can create challenges in removal of the twin-image artifact.

To overcome these object-support related imaging challenges for dense and connected specimens, here we demonstrate a new approach for pixel super-resolution holographic microscopy that uses multiple (e.g., 2-5) lensfree intensity measurements that are each captured at a different height (i.e., Z_2) from the detector-array (see Fig. 1.1). Stated differently, each lensfree super-resolved hologram is synthesized with ~30-70 μm change in the relative height of the object with respect to the detector-chip surface, after which they are digitally registered and aligned to each other to take into account possible rotations and shifts among these in-line holograms. These co-registered super-resolved holograms, corresponding to different object heights, are then iteratively processed[40] to recover the missing optical phase so that microscopic images of the specimens can be automatically reconstructed *without* the need for any spatial masking steps. Therefore, this multi-height holographic approach eliminates the need to estimate the object-support at the sample plane cleaning the twin-image artifacts of our in-line geometry over a large field-of-view of e.g., ~24 mm² even for dense and connected specimens.

The performance of this approach is validated by imaging dense Pap smears/tests, which are used to screen cervical cancer by detecting premalignant and/or malignant cells in the endocervical canal as well as blood samples. Providing a light-weight and cost-effective design, this multi-height holographic on-chip imaging platform could be rather useful for wide-field microscopy and pathology needs in resource poor locations as well as in field conditions.

3.2 Results

A schematic diagram of our lensfree multi-height imaging setup can be seen in Fig. 1.1. The setup is composed of a partially-coherent light source (~5 nm bandwidth centered at 550 nm),

glass cover slips with different thicknesses and a CMOS detector-array. The setup is rather simple to operate without any complicated alignment. For reconstructing dense samples where object-support based phase-recovery approaches face challenges, different lensfree intensity measurements of the sample are acquired at different Z_2 distances.

The Z_2 distance is controlled by placing glass cover slips with different thicknesses between the sample and the sensor-chip. The thicknesses of our glass cover slips varied between 50 μm and 250 μm, hence the corresponding Z_2 distances varied between ~0.7 mm and ~1 mm. Each lensfree intensity measurement is sampled by our CMOS sensor with 2.2 μm pixel size. This relatively large pixel size can cause undersampling issues; therefore, a pixel super resolution method is applied in order to effectively decrease the detector pixel size[6,7]. For each Z_2-distance a lower-resolution image stack is captured, where each image in this stack is sub-pixel shifted with respect to the other images in the stack. These sub-pixel shifts are achieved by a slight translation of the fiber-tip position between two sequential images

Fig. 3.1 depicts the image processing steps after image acquisition. For each Z_2-distance, one super-resolved hologram is synthesized from the low-resolution image-stack (typically 16 images in each stack). Then, these *M* super resolved images are registered to each other to account for rotation, translation and shear that may occur during placing/replacing the glass cover slips between each lensfree measurement. For the reconstruction procedure (iterative phase recovery), these *M* super resolved intensity measurements are utilized as amplitude constraints (typically 1-70 iterations are required for satisfactory results). Once the phase is iteratively recovered, any one of these *M* super resolved images is low-pass filtered (Butterworth 2^{nd} order) to eliminate high frequency noise and the resulting complex image is back propagated to the

object plane, retrieving both phase and amplitude images of the specimens on the chip (see Fig. 3.1).

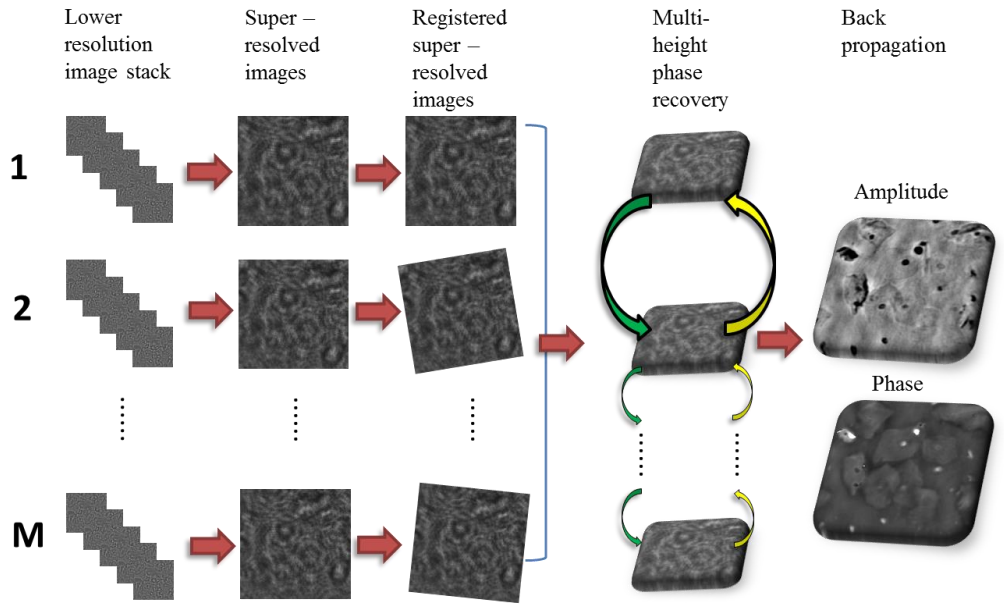


Figure 3.1 A schematic portraying the image processing that is conducted after acquiring M low-resolution lensfree image stacks at different Z_2-distances. Each image stack is used to create one super-resolved lensfree hologram. These high-resolution holograms are then registered to each other and multi-height iterative phase recovery algorithm is applied. After 1-70 iterations, amplitude and phase images of dense specimens can be reconstructed.

Fig. 3.2 illustrates the benefits of using the above outlined multi-height lensfree imaging approach for a blood smear sample. Fig. 3.2(a) shows a full FOV (~24 mm^2) low resolution lensfree hologram as captured by the CMOS sensor. The green dashed rectangle focuses on an area that is rather dense; however the blood cells are still organized as a mono-layer, suitable for imaging. The reconstruction results of this dense blood smear using five different Z_2-distances (711μm, 767μm, 821μm, 876μm and 946μm) are shown in Fig. 3.2(b). These five Z_2-distances/heights are automatically evaluated by using an auto-focus algorithm[62,77]. The reconstruction results of Fig. 3.2(b) provide a decent agreement to a 10× microscope objective

comparison image shown in Fig. 3.2(c). Figures 3.2(d) to (f) provide images of zoomed areas (taken from the dashed blue rectangle in Fig. 3.2(b)) of single height back propagation image, multi-height reconstruction image and a 20× microscope objective comparison image, respectively. The back propagated single height image (Fig. 3.2(d)) has lower contrast, and it is hard to evaluate the locations of the RBCs for spatial masking purposes. Therefore support-based phase recovery would not be effective in this case. On the other hand, the multi-height amplitude image (Fig. 3.2(e)) has significantly improved contrast, and individual RBCs can be identified and resolved even in dense clusters. *It is important to emphasize that these multi-height reconstruction images shown in Figs. 3.2(b) and (e) are obtained without the use of any spatial masking or any other prior information regarding the sample.*

After these blood smear experiments, next we imaged Pap smears (based on SurePath™ automated slide preparation[78]) using the same multi-height imaging setup. Fig. 3.3 summarizes our imaging results for this Pap smear. Because of the density of the specimen, the reconstruction of this image is a challenging task for any phase recovery method. Fig. 3.3(a) shows the multi-height phase image, which is recovered using lensfree measurements from five different heights (754μm, 769μm, 857μm, 906μm and 996μm - these Z_2-distances were automatically determined using an auto-focus algorithm[62,77]). Figures 3.3(c,h) and (d,i) show zoomed images of the same Pap smear sample, for amplitude and phase channels, respectively. In these reconstructed multi-height images the cell morphology is clear and their boundaries can clearly be seen and separated from the background. Moreover, minor overlaps among the cells do not constitute a limitation in this method. As a comparison, Fig. 3.3(b) depicts a single height back propagated phase image corresponding to one of the Z_2 measurements (the FOV is the same as in Fig. 3.3(a)). It is evident that distinguishing the cells from the background is a difficult task

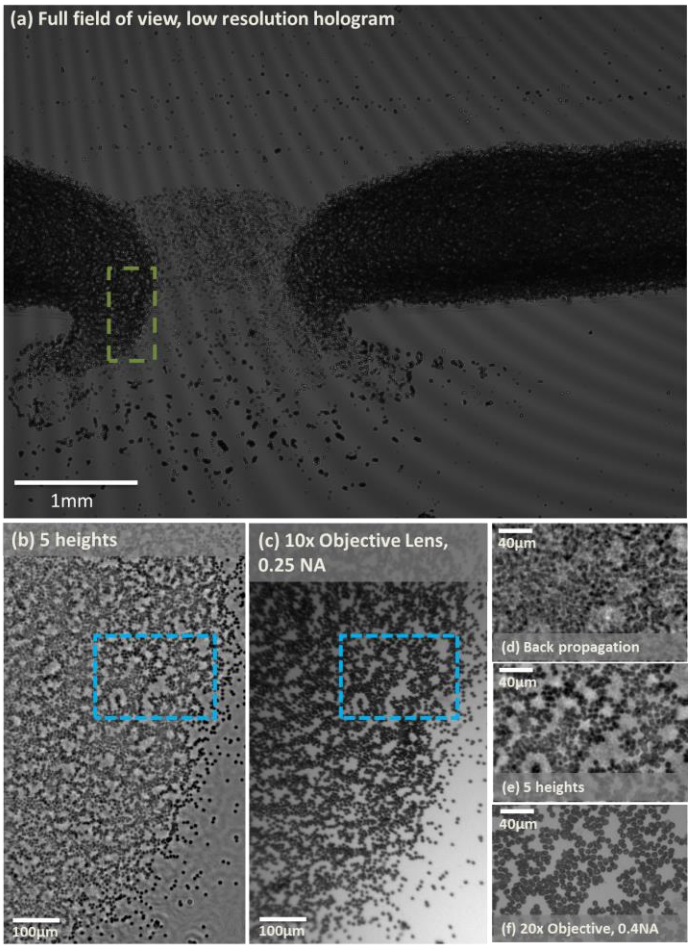


Figure 3.2 (a) Full FOV, low resolution hologram. **(b)** Multi-height based pixel super resolution lensfree amplitude image of a dense RBC smear is shown. This lensfree image was reconstructed using five different heights (λ = 550 nm). The FOV corresponds to the green dashed rectangular in (a). **(c)** A 10× objective lens (0.25 NA) microscope image is provided for comparison. **(d)** A single height back propagated pixel super-resolved amplitude image. The image FOV corresponds to the dashed blue rectangular in (b) and (c). **(e)** Multi-height based pixel super resolution lensfree amplitude image acquired using five different heights is shown. This FOV corresponds to the same FOV as in (d). **(f)** A 20× objective lens (0.4 NA) microscope image is also provided for comparison purposes.

in this dense reconstructed image. To better provide a comparison, Figures 3.3(f,k) and (g,l) also show zoomed images of the same Pap smear sample, for phase and amplitude channels, respectively, calculated using back propagation of a single height image. Compared to Figures

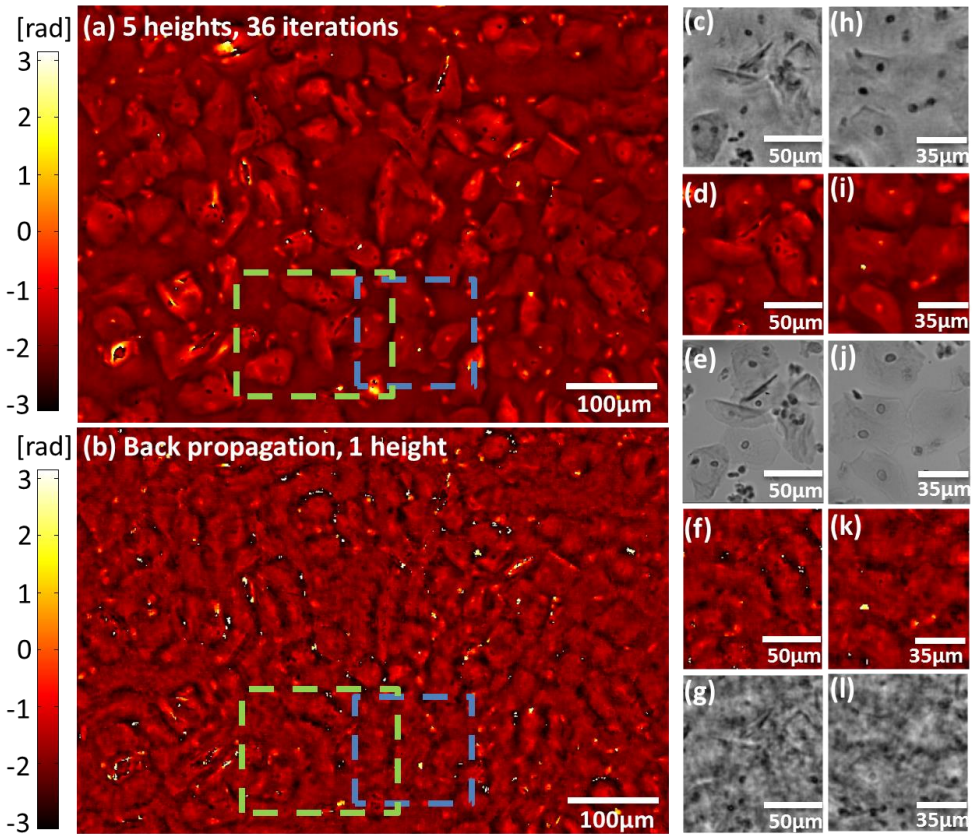


Figure 3.3 (a) Multi-height based pixel super resolution lensfree phase image of a Pap test is shown. This image was reconstructed using five heights. 36 iterations were used during phase recovery (λ = 550nm). **(b)** Single height back propagated pixel super resolution phase image is shown. **(c)** and **(d)** are multi-height based pixel super resolution lensfree amplitude and phase images, respectively, of the green dashed rectangle shown in (a). The absorbing nuclei of the cells are clearly visible in the amplitude images, while the cell's boundaries are more visible in the phase image. The corresponding 40× (0.65NA) microscope image is provided for comparison in **(e)**. **(f)** and **(g)** are the corresponding single height based back propagated phase and amplitude images respectively. **(h)** and **(i)** are multi-height based pixel super resolution lensfree amplitude and phase images, respectively, of the blue dashed rectangle in (a). The corresponding 40× (0.65NA) microscope image is also provided for comparison in **(j)**. **(k)** and **(l)** are the corresponding single height based back propagated phase and amplitude images respectively. All the phase images in the figure are wrapped since we did not employ phase unwrapping algorithms.

3.3(d,i) and (c,h), these single height back projection images show significant spatial distortion due to the density of the cells. Figures 3.3(e) and (j) also provide 40× objective lens (0.65NA) microscope comparison images for the same zoomed regions, clearly providing a decent match to our multi-height reconstruction results shown in Figures 3.3(d,i) and (c,h). *Especially note the enhanced contrast of the cell boundaries in our phase images (Figs. 3.3(d) and (i)), which is complementary to the spatial information coming from our amplitude images (Figs. 3.3(c) and (h))*. This complementary set of information that is conveyed by the amplitude and phase images might facilitate detection of abnormal cells within a Pap test that are characterized for instance by a high nuclear-cytoplasmic ratio. It is also important to note that all the phase images reported in our manuscript are wrapped; hence, for the multi-height reconstructed phase images, phase jumps should be expected in absorbing areas of the cells (e.g. nuclei), where phase would not be properly defined. Contrary to the phase images, these absorbing areas will be of high contrast in their corresponding lensfree amplitude images, which once again emphasizes the complementary nature of phase and amplitude lensfree image channels.

Next we investigated how the number of intensity measurements used in our iterative reconstruction process affects the image quality (see Fig. 3.4). To provide a fair comparison (i.e., to better isolate the source of improvement in image quality), a total of 144 Fourier transform pairs were used in each case, regardless of the number of intensity measurements employed in the multi-height based phase recovery. Moreover, all the phase images are wrapped and the same global phase was assigned to all of the images to avoid different phase jumps in different images. Fig 3.4(a) shows a single height back propagated phase image. When a second intensity measurement is added, multi-height based iterative phase recovery approach can be utilized. Consequently, the recovered phase image after 72 iterations (see Fig. 3.4(b)) looks significantly

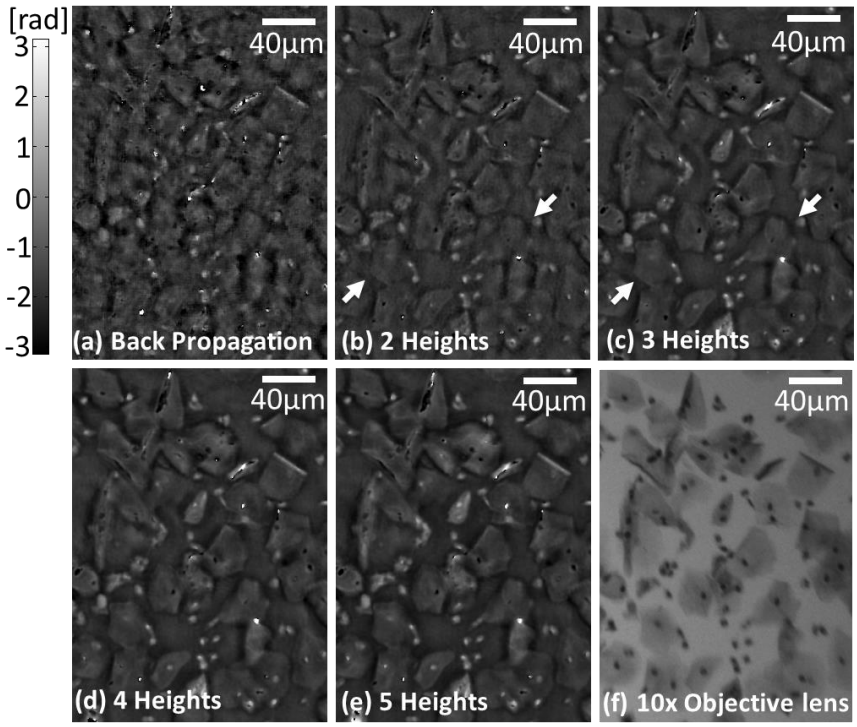


Figure 3.4 Pap smear reconstruction results acquired for different number of lensfree diffraction intensities. **(a)** Back propagated image from one pixel super-resolved lensfree hologram. **(b)**, **(c)**, **(d)** and **(e)** Multi-height based pixel super-resolution lensfree phase images from two, three, four and five heights, respectively (same color bar as in (a)). For fair comparison 144 Fourier transform pairs were used in each reconstruction case. **(f)** 10× objective lens (0.25 NA) microscope image is provided for comparison purposes. The cell's boundaries are more visible in our phase images, while the absorbing nuclei of the cells are better visualized in our amplitude images as illustrated in Fig. 3.3.

better than the phase image of Fig. 3.4(a). A further improvement in image quality is achieved by adding a third intensity measurement to the multi-height phase recovery process (Fig. 3.4(c)). After 36 iterations (i.e., corresponding to a total of 144 Fourier transform pairs as before), the cells that were hidden in the noisy background are now visible (see white arrows in Fig. 3.4(c)). A moderate improvement is noticed in the image contrast when adding more intensity measurements, as can be seen in the reconstructed multi-height phase images from four and five

heights (Fig 3.4(d) and (e), respectively). Note that in these two cases, 24 and 16 iterations were used, respectively, so that the total number of Fourier transform operations remains the same in all reconstructions shown in Figs. 3.4(b) to (e), which helps us to isolate the source of the phase reconstruction improvement and relate it to multiple height measurements rather than the number of back-and-forth digital propagation operations. Fig. 3.4(f) shows a microscope comparison image (10×, 0.25 NA) for the same region of interest. Note also that the cell's boundaries are more visible in our phase images, while the absorbing nuclei of the cells are better visualized in our amplitude images as illustrated in Fig. 3.3.

After validating the usefulness of pixel super-resolved multi-height based phase recovery approach with dense blood smears and Pap tests, we experimentally tested its impact on the reconstructed image quality. An important question that we aimed to address with this additional experiment was whether or not the digital cross registration process among different Z2 lensfree holograms results in spatial smearing of our reconstructed images. Therefore we compared the imaging performance of our multi-height reconstruction results against a single back-propagated super-resolved hologram. For this end, we imaged an isolated 'UCLA' pattern that was etched on a glass slide using focused ion beam (FIB) milling, where the letters 'U' and 'C' are ~1 μm apart. *We emphasize here that for such an isolated object multi-height based image reconstruction is not necessary*. *Since we aim to understand the impact of multi-height cross registration related issues, in this final experiment we chose an isolated object ('UCLA') so that the back-propagation result of a single height SR hologram could work for comparison purposes.* This is quite different from the dense objects/specimens reported in Figs. 3.2 to 3.4, where back-propagation of a single height lensfree pixel super resolved hologram fails, requiring the use of multiple height measurements.

For this final experiment, the single height back propagated super resolved holographic image is shown in Fig. 3.5(e), where the letters ‘U’ and ‘C’ are clearly separated. The ‘UCLA’ pattern is spatially isolated from nearby objects, and therefore for this small isolated FOV phase recovery is not necessary as emphasized earlier. Figs. 3.5(a) to (d) show multi-height based reconstructed amplitude images, for two, three, four and five different heights, respectively (λ = 490 nm). For fair comparison among these recoveries, once again the number of Fourier transform pairs was kept constant in each case, as a result of which each reconstruction used a different number of iterations (60, 30, 20 and 15 iterations, respectively). It is evident that the letters ‘U’ and ‘C’ are clearly separated in all of these images, which is an indication of our success in cross registration of different height super-resolved holograms to each other so that spatial smearing affects due to possible inconsistencies among different Z2 lensless holograms are minimized. A microscope comparison image of the same “UCLA” pattern can also be seen in Fig. 3.5(f), acquired using a 40× objective lens (0.65 NA).

3.3 Discussion

We demonstrated that by incorporating pixel super-resolved partially-coherent lensfree imaging with a multi-height phase recovery approach, dense and connected samples can be reconstructed over a large FOV (~24 mm^2). The multi-height iterative phase recovery approach uses multiple super-resolved intensity measurements, which are acquired at different sample-to-sensor distances. Unlike mainstream object-support based phase recovery methods, the multi-height based phase recovery approach does not need a spatial mask for objects. As a proof of concept, this pixel super-resolved partially-coherent multi-height lensfree imaging approach was tested on Pap smears and whole blood samples. Color imaging results are not shown here, however using the same multi-height lensfree imaging approach at three different wavelengths

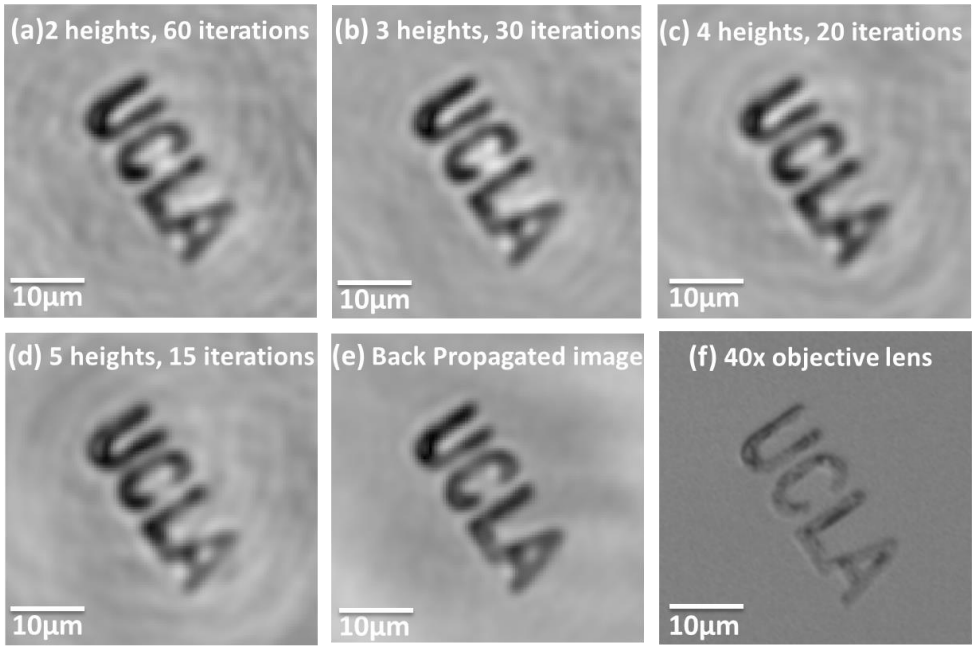


Figure 3.5 Adding intensity measurements from different Z_2 distances does not degrade the image resolution. An important question that we aimed to address with this additional experiment was whether or not the digital cross registration process among different height lensfree holograms results in spatial smearing of our reconstructed images. Therefore we compared the imaging performance of our multi-height reconstruction results against a single back-propagated super resolved hologram. **(a)**, **(b)**, **(c)** and **(d)** are multi-height based pixel super-resolved lensfree amplitude images, where two, three, four and five different heights were used in the reconstruction process, respectively (λ = 490nm). **(e)** Single height based back propagated pixel super-resolved amplitude image. For fair comparison the number of Fourier transform pairs was equal in each case, such that each reconstruction used different number of iterations. In all of these reconstructed images, the letters "U" and "C", with a spacing of ~1 µm, are clearly separated. **(f)** Microscope comparison image of the same sample (40× objective lens; 0.65 NA).

(e.g., λ = 450 nm, 550 nm and 650 nm) and combining these lensfree images to generate color images of the specimens should be straightforward[79]. Finally, we should also mention that translating the same lensfree microscopy platform into reflection geometry is also feasible, although a reduction in imaging field of view would be expected as previously demonstrated[15].

3.4 Theory and methods

Overview of phase recovery methods: In digital holography, the optical phase information of the scattered object field cannot be directly measured and is actually encoded into intensity oscillations of the recorded hologram. Therefore, for reconstruction of images using digital holographic data, phase recovery is of paramount importance. There have been several different approaches to tackle this important problem, and depending on the hologram recording scheme and its complexity, the degree of success varies[21,37,40,80–83].

The goal of phase recovery in our context is to extract a complex-valued object function from the intensity of its diffraction pattern. Note that in our partially-coherent holographic microscopy scheme described in Fig. 1.1, since the specimens are placed rather close to the detector array (e.g., $Z_2 \sim 0.7$-1 mm), the object field-of-view roughly equals to the detector active area. And due to partial-coherence of illumination there is no longer a single Fourier transform relationship between the entire object and detector planes. In fact, using the transfer function of free-space (equation (2.7)) one can digitally propagate back and forth between the object and detector planes through two successive Fourier transform operations. Therefore, the number of effective pixels (P) at the diffraction sampling plane equals to the number of useful pixels at the object plane. On a related note, the basic function of pixel super-resolution techniques in lensfree digital in-line holography is actually to increase the value of P beyond what the sensor chip can provide at the circuit level[6] .

As a result of this, for a complex-valued object function, phase recovery problem becomes undetermined by a factor of 2 since there are $2 \times P$ pixels defining the object function (P pixels for the real part and P pixels for the imaginary part), whereas there are only P pixels in the measurement matrix[38]. In order to solve this underdetermined phase recovery problem, new

information about the object function needs to be acquired and incorporated as a constraint on the solution space.

To provide a solution to this important problem, numerous iterative phase recovery algorithms were devised[34,39,41,47,80,84,85], where various different types of information about the object were used as constraints. These object constraints, together with the measured diffraction pattern were enforced at each step of the iterations, gradually converging to the missing 2D phase information[86]. The object-support constraint, which specifies the locations of the objects as a binary mask, is one of the most commonly used constraints[75], which also formed the basis of some of our earlier work[5,25,87]. This binary mask is a matrix, where a value of one is assigned to the binary mask wherever the object is located, and a zero is assigned wherever the background appears. This way, the object-support constraint or the spatial mask provides the coordinates for which the object function is zero, which effectively reduces the number of unknowns in our underdetermined phase recovery problem.

While quite effective[9,37], object-support based iterative phase recovery techniques encounter practical challenges in digital in-line holography when the density of the sample is relatively high, which makes it difficult to create an appropriate binary mask that can effectively reduce the number of unknowns at the object plane. This issue can affect convergence of iterative phase recovery techniques, yielding sub-optimum reconstructions of dense object functions. To overcome these hurdles, several methods were devised which in practice are restricted to sparse objects and/or to relatively small imaging field-of-views[88–90].

In this work, we utilized an iterative phase recovery method together with a pixel super-resolution technique that uses multiple diffraction intensity measurements of the objects captured at different planes along the light propagation direction. Each additional lensfree diffraction

measurement captured at a different object height brings a new set of equations to help us solve this underdetermined phase recovery problem *without* the use of any object-support constraint or spatial masks. In the literature, there are various methods that one can use to retrieve the lost phase information from two or more diffraction intensity measurements, such as transport-of-intensity equation (TIE) based methods[82,83,91,92], iterative methods which use these diffraction measurements as successive amplitude constraints[40,93] and other non-iterative methods[94,95]. Furthermore, multiple defocused images are also utilized in phase diversity methods, where phase aberrations of incoherent imaging systems can be characterized[96–98]. In this work, we followed the multi-height iterative method[40] due to its simplicity and robustness.

Image registration among multi-height lensfree super-resolved holograms: In our multi-height imaging based iterative reconstruction scheme, we synthesize *M* pixel super resolved holograms, one for each object height (Z_2) - see Fig. 3.1. However, among these *M* super-resolved holograms there might be spatial discrepancies since the object might have shifted and/or rotated between the acquisitions of each lensfree image stack. Therefore, we perform a digital registration step after the synthesis of these super-resolved holograms to ensure that each hologram essentially looks at the same object field-of-view. This registration procedure is based on arbitrary selection of three points (*control-points*) in one hologram (i.e., the reference hologram, typically the one with the lowest Z_2-distance) and finding the matching three points in the other *M-1* lensfree holographic super-resolved images. These control points should be close to the corners of the image in order to achieve small registration errors (~2 μm or less) over relatively large distances (e.g., ~5 mm). Moreover, these control points should better be circularly symmetric since normalized-correlation, which is used to find the shift of each control-point between the images, is sensitive to rotation. Quite conveniently, the acquired lensfree

images are in-line holograms, and an ergo isolated object (like a dust particle) in the object plane resembles an airy function in the hologram domain and exhibits circular symmetry. Therefore, in-line lensfree holograms of these dust particles or substrate defects, which are common in most samples, are desirable candidates to serve as control points. If needed, isolated spatial marks (in the form of e.g., dots) can also be placed to the corners of a sample slide to serve as predetermined control points.

After selection of the control points, a small area (e.g., ~30 × 30 μm) around each control point is cropped and digitally interpolated (~4-6 times) to serve as a normalized correlation template. Furthermore, for accurately finding the coordinate shift of each control point among *M* images, lensfree holographic images have to be positioned in the same Z_2-distance. Therefore, the difference in the Z_2-distance between lensfree holograms acquired at different heights is evaluated by an auto-focus algorithm[62,77], which permits us to digitally propagate the selected correlation templates to the same Z_2-distance, where normalized correlations are calculated to find the coordinate shifts between the control points in each image. After each control-point's coordinates are known in every image, *M-1* affine transformations are built to register these lensfree holographic images to the reference image, such that all the lensfree holograms acquired at *M* different heights can be digitally registered to each other.

Autofocus algorithm: In order to automatically obtain the depth position (Z_2 distance) of an object within the sample volume, an autofocus algorithm based on Sobel gradient magnitude is adopted[62,77]. By using digital back propagation as previously discussed, images at different planes (Z_2 distances) are obtained, and the "sharpness" measure (F) is calculated for each image. The maximum "sharpness" measure corresponds to the correct Z_2 distance i.e., the axial plane of

the object. For an amplitude image (A) containing $M \times N$ pixels, the "sharpness" measure (F) is defined as:

$$F(A) = \frac{1}{MN} \sum_{m=1}^{M} \sum_{n=1}^{N} (\nabla S(m,n) - \overline{\nabla S})^{2}. \quad (4.1)$$

Where $\nabla S(m,n)$ is the Sobel gradient magnitude and $\overline{\nabla S}$ is its mean value, the gradient magnitude is calculated by using:

$$\nabla S(m,n) = \sqrt{\nabla S_x(m,n)^2 + \nabla S_y(m,n)^2}, \quad (4.2)$$

where $\nabla S_x(m,n)$ and $\nabla S_y(m,n)$ are the result of convolving the input image (A), with the Sobel operators in the horizontal and vertical directions respectively (equation (4.3)). These resulting matrixes are approximations of the horizontal and vertical derivative:

$$\nabla S_x(m,n) = \begin{pmatrix} -1 & 0 & 1 \\ -2 & 0 & 2 \\ -1 & 0 & 1 \end{pmatrix} * A \; ; \; \nabla S_y(m,n) = \begin{pmatrix} 1 & 2 & 1 \\ 0 & 0 & 0 \\ -1 & -2 & -1 \end{pmatrix} * A; \quad (4.3)$$

where $*$ represents a 2D convolution operation. This method offers a simple way for finding the focus in an automated fashion without the need for any feedback or quantified measurement from the scanning stage or the experimental setup.

Phase recovery using M pixel super-resolved lensfree holograms: In order to retrieve the phase information and consequently eliminate the twin image artifact in our multi-height lensfree imaging approach, a modified Gerchberg-Saxton (GS) algorithm is utilized[93]. This modified GS algorithm is based on *M* intensity measurements that are taken at different Z_2 planes (see Fig. 1.1). The lowest measurement plane is typically taken with a Z_2 value of ~700 μm (which will be referred as intensity measurement #1). Note that to achieve a measurement with a lower Z_2 distance; the sensor's protective glass will have to be removed. The highest intensity measurement is typically taken with a Z_2 value of ~1 mm (referred as intensity measurement #*M*).

The distance (ΔZ) between two sequential intensity measurements is ~50 μm. We achieved this ΔZ value by using glass cover slips of different thicknesses.

In our iterative phase recovery process, we used the transfer function of free-space[5] (equation (2.7)) to propagate the fields back and forth, where the amplitudes of the *M* intensity measurements serve as constraints at each plane. To initiate the phase recovery process, a zero-phase is assigned to the object intensity measurement. One iteration during this phase-recovery process can be described as follows: Intensity measurement #1 is forward propagated (with zero initial phase) to the plane of intensity measurement #2 (see Fig. 3.1 green arrow). Then, the amplitude constraint in measurement #2 is enforced while the calculated phase resulting from forward propagation remains unchanged. The resulting complex field is then forward propagated to the plane of intensity measurement #3, where once again the amplitude constraint in measurement #3 is enforced while the calculated phase resulting from forward propagation remains unchanged. This process continues until reaching the plane of intensity measurement #*M*. Then instead of forward propagating the fields of the previous stages, back propagation is used (see Fig. 3.1 yellow arrow). The complex field of plane #*M* is back propagated to the plane of intensity measurement #*M-1*. Then, the amplitude constraint in measurement #*M-1* is enforced while the resulting phase remains unchanged. The same iteration continues until we reach the plane of intensity measurement #1. When one complete iteration is achieved (by reaching back to the plane of intensity measurement #1), the complex field that is derived in the last step will serve as the input to the next iteration. Typically, 1-70 iterations are required for satisfactory results, and for final object reconstruction step the acquired complex field of any one of the measurement planes can be back propagated to the object plane to retrieve both phase and amplitude images of the dense specimens on the chip.

Sample preparation: Blood smear samples were prepared using whole blood (UCLA Blood Bank, USA), where the samples were diluted (×2) with RPMI (Thermo Scientific, Catalog #: SH3002701) in room temperature. Then 5μL of the diluted blood was dropped on a type-one glass cover slip (Fisher Scientific Catalog # 12-548-A). The blood droplet was then smeared by a second cover slip by applying a constant force. The sample was then left to dry in air for ~ 10 minutes before being fixed and stained by HEMA 3 Wright-Giemsa staining kit (Fisher Diagnostics). The Pap smear was prepared using a standard SurePath (BD Inc.) procedure[78].

Chapter 4 Lensfree color imaging

Lensfree on-chip imaging techniques have shown great promise in addressing diagnostics and biomedical research challenges that require both a large FOV and a high spatial resolution. However, color imaging has remained relatively immature for lensfree holographic on-chip imaging since a 'rainbow' color artifact appears in the reconstructed images. In this chapter, I will demonstrate and compare two computational methods to mitigate this 'rainbow' color noise. The computational implementation of these two colorization methods is inexpensive and they preserve both the wide FOV and the sub-micron spatial resolution of lensfree on-chip microscopy. The first method that was introduced, YUV color space averaging, separates the color information from the brightness, thus allowing averaging only the colors of the image, while maintaining the gray-scale image with high resolution. This method is very robust and does not require any prior knowledge about the colors of the object. The second method is based on Dijkstra's shortest path algorithm and it requires prior knowledge about the number of dominant colors or the stains within the imaged object/sample. The proof of concept of this lensfree color microscope using both of these colorization methods was demonstrated by imaging Pap smear samples over a wide FOV of ~14 mm^2 with sub-micron spatial resolution and reliable color reproduction. Parts of this chapter have already been published in Greenbaum, A., Feizi, A., Akbari, N. & Ozcan, A. Wide-field computational color imaging using pixel super-resolved on-chip microscopy. *Optics Express* **21**, 12469-12483 (2013).

4.1 Introduction

Color imaging using a lensfree holographic microscope is still relatively immature. Color has a paramount role in biomedical imaging; for example color staining acts as a contrast mechanism

to differentiate various cell types. Moreover, color has an essential psychological effect as the end users of imaging systems such as pathologists and cytotechnologists are accustomed to observe specimen in color. In general, color images in lensfree holographic microscopy can be rendered by acquiring three high-resolution holograms of the same object[99–102], each with a different illumination wavelength, typically Red, Green and Blue (RGB). Combining these holographic images with or without additional processing can create an RGB image of the object[79,103–105]. However, a 'rainbow' like color artifact appears in the resulting RGB image (see for example Fig. 4.1(a)), which cannot be entirely removed even after preforming object-support based phase-recovery (see Fig. 4.1(b)). Similar rainbow like color artifacts also exist in lens-based holographic color imaging techniques[104].

The relative strength of the 'rainbow' color artifact in digital holography depends on the image acquisition and reconstruction schemes. By and large, any noise term (e.g., speckle noise, multiple reflection interference terms) or reconstruction artifacts that vary their spatial patterns/signatures as a function of the illumination wavelength would create 'rainbow' like color noise as different color holograms (e.g., red, green and blue) are reconstructed and digitally super-imposed to create a color image. More specific to digital in-line holography[79,103,104], a significant source of this rainbow artifact can be considered to be the twin image noise that exhibits different ripple frequencies at different illumination and reconstruction wavelengths. Since the twin image artifact is nothing but the residue of a defocused (i.e., diffracted) object function, its physical dependency on wavelength of light is due to free space diffraction of light that is scattered from an object. Similar to how a grating would disperse different colors of light, an object's twin image artifact or its residue will also exhibit similar wavelength dependent diffraction patterns. As a result of this, when three reconstructed holograms, acquired with e.g.,

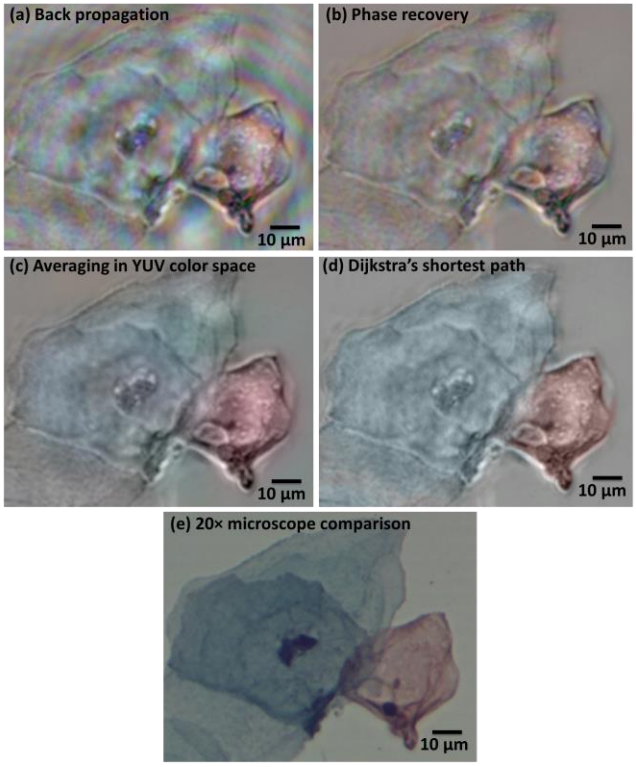


Figure 4.1 (a) A lensfree color image that was created by three high-resolution reconstructed holograms, where each hologram was acquired with a different illumination wavelength (λ = 460 nm, 530 nm and 630 nm). The 'rainbow' color artifact is evident. **(b)** Object-support based phase-recovery was applied on each of the three high-resolution holograms, and then the resulting super-resolved images were combined into one RGB color image, where the 'rainbow' color artifact is still apparent. **(c)** The result of colorization method #1 (YUV color space averaging). **(d)** The result of colorization method #2 that is based on Dijkstra's shortest path. For both (c) and (d), the 'rainbow' color artifact is clearly eliminated, while the spatial resolution is maintained. **(e)** A 20× objective (0.5 NA) microscope image of the same sample.

red, green and blue illumination wavelengths, are combined to form an RGB image, the superposition of the twin-image noise or its residues would create 'rainbow' like color artifacts. In addition to twin image, coherence of illumination, both spatially and temporally, might also contribute to the 'rainbow' color noise observed in holographic images. For instance speckle noise and multiple reflection interference (due to partial reflections that occur at e.g., substrate-

air interfaces) are also functions of the illumination wavelength, and would therefore create similar 'rainbow' like artifacts if different color holographic images are directly merged together[105].

Here we introduce and compare two new methods to eliminate 'rainbow' like color artifacts in lensfree holographic on-chip microscopy, without compromising the spatial resolution or wide FOV of lensfree reconstructed images (see Figs. 4.1(c) and (d)). The first method (see Fig. 4.2) averages only the color components of an image, while preserving the brightness (gray-scale) component. This can be realized by transforming the RGB image to a different color space such

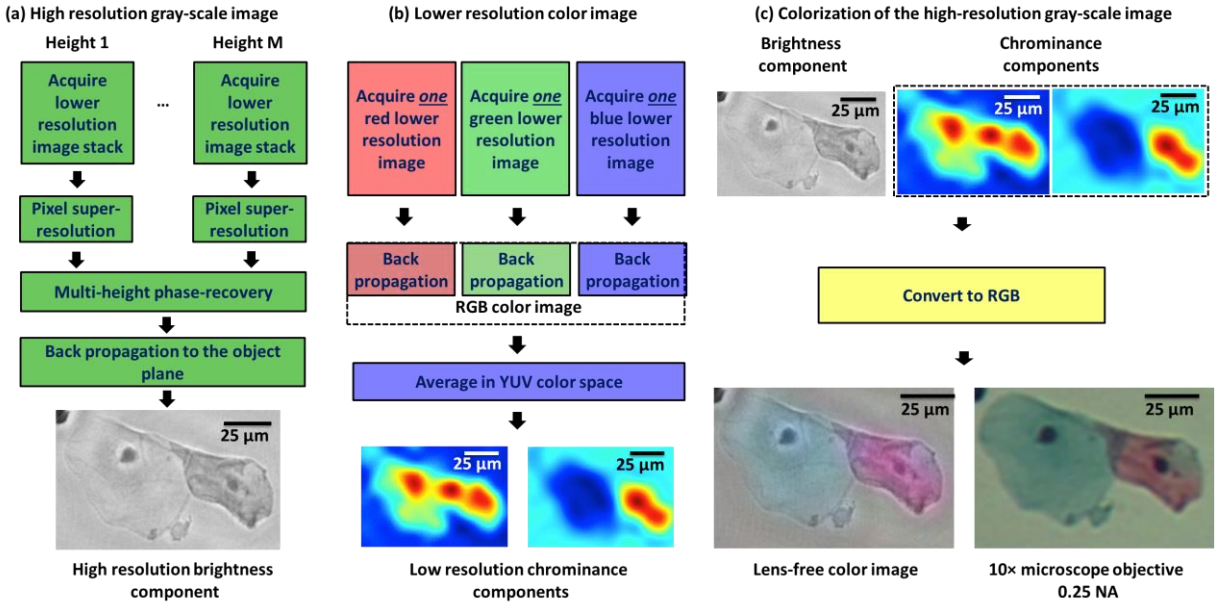


Figure 4.2 (a) The computational flowchart for acquiring and obtaining a high-resolution (i.e., pixel super-resolved) gray scale image using a single illumination wavelength (λ = 530 nm). **(b)** The computational flowchart for acquiring and obtaining one lower-resolution color image. This RGB image is then converted into YUV color space, where the color or chrominance channels (UV) are averaged. **(c)** The high-resolution brightness component from (a) is added to the averaged color components (UV) in (b), and the resulting image is converted into RGB color space to obtain a high-resolution lensfree color image, which provides decent color reproduction without sacrificing spatial resolution.

as the YUV color space, which separates the brightness component of an image from its color components[106]. In the second method (see Fig. 4.3), a colorization algorithm that relies on Dijkstra's distances to propagate colors from automatically generated color patches to the entire FOV is utilized to create a lensfree color image[107–109]. By using either one of these methods together with pixel super-resolution and multi-height phase-recovery approaches[40,110–112], lensfree on-chip color microscopy can provide wide FOV (~14 mm^2) images with sub-micron spatial resolution and accurate color reproduction. In addition to removal of the rainbow color artifacts, with both of these colorization approaches the image acquisition and processing times are improved by factor of ~3 compared to obtaining high-resolution holograms at each color channel (red, green and blue). To demonstrate the color imaging capability of this on-chip microscopy platform, Pap smears were successfully imaged. The significantly improved color rendering capability of our lensfree pixel super-resolution microscopy platform opens up new avenues for wide-field imaging of stained samples that are commonly used in e.g., diagnostics or biomedical research.

4.2 Results

As briefly discussed in our introduction, a straightforward approach for rendering a lensfree color image involves the acquisition of three high-resolution (i.e., pixel super-resolved) holograms each with a different illumination wavelength (typically red, green and blue). These three high-resolution holograms can then be reconstructed and combined into one RGB image, such as the one shown in Fig. 4.1(a). The 'rainbow' color artifact is quite apparent in this image, and it cannot be mitigated even after applying object-support based phase-recovery with a tight mask (see e.g., Fig. 4.1(b)). On the other hand, this color artifact can be effectively mitigated using colorization method #1 by spatial averaging of the color information, while preserving the

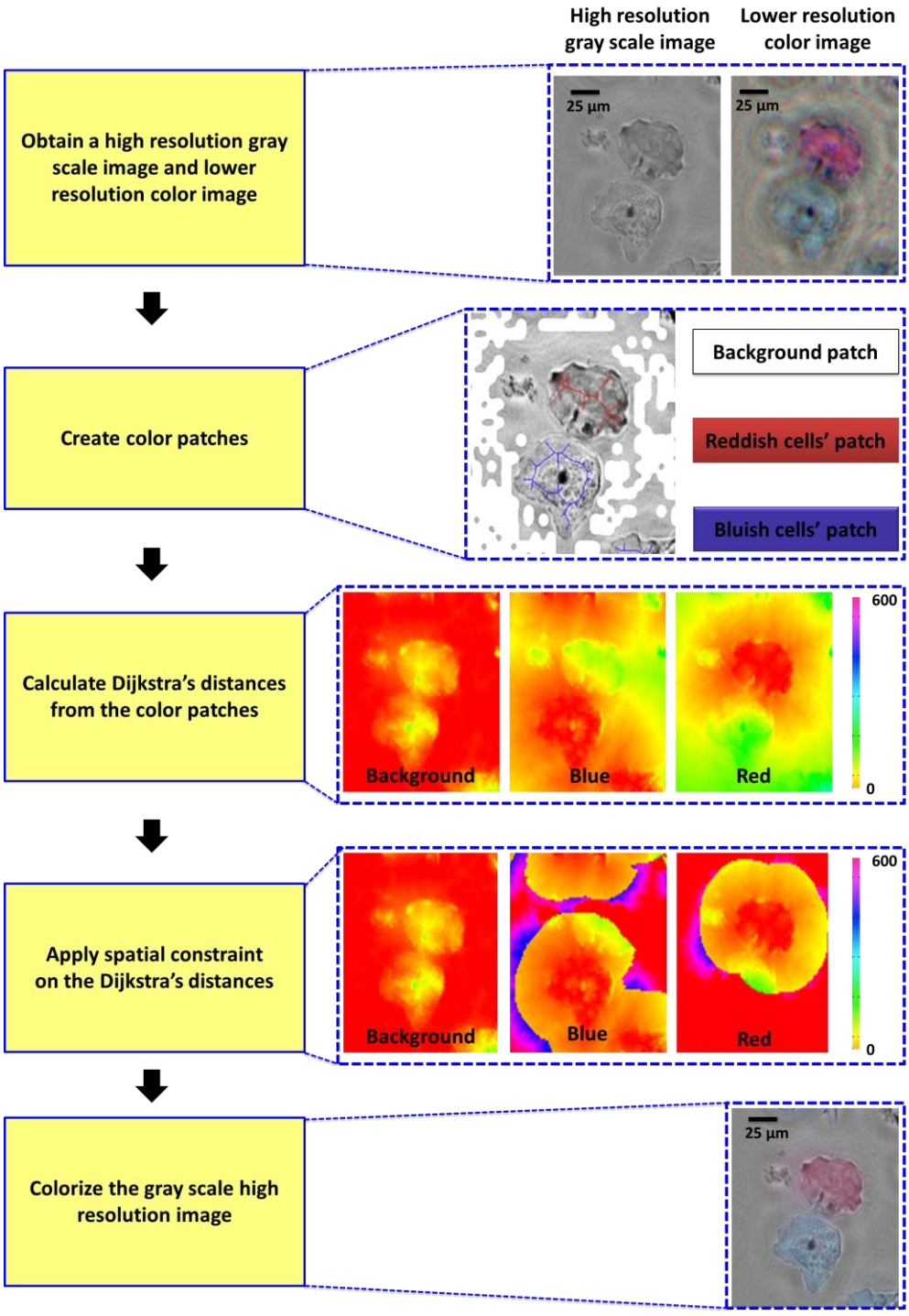


Figure 4.3 A block-diagram that describes the computational steps that are performed in the colorization approach (method #2) based on Dijkstra's shortest path algorithm. This colorization process automatically assigns color patches, which are later propagated to the entire image FOV.

brightness information (see section 4.4). The resulting image, through application of method #1 exhibits a significantly improved color rendering and the 'rainbow' artifact is now eliminated as shown in Fig. 4.1(c). Similar results are also obtained using method # 2 (see section 4.4) through the use of Dijkstra's modified shortest path algorithm, as illustrated in Fig. 4.1(d).

To quantify the spatial resolution of our lensfree microscope, a 1951 USAF resolution test chart was imaged according to the flowchart in Fig 4.2(b). In the acquisition process 36 lower resolution holograms were acquired for each height, and in total three heights were used for the multi-height phase-recovery process (Z_2 = 270 μm, 392 μm and 440 μm). As can be seen in Fig. 4.4 the entire USAF resolution target was clearly resolved, including the smallest grating line in group 9 element 3 with a width of 0.78 μm.

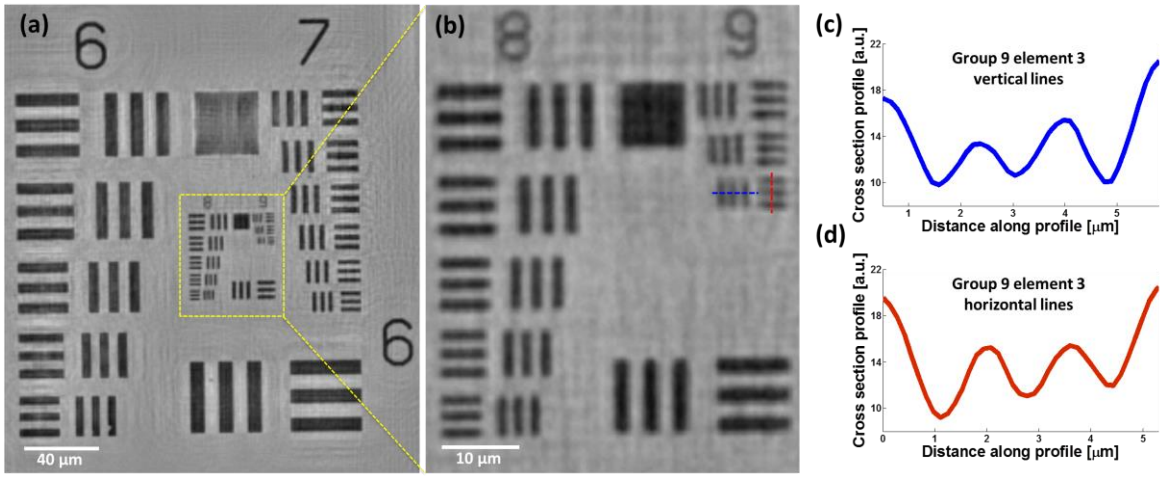


Figure 4.4 (a) A lensfree amplitude image of a 1951 USAF resolution test chart, which was acquired using the computational flowchart described in Fig. 4.2(b). In this experiment, three high-resolution holograms at different heights (Z2 = 270 μm, 392 μm and 440 μm) were recorded. **(b)** Zoomed in region of (a) reveals that the entire USAF test chart was resolved. The third element in-group nine corresponds to a grating with a line width of ~0.78 μm. **(c)**, **(d)** Cross-sections of the vertical and horizontal gratings of element three in group nine, respectively.

One important application of this wide FOV and high-resolution computational color microscope could be in cervical cancer pre-screening by imaging Pap smears. Pap test is a cytology based screening test used to detect premalignant and/or malignant cells that indicate the development of cervical cancer, which is the second most common cancer type among women worldwide[113]. Pap tests require a wide FOV since typically only one out of thousands of cells is premalignant; and furthermore high-resolution color imaging capability is rather important as different cell types are stained with different colors. Our partially-coherent lensfree color microscope can address all of these requirements, and to illustrate its proof of concept Fig. 4.5 shows the image of a wide FOV Pap smear sample that is reconstructed using our lensfree holographic microscope based on colorization method #1. In the image acquisition process 36 lower resolution holograms were acquired for each height, and in total three heights (Z_2 = 449 μm, 550 μm and 592 μm) were used for multi-height phase-recovery. Our lensfree color images shown in Fig. 4.5 are in very good agreement with 10× microscope objective (0.25 NA) color images that are provided for comparison purposes.

4.3 Discussion

Colorization is the task of assigning colors to a gray-scale image or a film, and it has traditionally been a labor-intensive task that eventually resulted in various computational approaches expediting the colorization process[108,114]. In this chapter, I have demonstrated a novel colorization method to mitigate the 'rainbow' color artifact in lensfree holographic on-chip microscopy, by averaging only the color information of the reconstructed image while preserving its brightness. Furthermore, inspired by the colorization literature[108,114], and under the assumption that various biomedical objects have only a discrete number of stains or colors, we have also modified and implemented a fully automated colorization method based on Dijkstra's

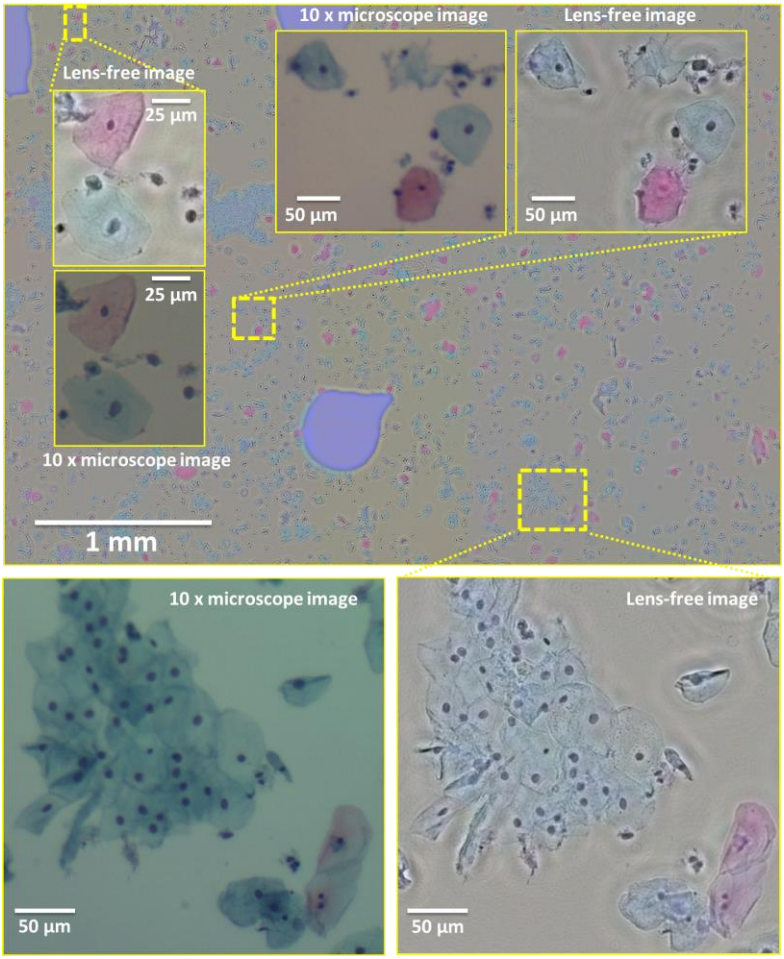


Figure 4.5 Wide FOV (~14 mm^2) lensfree color image of a Pap smear sample (ThinPrep® preparation[115]). The color image was obtained using colorization method #1, i.e., averaging in the YUV color space. Three digitally zoomed in regions are provided and are compared to 10× objective lens (0.25 NA) microscope images. To mitigate the twin image noise three heights (Z_2 = 449 µm, 550 µm and 592 µm) were used for multi-height phase-recovery. The large blue spots are permanent marker spots that were scribed on the sample for 2D mapping and image comparison purposes.

shortest path algorithm (Fig. 4.3). This automated colorization algorithm is an alternative to our method #1, i.e., the YUV color space averaging method (Fig. 4.2). Similar to method #1, in this modified Dijkstra colorization algorithm, inputs are (1) a high-resolution (pixel super-resolved) gray scale image and (2) a lower resolution RGB color image of the same object. The algorithm

automatically creates the color patches or scribes for three different classes of colors (red, blue and no color i.e., background). To propagate the colors to the rest of the image FOV, Dijkstra's shortest path distances are calculated for each color patch and a spatial constraint is applied to prevent excessive color leakage (refer to section 4.4 for further details).

Note that in the context of Pap smear imaging, for both of these colorization approaches the brightness channel that is pixel super-resolved contains the cell and nucleus boundary information of the specimen, and therefore a sub-micron resolution for the brightness channel is rather important for possible clinical applications of this approach in e.g., point of care settings. On the other hand, the color stains used in creating e.g., a Pap smear are used as visual markers for potential cells of interest, and therefore the spatial sharpness of the boundaries of these stains is less significant compared to the super-resolved brightness channel of the same specimen. As a matter of fact, the diffusion of the dye molecules within the staining process itself creates some resolution loss in the colorized boundaries of the specimen.

We also compared the performances of these two colorization approaches (Methods 1 and 2) using a confluent region of a Pap smear sample (see Fig. 4.6(a)) as well as a sparse region of the same sample (see Fig. 4.6(b)). Remarkably, these results illustrate that two entirely different methods provide very similar colorization performance under different sample densities. Overall, the YUV color space averaging preformed slightly better than the modified Dijkstra approach since the latter could not fully colorize the cells or specific areas of the sample that are indicated by the yellow arrows in Fig. 4.6. In Fig. 4.6(a) the yellow arrow points to an area where the color is a mixture of red and green, while in Fig. 4.6(b) the yellow arrow points to a cell which has a light red color. One solution to further improve the performance of the Dijkstra approach could be to discretize and represent each color of the image with more discrete levels, which could

potentially help eliminate some of the relatively faint colors reported with the yellow arrows in Fig. 4.6.

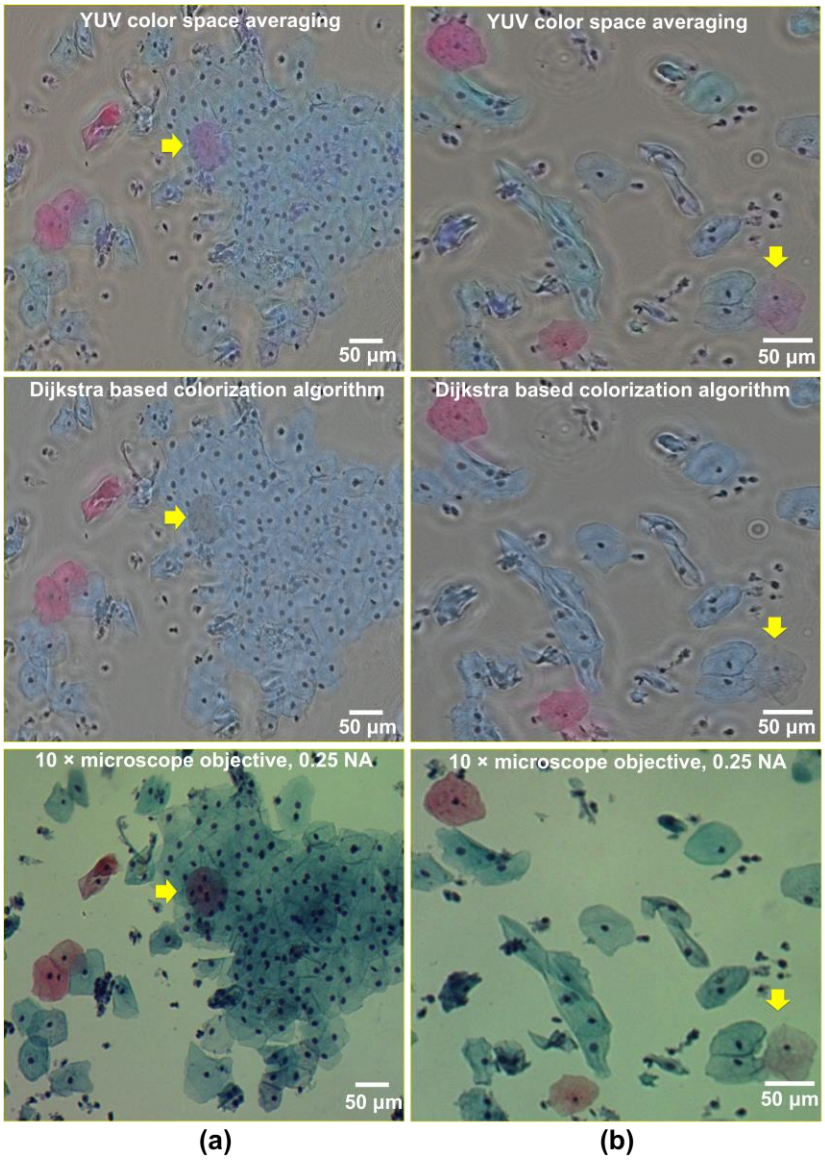


Figure 4.6 A comparison between the YUV color space averaging method (#1) and the method (#2) that is based on Dijkstra's shortest path. The yellow arrows indicate locations where the YUV color space-averaging method successfully colorized the image, while the Dijkstra's shortest path based algorithm was less successful for the same arrow locations. A confluent region and a sparse region of the Pap smear sample are shown in **(a)** and **(b)**, respectively.

4.4 Theory and methods

Colorization Method 1: YUV color space averaging: To mitigate the 'rainbow' color artifact in the reconstructed holographic images (see e.g., Figs. 4.1(a) and (b)), in our image acquisition scheme first a super-resolved multi-height phase-recovered holographic image is obtained with only one illumination wavelength (λ = 530 nm) using 6 × 6 = 36 shifts of the source aperture. This super-resolved image provides the high-resolution brightness component (Y) of our lensfree color image (see Fig. 4.2(a)). To obtain the color information, three lower resolution holograms (i.e., *without* pixel super-resolution) at three different illumination wavelengths (λ = 460 nm, 530 nm and 630 nm) are also acquired, reconstructed and merged to a lower resolution RGB image (Fig. 4.2(b)). This lower resolution RGB image is then converted to the YUV color space using Colorspace Transformations package that is processed in Matlab. In this YUV color space, the brightness component (Y) is separated from the color or chrominance components (UV) and it is replaced with our pixel super-resolved high-resolution lensfree image. To obtain an artifact-free high-resolution color image, the color components (UV channels) are averaged with a rectangular window (~10 μm edge size), while the Y component of each image remained untouched containing the super-resolved phase recovered image. Finally, this hybrid YUV image is converted back to an RGB image (see Fig. 4.2(c)).

Colorization Method 2: Dijkstra's shortest path: This second colorization method (Fig. 4.3) is inspired by earlier work in video and photography colorization literature[108,114], and is adopted for lensfree holographic microscopy needs where artificial leakage of the colors outside the physical size of individual cells is digitally prevented.

At the core of this second approach is the Dijkstra's shortest path algorithm[107], a graph search algorithm that finds the shortest path from a given node (i.e., the initial node) to all the remaining nodes within the graph. This algorithm assumes that the graph is connected with only non-

negative edges, where a non-negative edge between two nodes can be considered as the cost of moving from one node to the other. The algorithm starts by assigning tentative distances to all the nodes in the graph, by calculating the accumulated edge cost in an already explored path from the initial node to a specific node in the graph. The initial node gets a zero tentative cost; while the rest of the nodes are assigned with an initial tentative distance of infinity; as the algorithm proceeds, the tentative costs of the rest of the nodes gradually decrease, until the algorithm converges to the shortest path for a given initial node. Except for this initial node, the algorithm marks all the remaining nodes in the graph as 'unvisited', and stores them in a wait-list, while setting the initial node to 'current'. The algorithm then checks the distance between the 'current' node and its neighbors. If this distance plus the tentative cost of the 'current' is less then the previously assigned tentative distance of the neighboring node, the new total distance will replace the tentative distance that was previously assigned to this neighboring node. After this step, the current node will be moved to the 'visited' list and will never be scanned again; the new 'current' node will be selected as the node in the 'unvisited' wait-list with the smallest tentative distance. The algorithm will continue until all the nodes will be removed from the 'unvisited' list, at that point the tentative distances will converge to the shortest paths from the initial node to all the other nodes in the graph.

This second colorization method that is based on Dijkstra's algorithm is composed of five computational steps:

(*i*) Obtain a high-resolution (i.e., pixel super-resolved) gray scale image and lower resolution color images of the object.

(*ii*) For each discrete color in the image, color patches are initially created by averaging and thresholding the low-resolution color image in the YUV color space[106]. For stained Pap smear

samples, we assumed that only three colors are present in the image: red, green, and no color, i.e., background. In the following three steps (*iii*-*v*), each discrete color patch is processed separately. The pixels with color values above a preset threshold value were further processed using morphological operations such as dilation, erosion and skeleton to prevent the color patches from leaking out of the cell boundaries[74].

(*iii*) The Dijkstra algorithm was utilized to find the shortest path from a collection of unicolor label patches to all the pixels across the image FOV[107–109]. To calculate the shortest path, the high-resolution gray-scale image is conceptually transformed into an undirected graph, where each pixel is a node that is connected by eight positively weighted edges to its neighboring pixels (pixels located on the boundaries of the image will have smaller number of neighbors or edges). The positive weight of each edge is defined as the absolute value of intensity difference between the two nodes that the edge is connecting. Moreover, the pixels in the unicolor label patches are all connected by an edge with zero weight. Therefore the Dijkstra algorithm will find the shortest path in terms of edge cost between each pixel in the image to the unicolor label patches. We implemented the Dijkstra algorithm using C\C++ with a binary heap that provided a computational complexity of $O(N \cdot logN)$ when N is the number of pixels in the image[108].

(*iv*) We then apply a spatial constraint to prevent the leakage of the colors outside the physical size of an individual cell. Stated differently, a typical red cell with a diameter of ~50 μm would contribute ~20 pixels that would serve as an individual red color patch. Therefore, when Dijkstra's shortest path is calculated we do not expect to find pixels that are physically far from that color patch (e.g., > 100 μm) and have a relatively small Dijkstra's distance, since these pixels are located outside the cell's boundary. Subsequently, the algorithm also tracks the ancestor patch that each pixel's distance value is originated from. If the Euclidian distance

between each pixel in the image to its ancestor patch is larger than the physical size of a typical cell we then assign this pixel a large Dijkstra distance (e.g. infinity), thus cutting off the leakage caused by that patch, which avoids color artifacts forming in our lensfree images.

(*v*) Finally, the reciprocals of the Dijkstra's distances are used as weights in order to mix the UV values of all color patches and determine the optimum UV value for each pixel of the reconstructed lensfree image[108].

Chapter 5 Imaging of pathology slides using lensfree microscopy

In previous chapters I introduced the computational methods that are commonly used in lensfree imaging, Here, I demonstrate that lensfree holographic on-chip microscopy can image pathology slides over an ultra-wide FOV with a spatial resolution and contrast sufficient for pathologists to perform clinical investigation and diagnosis. Parts of this chapter have been submitted to publication and are under review.

5.1 Introduction

For pathologists, bright-field transmission microscopy is an indispensable tool used for the observation of micro-scale objects within a tissue section or a smear[116–118]. While high-resolution imaging capabilities have contributed to the optical microscope's wide spread use in clinical settings, it still has several limitations. First, a high-quality pathology microscope and its carefully crafted objective lenses are in general costly. Additionally, the microscope's FOV (the area of the specimen that can be imaged) is inversely proportional to the square of its total magnification factor, thus limiting its ability to observe large samples (e.g., whole histology slides) without mechanical scanning. While lateral scanning can expand the effective FOV of a microscope image, its usefulness is partially compromised due to the potential sample tilt and out-of-plane regions that naturally occur in large pathology samples, which necessitate dynamic focus adjustment through additional depth scanning and digital signal processing.

Here, I demonstrate that lensfree holographic on-chip microscopy can image pathology slides over an ultra-wide FOV with a spatial resolution and contrast sufficient for pathologists to perform clinical investigation and diagnosis, which was confirmed after examination by an expert pathologist. In our experiments, we imaged invasive carcinoma cells within human breast

sections, Pap smears consistent with a high-grade squamous intraepithelial lesion and sickle cell anemia blood smears. Our results constitute the first demonstration of 3D pathology slide imaging using on-chip microscopy, matching the clinical pathology needs. This milestone performance is enabled by the solution of transport of intensity equation (TIE) to generate an initial phase guess to the multi-height based iterative phase retrieval algorithm as well as rotational field transformations implemented in pixel super-resolved partially-coherent in-line holography (Fig. 5.1). This approach can not only image specimen in 3D, but also digitally correct for uncontrolled mechanical tilts and height variations between the sample and the image sensor planes, which makes it much more powerful and realistic compared to contact (i.e., shadow) imaging approaches that strictly demand flat (i.e., 2D) and parallel-placed samples with sub-micron gap precision on a chip. We believe that lensfree computational microscopy on a chip can have unique translational impact on the practice of pathology in resource limited clinical settings since this cost-effective microscope not only records high-quality images over a wide FOV, but also retrieves the complex optical field of the specimen such that the pathologist can digitally adjust the focus of the sample after image capture, providing a *virtual* depth-of-field experience for investigating sample slides, matching the manual depth adjustment that is routinely practiced in clinical examination of specimen under traditional light microscopes. Therefore, the presented platform offers medical personnel a powerful, yet cost-effective and simple tool to acquire high-resolution and clinically relevant 3D images of biological specimen across large FOVs, which is of paramount importance especially when large areas need to be inspected for diagnosis.

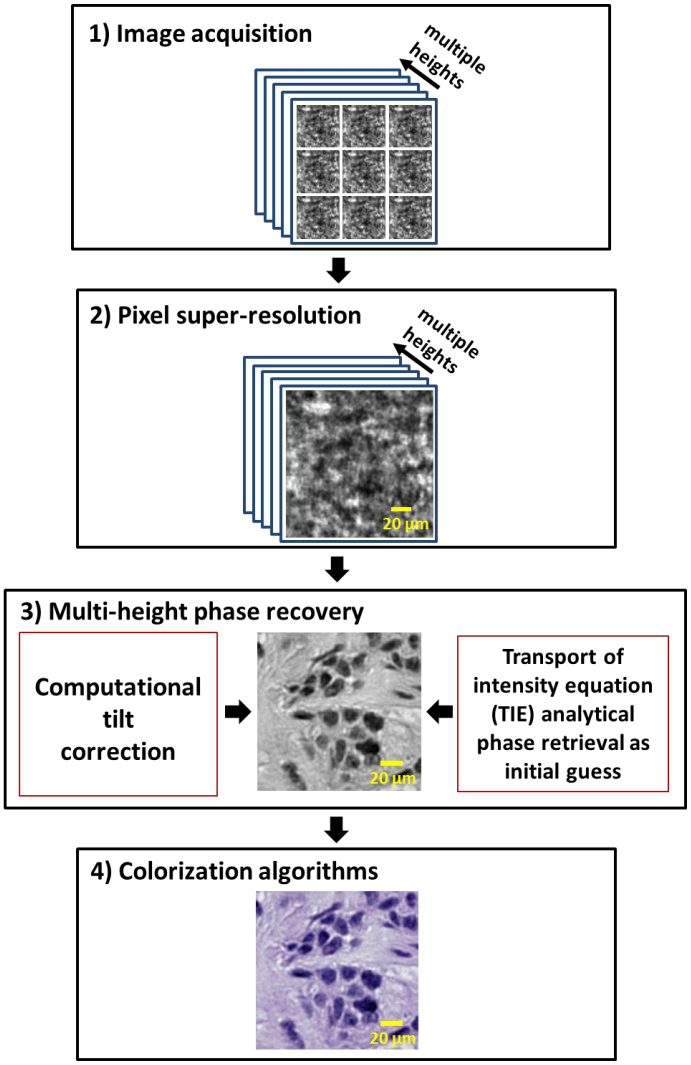


Figure 5.1. Block diagram of our image reconstruction steps in lensfree holographic on-chip imaging. The imaging process starts by capturing a sequence of low-resolution holograms, each sub-pixel shifted with respect to others at each height (Z_2 distance). Then for each height, the pixel super-resolution algorithm synthesizes a high-resolution hologram out of these multiple low-resolution holograms. These resulting "pixel super-resolved" holograms at different heights are then fed to our multi-height phase-recovery algorithm, which also includes tilt correction and field transformations to retrieve the lost phase of the optical wave, thus enabling the reconstruction of 3D images of specimen. To considerably accelerate the convergence of the iterative phase-recovery algorithm, the phase solution of TIE is used as an initial phase guess. Lastly colorization algorithms provide color representation of the lensfree reconstructed image.

5.2 Results

Wide FOV imaging of invasive ductal carcinoma cells using lensfree on-chip microscopy: Pathology slides are traditionally stained with Hematoxylin and Eosin (H&E), and the thickness of the section depends on the tissue properties and the pathologist's preference, typically ranging between 2 μm and 7 μm. To demonstrate that lensfree holographic on-chip imaging can properly image connected histology slides, we chose to image human adenocarcinoma of breast tissue slice (Carolina, Item #318766) with 7 μm thickness (Fig. 5.2). After holographic reconstruction of the slide (see section 5.4), the obtained lensfree images were shown to an expert pathologist to confirm that the image quality was sufficient for medical evaluation. Fig. 5.2(a) shows a full FOV reconstruction (FOV = 20.5 mm^2) of the slide, and to emphasize the wide FOV of lensfree imaging compared to traditional lens-based microscopy, the digital fields-of-view of 40× and 20× microscope objectives are also shown (note that these rectangular FOVs for lens-based digital microscopes are generously estimated, assuming a camera adapter with unit magnification, i.e., these FOV estimates represent upper bounds). Using the lensfree reconstructed images (Figs. 5.2(b) to (d)) the expert pathologist confirmed disorderly epithelial cell proliferation with cribriform growth. The cells exhibit nuclear enlargement, slightly irregular nuclear contours, open chromatin, and moderate delicate cytoplasm. All of these observations made by the pathologist were also in agreement with the 40× microscope objective images (NA=0.75) taken for comparison purposes (Figs. 5.2(e) to (g)). Note that the lensfree image shown in Fig. 5.2 was acquired using a single illumination wavelength (λ = 532 nm), and that is why it is mono-color. However, as will be detailed in the next sub-section, a pseudo color mapping can digitally generate lensfree color images.

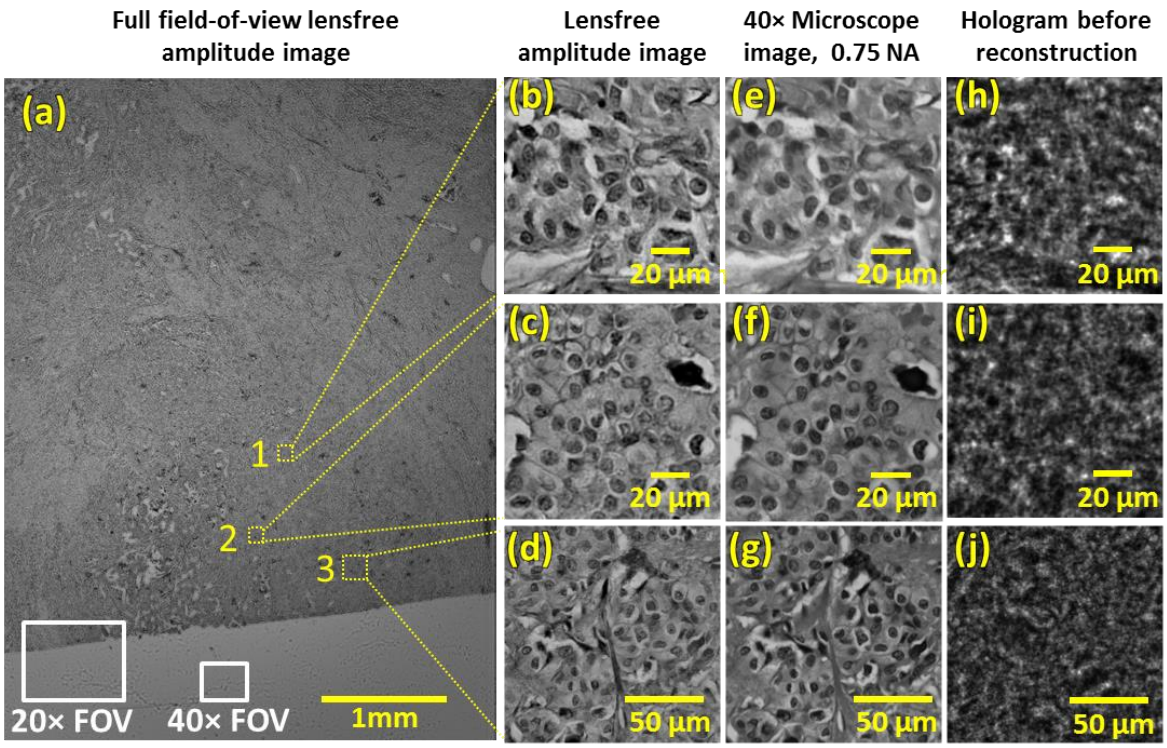


Figure 5.2 Lensfree imaging of invasive ductal carcinoma of the human breast. **(a)** A full FOV (20.5 mm^2) lensfree amplitude image of the specimen. The sample is ~ 7 µm thick and therefore it is rather challenging to image in transmission using traditional in-line holographic methods. For comparison, the fields-of-view of 40× and 20× microscope objectives are also shown using white solid rectangles. **(b)** to **(d)** Zoomed in regions of the lensfree image, which show a disorderly epithelial cell proliferation with cribriform growth. The cells exhibit nuclear enlargement, slightly irregular nuclear contours, open chromatin, and moderate delicate cytoplasm. **(e)** to **(g)** Microscope comparison images of (b) to (d) taken with a 40× objective lens (0.75 NA). **(h)** to **(j)** The super-resolved lensfree holograms before digitally reconstructed to yield the images shown in (b) to (d).

Pseudo colored lensfree imaging of invasive carcinoma cells within a human breast section: After establishing that lensfree on-chip microscopy provides high-quality clinical images of connected tissue samples over a large FOV, next we imaged a human carcinoma of breast section with a thickness of 4 µm (Fig. 5.3). Even though the raw lensfree image was captured using only one illumination wavelength, to digitally colorize the reconstructed image, a

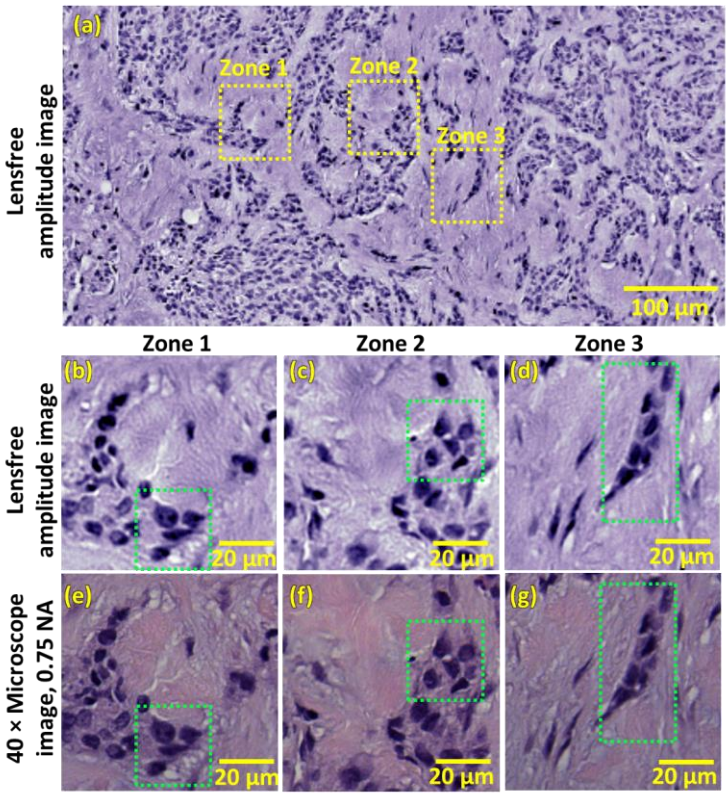


Figure 5.3 Lensfree pseudo color imaging of human carcinoma of the breast. **(a)** Lensfree amplitude image that shows invasive carcinoma cells arranged in irregular nests within the connective tissue. The image was captured using a single illumination wavelength (λ = 550 nm) and automatically colored using a transformation that maps intensity to color. **(b)** to **(d)** Zoomed in lensfree amplitude images of zones 1-3, respectively. The cells within the dashed green boxes are invasive carcinoma cells with increased nuclear to cytoplasmic ratios, hyperchromasia, irregular nuclear contours, and scant cytoplasm. **(e)** to **(g)** Microscope comparison images of (b) to (d) taken with a 40× objective lens (0.75 NA).

transformation that maps intensity to color through prior learning statistics was used (see Section 5.4). Fig. 5.3(a) illustrates this pseudo colored lensfree image of carcinoma cells invading a connective tissue region. The cells are arranged in irregular nests within the connective tissue, as illustrated with the green dashed rectangles in Figs. 5.3(b) to (d). Each nest contains cells that exhibit increased nuclear to cytoplasmic ratios, hyperchromasia, irregular nuclear contours, and

scant cytoplasm. All these observations are made by a pathologist examining our lensfree reconstructed color image shown in Fig. 5.3.

Lensfree color imaging of a Papanicolaou smear, consistent with a high-grade squamous intraepithelial lesion: Cervical cancer screening is another medical application that requires high-throughput and cost-effective imaging solutions. The pathologist or cytotechnologist is required to mechanically scan (using a light microscope) large area Pap smear samples, in search for pre-cancerous cells, which is a tedious, but imperative task. The large FOV of lensfree imaging could assist the pathologist to minimize the mechanical scanning, as its FOV covers substantial area within the entire smear (see Fig. 5.4(a)). Moreover, when a suspicious cell is detected, the pathologist typically refocuses the objective lens to different depth slices within the suspicious cell, to better assess the cell's morphology before classifying the cell. Lensfree holographic imaging can address this need since it possesses the ability to digitally focus the sample image to different depths after the image capture. Fig. 5.4 shows our imaging results for a normal Pap smear (Figs. 5.4(b) and (c)) and their microscope comparison images (Figs. 5.4(d) and (e)), as well as two different types of abnormal Pap smears that were confirmed by a pathologist using the lensfree images shown in Fig. 5.4(f) to (i) (ThinPrep® preparation)[119]. In Fig. 5.4(f), white arrows mark a cluster of squamous epithelial cells with nuclear crowding, increased nuclear to cytoplasmic ratios, and slightly irregular nuclear contours. In Fig. 5.4(g) to (i), the white arrows mark the cells that show high nuclear to cytoplasmic ratios, irregular nuclear contours, hyperchromasia, and scant cytoplasm. These findings, enabled by our lensfree on-chip microscope images, are consistent with a high-grade squamous intraepithelial lesion.

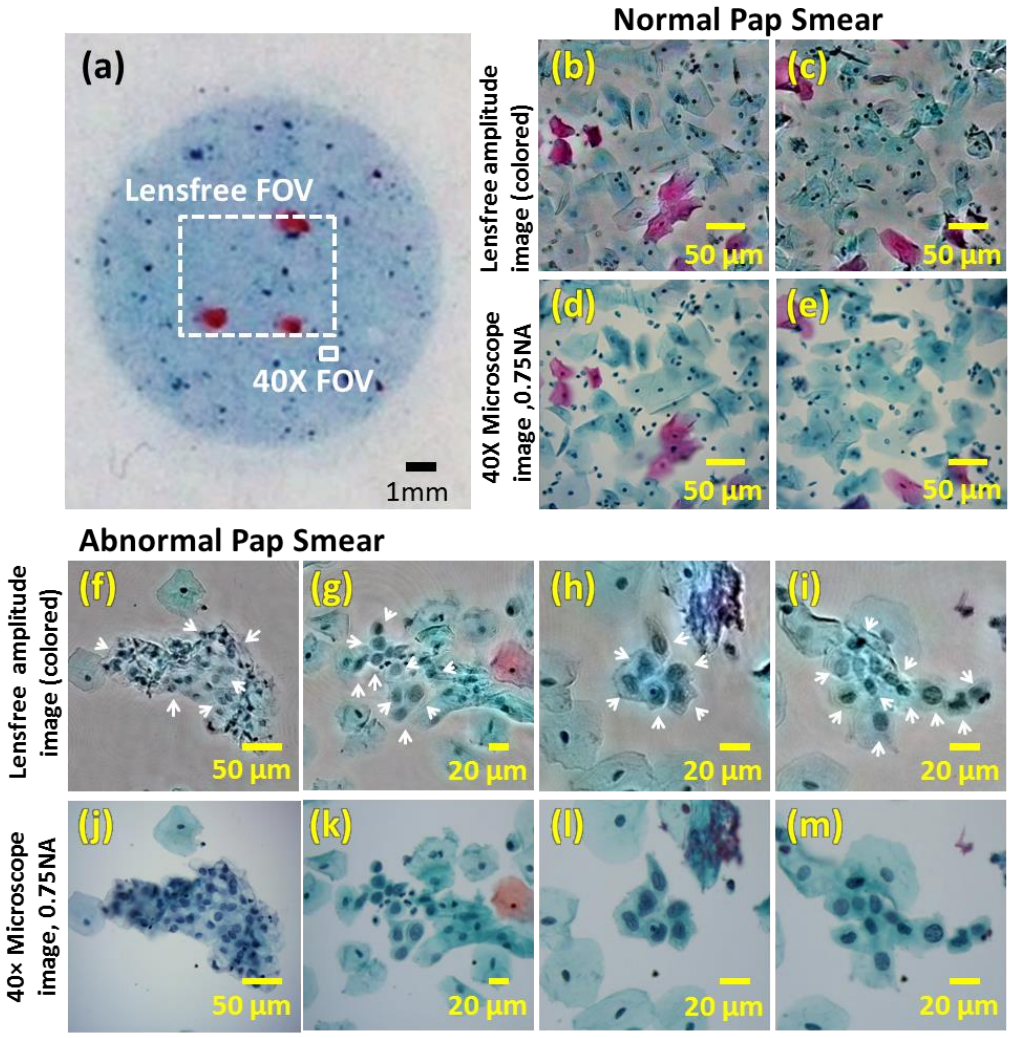


Figure 5.4 Lensfree color imaging of normal and abnormal Papanicolaou (Pap) smears. **(a)** A photograph of a normal Pap smear slide (SurePath™ preparation). For comparison, the FOV of our lensfree microscope and of a bright field microscope equipped with a 40× objective lens are marked by a dashed and a solid rectangle, respectively. **(b)** and **(c)** Lensfree images of a normal Pap smear taken from the smear in (a), and their microscope comparison images **(d)** and **(e)** taken with a 40× 0.75 NA objective lens. **(f)** A lensfree color image of atypical squamous cells. The white arrows mark a cluster of squamous epithelial cells with nuclear crowding, increased nuclear to cytoplasmic ratios, and slightly irregular nuclear contours. **(g)** to **(i)** Lensfree color images that show cells with high nuclear to cytoplasmic ratios, markedly irregular nuclear contours, hyperchromasia, and scant cytoplasm (white arrows). These findings are consistent with a high grade squamous intraepithelial lesion. **(j)** to **(m)** Microscope comparison images of (f) to (i) taken with a 40× objective lens (0.75 NA).

The colorization method used to generate these results is based on YUV color space averaging as detailed in section 5.4.

Lensfree imaging of whole blood smears: Blood smear is still considered as one of the standard methods to identify immature or abnormal cells that are indicative of various diseases such as anemia, hemoglobin variants and bone marrow disorders[120]. Using our lensfree on-chip microscopy platform we also imaged normal and abnormal blood smears as illustrated in Fig. 5.5. Figs. 5.5(a) to (d) show recorded holograms before reconstruction. However random these lensfree holograms may seem, our reconstruction technique is able to transform these holograms to valuable images (Figs. 5.5(e) to (h)) that match very well with lens-based microscope comparison images shown in Figs. 5.5(i) to (l). In a normal smear (Figs. 5.5(e) and (f)), mature red blood cells have uniform diameters of ~7 μm, they are shaped as a donut (round with an indentation in the middle) and do not have a nucleus. In an abnormal smear taken from a patient with a sickle cell anemia, however, the red blood cells' morphology is clearly different (Figs. 5.5(g) and (h)). Sickle red blood cells (yellow arrows) and target cells (red arrows) are observed in Figs. 5.5(g) and (h). The lensfree microscope resolution also enables the identification and classification of white blood cells that are present in the blood smear (see Figs. 5.5(e) and (f)).

5.3 Discussion

Our results demonstrate that lensfree holographic on-chip imaging provides wide FOV 3D images with high-resolution and fidelity that are sufficient for pathology applications. The wide FOV that is digitally recorded in lensfree on-chip microscopy not only provides two orders of magnitude improvement in throughput compared to a lens-based microscope of similar resolution level, but also enables digital focusing of the image plane to different depth sections, a highly desired attribute that is especially important to give the pathologists more degrees of

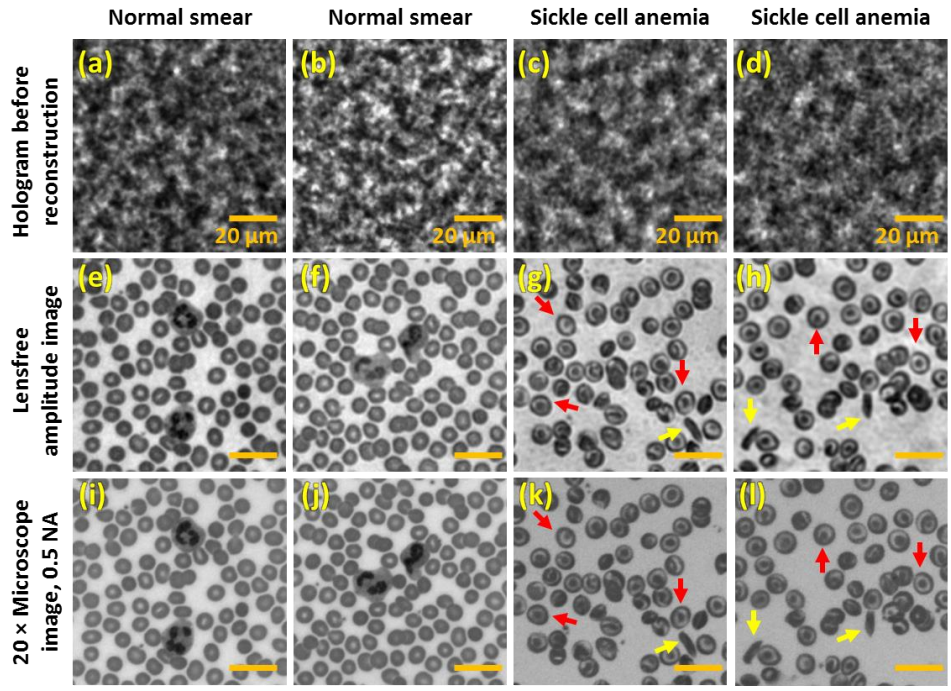


Figure 5.5. Lensfree imaging of normal and sickle cell anemia blood smears. **(a)** to **(d)** Super-resolved lensfree holograms before reconstruction. **(e)** to **(h)** Lensfree amplitude images that are reconstructed from the holograms shown in (a) to (d). The images in (e) and (f) show two normal white blood cells in each image and multiple normal red blood cells. In contrast, the red blood cells imaged in (g) and (h) show very different morphology. The yellow arrows mark abnormal (sickle) red blood cells, while the red arrows mark target cells (exhibiting a bullseye appearance), which are typical for hemoglobinopathy disease. **(i)** to **(l)** 20× objective lens (0.5 NA) microscope comparison images of (e) to (h) respectively. All scale bars are 20 µm.

freedom in their examination of the samples since often times different parts of the specimen appear in focus at different depths for large area pathology samples. Some examples of this 3D focusing capability are illustrated in Fig. 5.6. This 3D imaging performance cannot be achieved using other on-chip microscopes that are based on contact imaging since complex optical fields cannot be retrieved using a contact imaging geometry, which strictly demands the objects to be flat and parallel (with sub-micron gap) with respect to the plane of the sensor chip. In reality, however, pathology samples and other medically relevant biological specimens naturally have

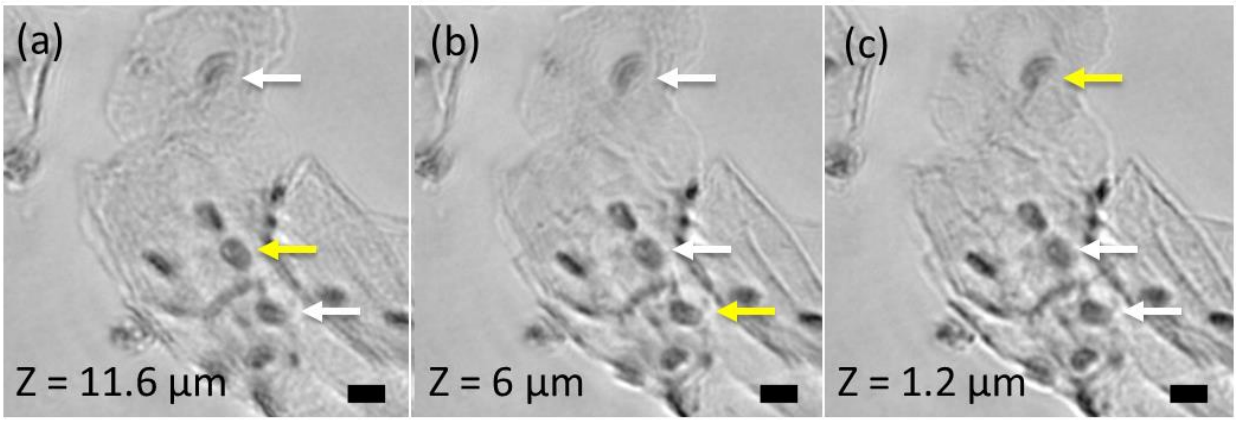


Figure 5.6 A demonstration of digital focusing, an inherent property of lensfree on-chip imaging. **(a)** to **(c)** Lensfree images of cells on a Pap smear sample that were digitally focused to different depths. At each depth, the yellow arrow marks an in-focus nucleus, while the white arrows mark out-of-focus nuclei. Scale bars are 10 µm.

3D features, with uncontrolled modulation of the gap between the sample and sensor planes, both of which create spatial artifacts in contact or shadow imaging. On the other hand, since holographic on-chip microscopy retrieves complex optical fields of the objects, 3D nature of specimen and uncontrolled variations in tilt and height of the specimen can be digitally corrected.

In our reconstruction process to retrieve complex optical fields of dense specimen, the convergence of our iterations depends on the quality of the initial phase guess. Rather than selecting a random initial phase guess (which has been the standard practice in earlier work [24,40,110,121,122]), in this work we digitally solve TIE, which provides an analytical solution[82,83,123] to the phase of an optical wave from a series of defocused intensity images (see section 5.4). Note that we only use the TIE solution for the *initial* phase guess to our iterative multi-height phase retrieval algorithm, and therefore our images are not affected by the low-resolution Fresnel approximation that is inherent to TIE. Although for relatively sparse and less connected objects TIE solution might not always be needed, for dense and connected objects such as histopathology slides it provides significant convergence advantages. By comparing the

reconstructed amplitude images with and without TIE, Figs. 5.7(a) and (b), respectively, we can clearly see that the use of TIE is very important since either less number of iterations or less number of heights can be used to reconstruct the lensfree image using TIE solution as the initial phase guess. This in turn reduces the computational burden of lensfree imaging without degrading the spatial resolution of the image. To validate that our spatial resolution is not

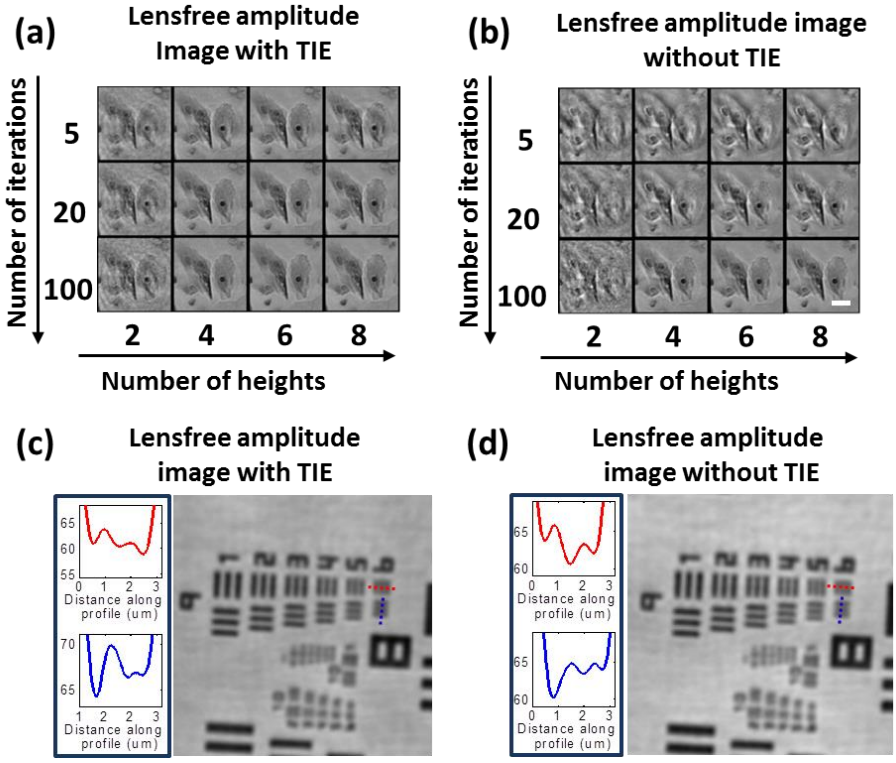


Figure 5.7. The effect of using TIE solution on multi-height phase recovery algorithm convergence and spatial resolution. (**a)** and (**b**) Reconstructed lensfree amplitude images as a function of the number of heights and the number of iterations. In (a) the solution of TIE was used as an initial phase guess for the multi-height phase-recovery algorithm. This educated initial phase guess drastically accelerates the convergence in comparison to (b), where a random phase was used as an initial phase guess to the multi-height phase recovery algorithm. Scale bar is 20 µm. (**c)** and (**d**) Resolution quantification using extreme USAF test chart with and without TIE solution as an initial phase guess for the multi-height phase recovery algorithm, respectively. With a green illumination wavelength (λ = 532 nm), gratings with a line-width of 548 nm (group 9, element 6) are resolved in both cases.

compromised using TIE initial phase, we imaged extreme-USAF test chart (Ready Optics, item# 2012B), where the last element of group 9, which corresponds to a grating line-width of 548 nm, was successfully resolved using $\lambda = 532$ nm (see Figs. 5.7(c) and (d)).

In addition to its wide FOV and 3D imaging capability, one other advantage of lensfree on-chip imaging is its cost-effectiveness and design simplicity compared to a lens-based pathology microscope. In the current setup, we utilized a mechanical positioning stage mainly for two reasons. First, the positioner is used to laterally shift the sample for implementing pixel-super resolution; this function of the stage can be replaced by source shifting using e.g., an array of laser diodes or light-emitting-diodes (LEDs), which is a cost-effective solution for achieving pixel super-resolution as our group reported earlier[7,24,124]. Furthermore, in our reconstructions, as detailed in our section 5.4, we utilize an algorithm to automatically determine the relative sub-pixel shifts of each lensfree hologram, *without* the need for a measurement or reading from the scanning system; therefore even a simple and inexpensive mechanical stage would work fine for implementing pixel super-resolution. Second, the mechanical stage is used to modulate and control the sample-to-sensor distance, so that we can capture several defocused interference patterns for our multi-height phase recovery algorithm. However, for this purpose, a simple and inaccurate *one-axis* translation stage is sufficient since we digitally estimate the sample to sensor distance as well as uncontrolled tilts of the sample using an autofocus algorithm with ~1 μm precision, *without* the need for stage readings (see section 5.4). In fact, we modified our multi-height phase recovery algorithm to digitally compensate for these uncontrolled tilts and variations in sample to sensor distances along our FOV, which permits the use of a low-cost 1D translation stage (see Fig. 5.8). Fig. 5.8(a) depicts the challenge of using a low-end axial translation stage, e.g., with a cost of ~$10-20: each recorded hologram at a given height exhibits

a different tilt between the axially translated sensor-chip and the sample plane. These uncontrolled tilts result in distortions that are apparent in the reconstructed images as can be seen in Figs. 5.8(d) to (g). To digitally mitigate these distortions (after image capture), we utilize a *rotational field transformation* technique (see Section 5.4), which is a computational method that can reconstruct a complex image on any arbitrarily tilted plane[71,125–127]. Fig. 5.8(b) depicts the inclusion of this rotational transformation in our multi-height phase-recovery algorithm, where the current guess of each iteration (blue dashed rectangle) is projected onto the image sensor plane (green solid rectangle) to enforce the measured intensity, while retaining the phase. This tilt correction step in the forward model of our algorithm is of paramount importance in order to reconstruct the phase of the optical wave. To test the robustness of this algorithm, we recorded five interference patterns using five highly tilted planes, mimicking a poorly designed experimental setup that is even worse than the performance of a typical inexpensive 1D translation stage. A graph that shows the sample-to-sensor distances for these five heights can be seen in Fig. 5.8(c). Without the tilt correction, the reconstructed images are severely distorted (see Figs. 5.8(d) to (g)), in contrast with the lensfree images shown in Figs. 5.8(h) to (k), which used the tilt correction process as detailed in Fig. 5.8(b). Therefore, this computational tilt correction and sample height estimation approach enables cost-effective implementations of lensfree on-chip microscopy, digitally eliminating the need for expensive scanning hardware.

All the pathology slides reported in this work that are reconstructed in 3D were processed using 288 raw lensfree images (36 holograms per height to perform pixel super-resolution, and 8 heights to perform multi-height phase recovery), which translate into image acquisition times that are on the order of several seconds using the maximum frame rate of our opto-electronic

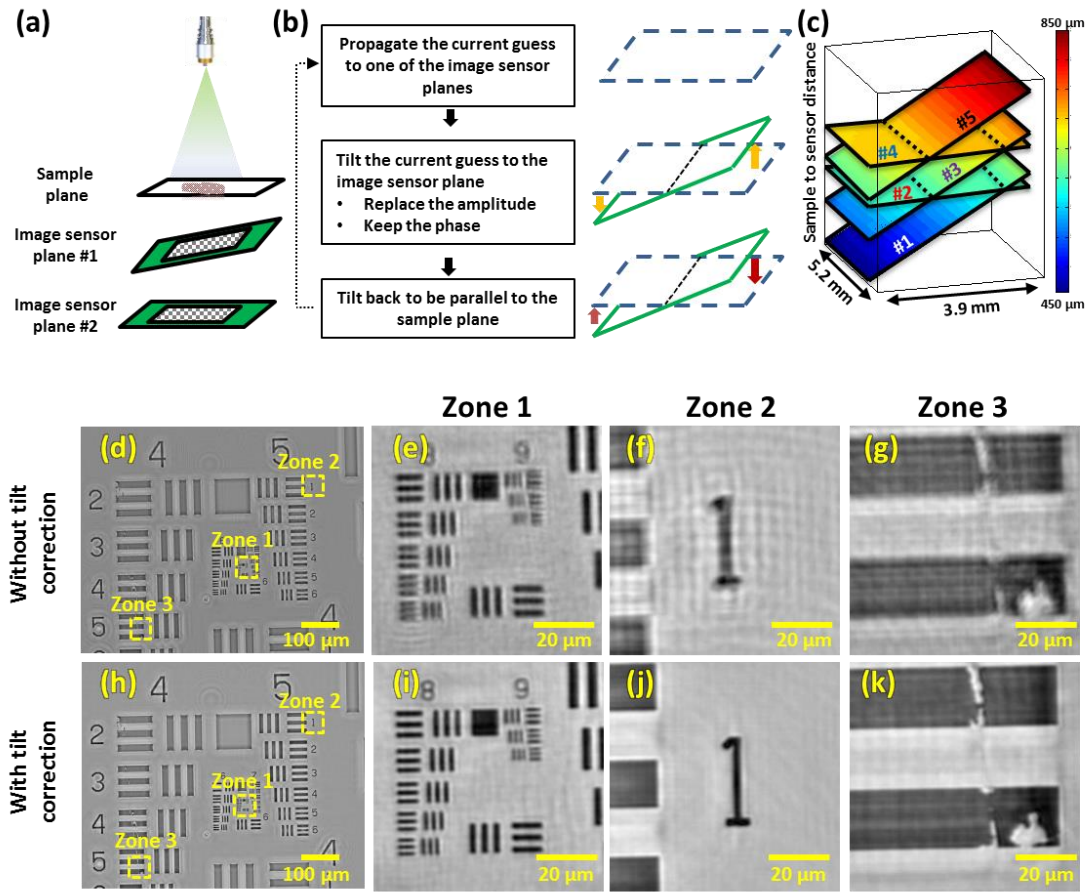


Figure 5.8. Computational tilt correction in multi-height phase-recovery algorithm. **(a)** When using a low-end stage to mechanically modulate the sample-to-sensor distance, mechanical tilts between the sample and the image sensor planes might occur as illustrated in this schematic. **(b)** A modification of the multi-height phase-recovery algorithm is shown, which corrects for such mechanical tilts between the sample and the image sensor planes. **(c)** A graph that shows the sample-to-sensor distances at five different heights, when the tilt angle between the planes alternated between 3.5˚ to 0.2˚. This experiment represents a poorly aligned lensfree imaging setup and these tilted measurements are used to reconstruct images shown in (d) to (k). (**d**) A lensfree amplitude image that was reconstructed *without* using tilt correction. **(e)** to **(g)** Zoomed in images of zones 1-3 in (d) respectively. Spatial aberrations caused by the physical tilts among planes are apparent. **(h)** A lensfree amplitude image that was reconstructed by compensating for these tilts during the multi-height phase recovery algorithm as proposed in (b). **(i)** to **(k)** Zoomed in images of zones 1-3 in (h), respectively. These reconstructed lensfree images, due to our digital tilt correction, do not exhibit the aberrations that were observed in images (e) to (g).

image sensor chip (15 frames per second). This image acquisition time can be significantly improved using faster CMOS imager chips and/or pulsing of illumination source(s); however, for pathology applications, our current image acquisition times do not form a limiting factor since the pathology slides are fixed. In terms of the image reconstruction time, using MATLAB® and eight measurement heights, the entire processing time of a 1 mm × 1 mm sub-FOV took about nine minutes (~539 seconds) using a single desktop computer (Dell T3600, 16GB RAM memory and Intel Xeon processor E5-1620). Since all the reconstruction steps can be processed in parallel for different sub-FOVs, using a cluster of 20 nodes (e.g., quad-core machines), the entire FOV reconstruction can be performed within 10 minutes. This processing time can be further improved by using: (*i*) a cluster of Graphics Processing Units (GPUs) instead of Central Processing Units (CPUs), such that the total reconstruction time can be improved by an additional factor of 10-20 fold as our algorithms heavily rely on fast Fourier transforms[25]; and (*ii*) optimized algorithms running on more efficient software languages such as C/C++. Therefore, even with a single desktop computer using GPUs, the processing time for full FOV reconstructions can be reduced to less than a few minutes.

Another important topic of interest that needs to be discussed is the coherence of illumination, both spatially and temporally. For contact on-chip microscopy, since the ideal gap between the sample and sensor planes is sub-micron, one can initially assume that the coherence of the source is of secondary importance. However, coherence properties of the source still introduce spatial artifacts in contact imaging due to optical diffraction that occurs between the sample and sensor planes. This unavoidable artifact is especially more pronounced for non-planar objects and sub-micron features of the specimen, imaged using contact on-chip microscopy[70]. On the other hand, for lensfree holographic on-chip microscopy, partial coherence of the source is *engineered* and

utilized in our favor to retrieve high resolution complex fields of the specimen to digitally reverse optical diffraction so that the vertical gap between the sample and sensor planes can be significantly larger compared to contact imaging, and it can also spatially vary within the sample FOV, without introducing spatial artifacts. For this performance, we engineered our spatial coherence diameter at the sensor plane to be > 4 mm and temporal coherence length to be ~0.1 mm[128], permitting high-resolution imaging of connected tissue slides over >20 mm^2 FOV with significantly reduced speckle and multiple reflection interference noise terms.

This 3D imaging capability using lensfree on-chip imaging is a landmark result for automated digital imaging of pathology slides even in resource limited clinical settings, where e.g., the patient-to-doctor ratio is much larger than 1,000. It not only creates a cost-effective telemedicine tool by enabling the medical professionals to remotely seek for a second opinion, but can also provide the diagnosing pathologist a documentation tool, which could protect the pathologist in the case of medical malpractice lawsuit, or to serve as a training resource[129] for prospect pathologists.

5.4 Theory and methods

Analytical phase retrieval using the transport of intensity equation (TIE):TIE [40,82,83,123] is an elliptic partial differential equation that relates the phase of an optical field to the z-derivative of the field intensity. Unlike iterative methods, this equation deterministically computes the phase. The TIE performance is typically limited by the low-numerical-aperture assumption, imperfect knowledge of axial derivative of intensity, relatively high susceptibility to noise, and the need for the knowledge of the phase at the perimeter of the aperture, which is usually not available[83,123]. However, the TIE phase solution is a good initial guess to the multi-height phase recovery algorithm that can accelerate convergence. In our work, the intensity derivative along

the axial direction is approximated by the differentiation of intensity measurements at two different heights divided by the distance between them. The first height is picked as the lowest one, and the second height is picked among the other heights so that they are separated by approximately 100 μm with respect to each other. The elliptic equation is solved using a finite element method based elliptic equation solver[130]. Due to the fact that the phase at the boundary is difficult to measure in practice, we taper the intensity derivative gradually to zero at the edges using a Tukey window and assume a zero Dirichlet boundary condition at the edges of the aperture. The output of the equation solver is fed to the multi-height phase retrieval algorithm as the initial guess for the optical phase. To increase the speed of the TIE solver, a faster solution to the TIE can also be generated using a fast Fourier transform based approach, but it is in theory less accurate than the elliptic equation solver due to its periodic assumption of the boundary conditions[40,131]. Note, however, that this fast Fourier transform based method does not introduce any visible degradation of the reconstructed image quality compared to elliptic equation solver.

Colorization of lensfree holographic images: In biomedical imaging, color is of great importance and color staining of samples is widely used. One method for coloring of lensfree holographic images involves capturing and reconstructing images at three wavelengths (i.e., red, green and blue) and using them as the RGB channels, respectively, to create a color image. However, this scheme triples the image acquisition and processing time compared to the mono-color case, and also gives rise to a spatial color noise, commonly referred to as the "rainbow" artifact in holographic imaging. An alternative solution that we utilized in this work involves spatial-averaging of only the color information of an image in the YUV color space to alleviate this rainbow artifact[55,124]. The YUV color space[114] has three channels Y, U and V, where Y represents the luminance (brightness), and U an V represent the chrominance (color). This YUV

representation can be created from RGB color space via a simple linear transform. By taking advantage of the separation of the color from the brightness channel in the YUV color space, the rainbow artifact can be mitigated by moving-averaging (or equivalently, low-pass filtering) in the U and V channels without affecting the brightness of the image. In this manuscript (e.g., Fig. 5.4), we synthesized the color (U and V) channels from back-propagated low-resolution holograms acquired at three wavelengths (blue: 471 nm, green: 532 nm, red: 633 nm) by RGB to YUV conversion; we then used the high-resolution multi-height reconstructed image, acquired at only one wavelength (green, 532 nm) as the Y channel. Next the U and V channels are low-passed filtered spatially with a rectangular window. Finally, the YUV image is converted back to the RGB domain. This process is computationally very efficient as only one high-resolution (i.e., super-resolved) image needs to be reconstructed (at the green wavelength), hence the total reconstruction time is only ~5% longer than that of the mono-color case.

In order to further reduce the computational complexity and relieve the need to capture multi-color holograms, we also implemented a second colorization method based on a single mono-color reconstructed image (see Fig. 5.3). In this method, a digital mapping function between luminance (Y) and color (U and V) channels is created by statistically learning the transformation that exists in a given stain type of interest. In the initial learning phase, traditional microscope images of the specimens are converted into the YUV color space[74,114], where a pixel-by-pixel scan relates each Y value to its corresponding average U and V values, resulting in a statistical mapping function. Next, this learned mapping is applied to digitally color the single wavelength lensfree reconstructed images of the same stain type, deciding on the missing color values (U and V) of each pixel according to the reconstructed holographic image intensity, which serves as the brightness (Y) channel of the final colored image. The full YUV representation is

finally converted to the RGB color space to yield the lensfree color image. In this method, since all the holograms are captured at a single wavelength, the image acquisition time is equal to the mono-color case and there is no need for a multi-wavelength experiment. The initial learning step needs to be carried out only once for a specific stain-tissue combination, and therefore new samples of the same type can be rapidly colored using the same mapping function. Also note that in order for the color mapping to be applied correctly, the range of amplitudes (or intensity values) of the lensfree image needs to be digitally matched to the acquired microscope images, i.e., histogram matching, to increase the coloring similarity between the lensfree and lens-based microscope images, which needs to be performed only once for a given lensfree imaging setup.

Field transformations among tilted planes: Rotational transformation of a complex optical field is a computational method that enables the reconstruction of an image on arbitrary tilted planes using the phase information of an optical wave[71,125–127]. For example, when trying to image a tilted surface using a bright field microscope, the microscope user has to constantly refocus the microscope at different locations within the FOV; however, if one has access to the complex field information, the entire sample can be digitally focused all at once using rotational transformations. This method is computationally inexpensive as it involves two fast Fourier transforms and a single interpolation step in the Fourier domain. To implement it, and to digitally focus the entire FOV of our lensfree on-chip microscope, the local tilt angles between the image sensor and the sample need to be determined. We automatically estimate these local tilt angles by utilizing the autofocus algorithm at different spatial locations on the sample's FOV, and find their absolute heights. We can then fit a local plane to match these heights (see e.g. Fig. 5.8(c)), and find a 3D rotation transformation matrix (T) .T is a 3×3 matrix:

$$T = \begin{bmatrix} a_1 & a_4 & a_7 \\ a_2 & a_5 & a_8 \\ a_3 & a_6 & a_9 \end{bmatrix} \qquad (5.1)$$

that transforms between two coordinate systems (Fig. 5.9): the source/image sensor coordinate system (x, y, z), with a position vector $\boldsymbol{r} = (x, y, z)$ and the reference/sample coordinate system $(\hat{x}, \hat{y}, \hat{z})$, with a position vector $\hat{\boldsymbol{r}} = (\hat{x}, \hat{y}, \hat{z})$. These two position vectors can be mutually transformed using:

$$\hat{\boldsymbol{r}} = T\boldsymbol{r}. \qquad (5.2)$$

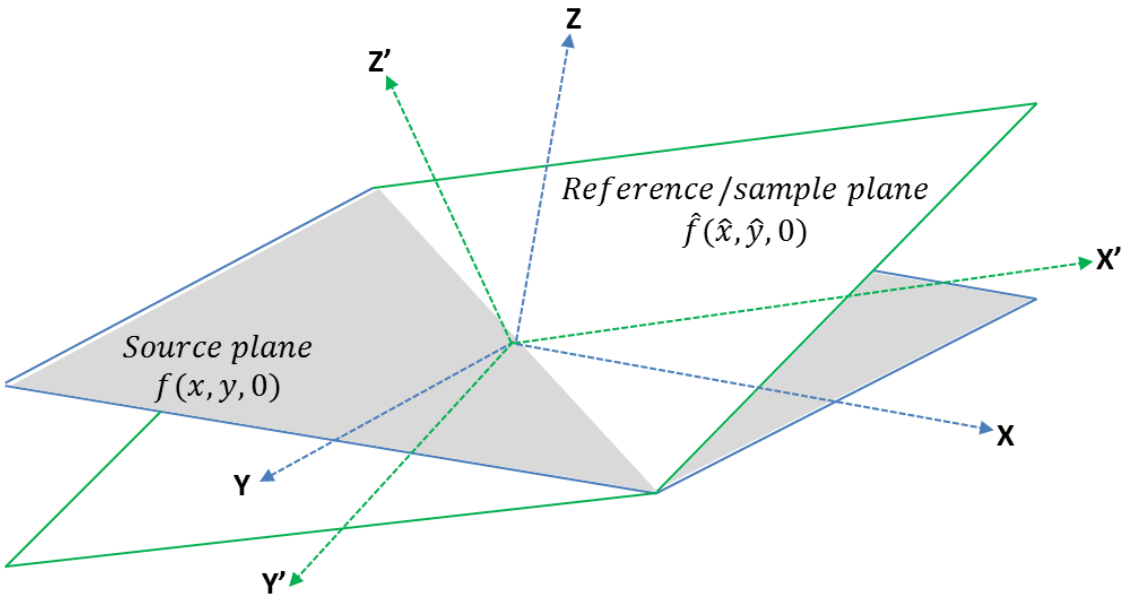


Figure 5.9 The definition of two coordinate systems: the source plane is parallel to the image sensor, while the reference/sample plane is tilted.

Initially a wave field is obtained in the source plane $f(x, y, 0)$, and the projection on a sample plane is desired $\hat{f}(\hat{x}, \hat{y}, 0)$. The Fourier transform pairs for these two planes are defined as:

$$f(x, y, 0) = F^{-1}\{F(u, v)\}; \hat{f}(\hat{x}, \hat{y}, 0) = F^{-1}\{\hat{F}(\hat{u}, \hat{v})\}, \qquad (5.3)$$

where u, v and $\hat{u}, \hat{v}$ are the spatial frequencies for the source and reference planes. Given these relations it has been previously shown[127], that $\hat{F}(\hat{u}, \hat{v})$ can be obtained using:

$$\hat{F}(\hat{u},\hat{v}) = F\big(a_1\hat{u} + a_2\hat{v} + a_3\hat{w}(\hat{u},\hat{v}), a_4\hat{u} + a_5\hat{v} + a_6\hat{w}(\hat{u},\hat{v})\big)|J(\hat{u},\hat{v})|, \quad (5.4)$$

where $\hat{w}(\hat{u},\hat{v})$ is defined as:

$$\hat{w}(\hat{u},\hat{v}) = \sqrt{\lambda^{-2} - \hat{u}^2 - \hat{v}^2} \quad (5.5)$$

and $J(\hat{u},\hat{v})$ is the Jacobian of the coordinate transformation T, which is defined in equation (5.6).

$$J(\hat{u},\hat{v}) = \frac{(a_2a_6 - a_3a_5)\hat{u}}{\hat{w}(\hat{u},\hat{v})} + \frac{(a_3a_4 - a_1a_6)\hat{v}}{\hat{w}(\hat{u},\hat{v})} + (a_1a_5 - a_2a_4). \quad (5.6)$$

Close examination of equation (5.4) reveals that an interpolation in the frequency domain is required to solve for $\hat{F}(\hat{u},\hat{v})$ as the frequencies are discretized on an equidistance grid. For accurate results[132] the interpolation methods that was chosen is "Cubic 8" and it was implemented in C to minimize the processing time.

Multi-height phase recovery with tilt correction: To take into account the tilts between the image-sensor and the sample planes we modified the multi-height phase recovery algorithm. First, the tilt angles between different planes are evaluated using our autofocus algorithm (see section 3.4). Second, the multi-height phase recovery process is evoked without tilt correction for ten iterations. The result of this previous step serves as an initial guess for the modified multi-height algorithm. In this modified algorithm (Fig. 5.8(b)), the current guess is still propagated among different measured planes, however, after the propagation step the current guess (blue dashed rectangle) is projected to the tilted image-sensor plane (green solid rectangle) using the rotational transformation discussed earlier. The tilted current guess is then registered to the measured hologram. After the registration step, the tilted current guess amplitude is averaged with the measured amplitude, while the phase of the current guess is maintained for the next cycle of iterations. After this step, the current guess is rotated back to a parallel plane (blue dashed rectangle) and it is digitally propagated to the next measured plane/height until convergence is achieved, which usually takes 10-20 iterations.

Chapter 6 Field-portable pixel super-resolution color microscope

In this chapter I report a field-portable lensfree microscope that can render color images over a wide field-of-view of e.g., >20 mm^2. This computational holographic microscope weighs less than 145 grams with dimensions smaller than 17 × 6 × 5 cm, making it especially suitable for field settings and point-of-care use. Parts of this chapter have been published in Greenbaum, A., Akbari, N., Feizi, A., Luo, W. & Ozcan, A. Field-portable pixel super-resolution colour microscope. *PLoS ONE* **8,** e76475 (2013).

6.1 Introduction

In recent years there has been a large interest in point of care (POC) imaging and sensing devices that could permit remote clinics or doctors' offices to conduct basic diagnostic tests that are traditionally restricted to hospitals, requiring a relatively large capital investment[133–142]. Recent progress in this direction created various field-portable and cost-effective designs that have the capacity to perform e.g., flow-cytometry[143], optical coherence tomography[144,145], water quality monitoring[62], fluorescent imaging[146–148], and other imaging/sensing tasks[16,149] even in resource limited settings.

Lensfree holographic on-chip microscopes form an emerging sub-group of such POC imaging devices, and of digital holography in general[5,150,151], offering competitive alternatives to conventional lens-based microscopes, with several key advantages such as wide FOV and large depth-of-field, yielding giga-pixel range phase and amplitude images, in addition to compactness and cost-effectiveness, making them especially appealing for global health related applications[103–105]. Here we present a lensfree super-resolution color microscope design, which is cost-effective and field-portable, weighing < 145 grams with dimensions of < 17 × 6 × 5 cm (see

Fig. 6.1). In this field-portable color microscope, we introduce an image processing technique that mitigates 'rainbow' like color artefacts. This colorization technique is based on transforming the lensfree RGB image into the YUV color space[106,114], which separates the brightness component of the image (i.e., Y channel) from its color components (i.e., U and V channels). As a result of this, to achieve sub-micron spatial resolution in color, there is no need to capture three distinct pixel super-resolved holograms, each with a different illumination color (i.e., red, green and blue). In fact, it is sufficient to acquire only one pixel super-resolved lensfree image with a single illumination wavelength (e.g., green) which can serve as the Y channel of the color image, preserving the sub-micron resolution over a large FOV. To obtain the remaining U and V channels of the color image, since there is no need for pixel super-resolution, three LEDs at red, green and blue wavelengths would be sufficient. To demonstrate the resolution and color imaging capabilities of this field-portable holographic microscope, we imaged a USAF resolution test chart and color stained Pap smears, which are widely used for pre-screening of cervical cancer[113].

In the previous chapters, I also introduced a lensfree color microscopy concept, which uses similar image processing methods to mitigate 'rainbow' like color artefacts. However, this previous work was performed on a bench-top system within a well-controlled environment, which involved an optical table as well as a mechanical micro-stage and a monochromator to control the illumination position and the wavelength. In this chapter I introduce a novel design and the experimental implementation of a field-portable, light-weight and cost-effective color microscope, which is based on inexpensive components such as an array of LEDs and 3D printed plastic enclosure. This field-portable, cost-effective and wide-field color microscope could be

significant especially for tele-pathology and micro-biology applications in resource limited environments and developing countries.

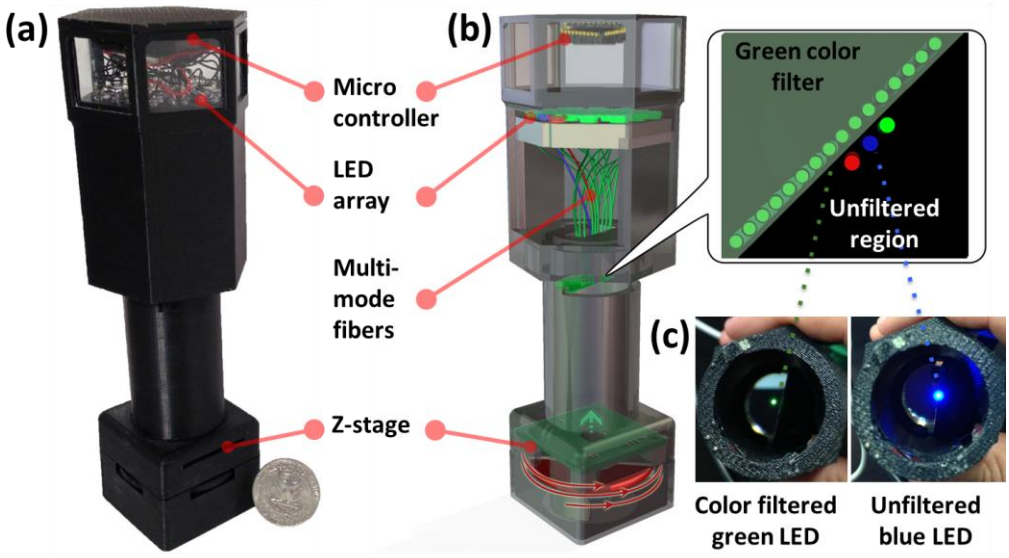


Figure 6.1 A portable lensfree super-resolution color microscope. **(a)** A photograph of the microscope that weighs < 145 grams. **(b)** A schematic diagram of the microscope; the LED array is separated into two groups, the first group enables pixel super-resolution based on source shifting, and it contains 17 green LEDs (λ = 527 nm) where each LED is butt-coupled to a multi-mode fiber and its emission passes through a color filter as shown in the inset. The second group of LEDs enables the acquisition of a lower resolution color image and it is composed of three LEDs (λ = 470 nm, 527 nm and 625 nm). **(c)** A photograph of one of the 17 green LEDs (left) and the blue unfiltered LED (right).

6.2 The design of a field-portable color lensfree microscope

Our field-portable microscope (see Fig. 6.1) is designed to enable both pixel super-resolution and color imaging by separating a set of low-cost LEDs that serve as the illumination source into two groups. The first group of LEDs enables pixel super-resolution imaging based on a shift of the source location; it contains 17 green LEDs that are butt-coupled to multi-mode fibers (each with 0.1 mm core diameter, Thorlabs, AFS-105/125Y). The emission of these green LEDs is also

passed through a color filter after each fiber end (bandwidth ~ 3 nm, centered around 532 nm, Thorlabs, FL532-3) to achieve the temporal coherence that is required for capturing high NA in-line holograms at the detector plane. To implement pixel-super resolution by source shifting, these green LEDs of the first group are arranged into a line, which is tilted 45 degrees relative to the image sensor edges (see Fig. 6.1(b)), such that the acquired lensfree holograms can be sub-pixel shifted along both X and Y directions.

The second group of LEDs enables the acquisition of lower resolution lensfree color images, and it is composed of only three LEDs: one blue, one green, and one red, with λ = 470 nm, 527 nm and 625 nm, respectively. The illumination bandwidth of each one of these LEDs is rather broad, e.g., ~ 45 nm, and since pixel super-resolution is not needed here, we did *not* employ a color filter for these second group of LEDs. Each LED is still butt-coupled to a multi-mode fiber (0.1 mm core diameter), as illustrated in Fig. 6.1(c).

All these 20 LEDs are individually controlled by a micro-controller (Atmel, ATmega8515), which sequentially turns on and off each LED within the array, while the image sensor captures lensfree holograms. The image capture and illumination are controlled in LabVIEW, and consequently the entire imaging process, including auto-exposure, is fully automated and is controlled using a laptop computer with a USB connection to the field-portable microscope.

The distance between the fibers' free ends (which are cleaved) and the object plane is designed to be ~ 6 cm for two reasons: first, to allow the partially-coherent illumination light to gain sufficient spatial coherence before impinging on the sample plane, and second to ensure that each LED will illuminate the sample with an angle that is less than three degrees compared to the surface normal. This restriction is of paramount importance for pixel-super resolution based

microscopy, since it enables capturing the same cross-section of the object in each sub-pixel shifted transmission image.

The above described multi-source illumination module is then connected to the sample holder and a cost-effective, custom-designed Z-stage (see Fig. 6.1(b)). This Z-stage has a coarse axial resolution of ~ 10-15 μm, and it is used to move the CMOS sensor chip (1.67 μm pixel size, 10 mega-pixel, monochrome) up and down compared to the sample plane, which is required for achieving multi-height based phase-recovery. This multi-height phase-recovery process enables imaging of dense and connected samples, such as pathology slides, by iteratively eliminating the twin image noise, which is an artefact of in-line holography. This Z-stage is custom built from a lens-tube (Thorlabs, SM1L03) and a threading adapter (Thorlabs, SM1A10), which is glued to the field-portable microscope enclosure.

6.3 Results

To quantify the spatial resolution of our field-portable microscope as a function of the number of heights used in our multi-height phase-recovery process (see Chapter 3), a 1951 USAF resolution test chart was imaged. In our image reconstruction process, we followed the computational flowchart shown in Fig. 4.2. Fig. 6.2(a) shows the reconstructed amplitude image using only one height (Z = 694 μm), which clearly resolves a line-width of 0.87 μm using a CMOS imager chip that has a pixel size of 1.67 μm. Fig. 6.2(b), on the other hand, shows the reconstructed amplitude image using two different heights (694 μm and 922 μm), which resolves a line-width of 0.98 μm. It is clear that using two different heights, the twin image noise is suppressed in comparison to Fig. 6.2(a); however, the resolution is also slightly degraded due to possible errors in spatial registration of the two super-resolved holograms acquired at different heights. When using three heights (694 μm, 922 μm and 958 μm), no additional degradation in

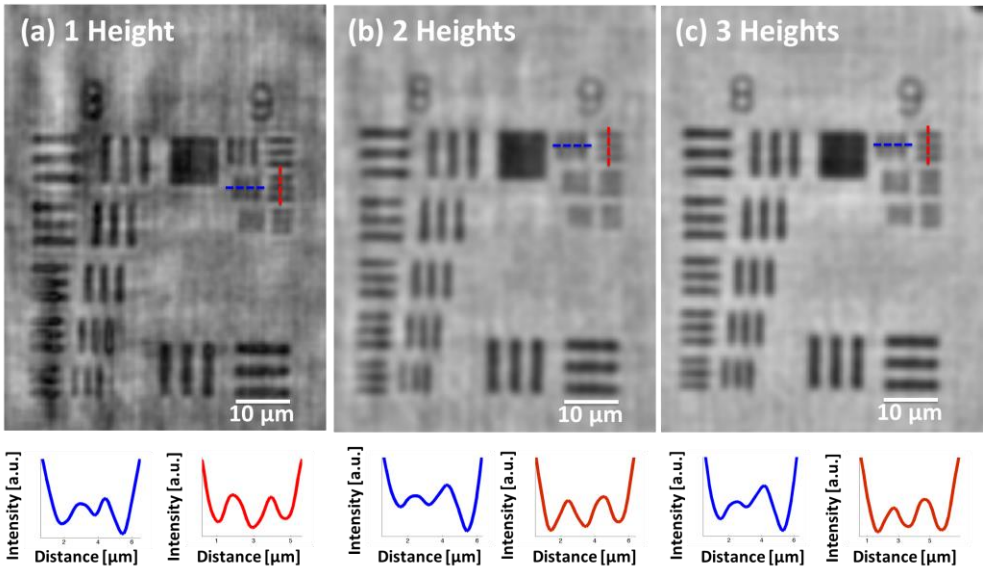


Figure 6.2 Quantification of the spatial resolution as a function of the number of heights used in our multi-height phase-recovery process. **(a)** Amplitude image that was reconstructed using one height. **(b)** Amplitude image that was reconstructed using two heights. **(c)** Amplitude image that was reconstructed using three heights. Cross sections of the smallest resolved gratings are provided below each reconstructed image. Pixel size of the monochrome CMOS chip used in our field-portable microscope is 1.67 µm. Note that using a CMOS imager chip that has a smaller pixel size (e.g., ~1.1 µm), a higher spatial resolution of e.g., ~300 nm can also be achieved using the same lensfree imaging technique[60,151].

resolution is observed as illustrated in Fig. 6.2(c); nevertheless the twin image noise is now significantly cleared (for instance, the dark vertical lines in Fig. 6.2(a) are not present in Fig. 6.2(c)). In these experiments, our goal was to illustrate this significant reduction of twin image related spatial artefacts, while also demonstrating that cross-registration of multi-height super-resolved holograms and their FOVs does not introduce a major resolution loss, still permitting sub-micron resolution as shown in Figs. 6.2(b) and 6.2(c).

To further illustrate the performance of our field-portable color microscope, next we imaged Pap smear samples over a wide FOV of ~ 21 mm^2, the results of which are summarized in Fig.

6.3. Pap test is a cytology-based method that is extensively used to diagnose cervical cancer, which is the second most common cancer in women worldwide[113]. Optical microscopy can be considered as one of the gold standard techniques for early detection of premalignant and/or malignant cells in a Pap smear, a task that is labor intensive and tedious, since in early stages of cervical cancer only a few cells among thousands of cells will statistically be abnormal. Moreover color is important in Pap tests since it allows differentiating between different states/types of cells on a Pap smear slide. To create the lensfree color images shown in Fig. 6.3, the computational flowchart of Fig. 4.2 was utilized; where pixel super-resolved holograms were synthesized at three/four different heights and five multi-height phase-recovery iterations were computed. Our reconstructed lensfree color images provide very good agreement with 20× microscope objective (0.5 NA) images, which are provided for comparison purposes. These results demonstrate the potential of this field-portable color microscope for tele-pathology and micro-biology applications, making it especially relevant for various global health applications.

6.4 Discussion

Since the low-resolution color image is overlaid on the high-resolution brightness image, it is evident that our microscope has a significantly better resolution in the brightness channel than in the color channel. Unlike the brightness channel, where the spatial resolution is determined by the effective pixel size of the image sensor after pixel super-resolution, e.g., ≤500 nm, the color resolution is determined by the size of the averaging window in the YUV color space (e.g., ~ 13 μm), which is used to mitigate the rainbow color artifacts in reconstructed holographic images. However, in the context of Pap tests or pathology in general, this resolution mismatch between the color (i.e., UV) and brightness (i.e., Y) channels is irrelevant. Sub-micrometer resolution is required in clinical pathology applications to observe the cells' boundaries and nuclei; this

information is provided in the brightness channel of our field-portable microscope. On the other hand, the color information is used as a visual marker to distinguish among different cell types; therefore lower color resolution requirements are acceptable. Moreover, the physical process of color staining creates an inherent resolution loss as the dye molecules diffuse inside the stained cell, creating smoothened boundaries. Consequently, the presented microscopic colorization scheme satisfies pathology needs, as it provides accurate color information that would have been normally concealed by the rainbow artifacts of holographic imaging.

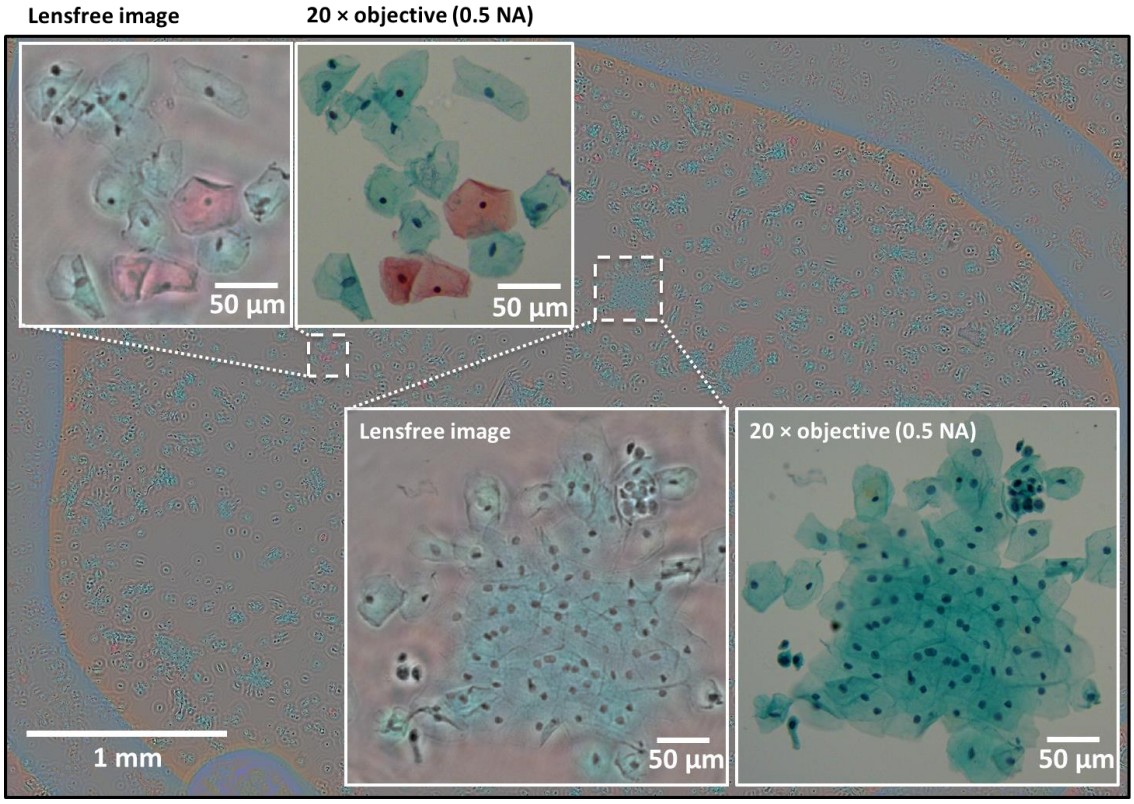


Figure 6.3 A wide FOV (~21 mm^2) lensfree color image of a Pap smear sample (ThinPrep® preparation). The Pap test was reconstructed using pixel super-resolved holograms acquired at four different heights (1069 µm, 1117 µm, 1159 µm and 1205 µm). For comparison purposes, 20× microscopes images (0.5 NA objective lens) of the same specimen are also provided.

To validate that our field-portable microscope can satisfy pathology needs, we specifically imaged some abnormal cells in a Pap smear as shown in Fig. 6.4 (marked by white arrows). A professional cytotechnologist confirmed the abnormality of these cells beforehand and the cells were imaged with our field-portable device. Abnormal cells have generally distinct spatial features such as a large nuclear-cytoplasmic ratio and/or an irregular cytoplasm shape. Figures 6.4(a) to (c) illustrate the lensfree color images obtained by our field-portable microscope using four different sample heights (i.e., 1069 μm, 1117 μm, 1159 μm and 1205 μm). These lensfree images shown in Figs. 6.4(a) to (c) agree very well with the corresponding 20× microscope objective (0.5 NA) images that are provided in Figs. 6.4(d) to (f), respectively, illustrating that our field-portable color microscope preserves the spatial features of interest within abnormal cells. Here we should also emphasize that this work does 'not' claim automated diagnosis of Pap smears and does 'not' aim to replace the pathologist or the cytotechnologist; but rather aims to create a field-portable and cost-effective high-throughput microscope that can provide decent quality and high-resolution color images of various specimen that can be used by professionals for e.g., tele-pathology and remote diagnostics purposes.

It is interesting to note that in this computational color microscope, while the usage of multiple heights offers superior twin image elimination, it also comes with the cost of partially degrading the spatial resolution of the image as well increasing the reconstruction time. Typically, the twin image noise is strong when the specimen is spatially dense and connected, and it gets weaker when the specimen is spatially sparse. Therefore, if sub-micron resolution is sufficient for a certain imaging application/need, the number of heights to be used in the multi-height phase-recovery process depends on the spatial density of the sample of interest. For samples that are spatially dense and/or require the investigation of fine features obscured by twin

image related artifacts (as in the case of Pap smear samples, see e.g., Fig. 6.3), the multi-height phase-recovery process might require more than two different heights in order to produce acceptable results and effectively eliminate the twin image noise. As a solution to this need, our field-portable color microscope offers the flexibility to acquire super-resolved holograms at any necessary number of sample heights, thus enabling computational color imaging of dense and connected specimen. Finally, we should emphasize that using a CMOS imager chip that has an even smaller pixel size (e.g., ~1.1 μm), a higher spatial resolution of ~ 300 nm can also be achieved using the same computational imaging technique[60,151].

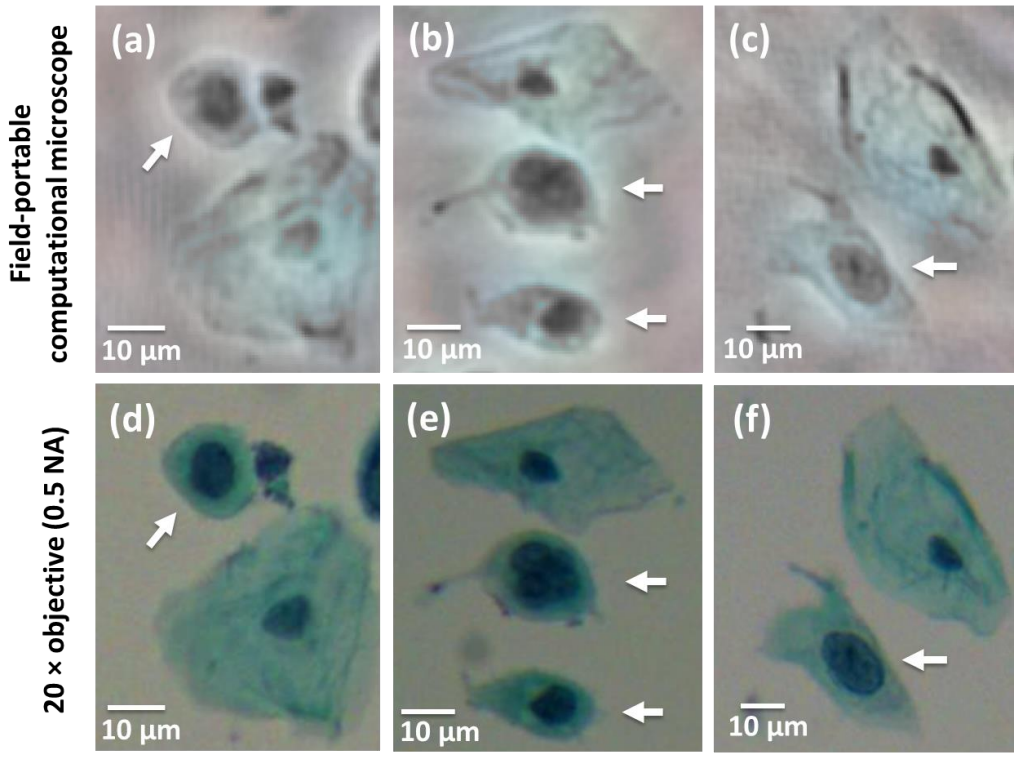


Figure 6.4 Lensfree computational images of abnormal cells in a Pap smear sample. **(a)**, **(b)** and **(c)** lensfree Pap smear images of abnormal cells (pointed by white arrows), which generally exhibit large nucleus in comparison to their cytoplasm as well as an irregular cytoplasm shape. **(d)**, **(e)** and **(f)** microscope comparison images for (a), (b) and (c), respectively, obtained using a 20× microscope objective (0.5 NA).

Chapter 7 Conclusions

Over the past three centuries, the bright field microscope has served as a valuable imaging tool for the scientific and medical community. Central to its success are the carefully crafted lenses that enable real time imaging with high resolution; nevertheless, the dependency on high quality lenses imposes fundamental limitations on the microscope's performance such as limited field-of-view, bulkiness and relatively high capital cost. To address these issues, several computational imaging approaches have emerged, which with the use of computational power, aim to replace the dependency of the microscope on lenses. In this dissertation I presented lensfree holographic microscopy, a promising method whose utilization enables the construction of portable, cost-effective and high-resolution microscopes with phenomenally wide field-of-view.

Reflecting back on my work, I can summarize my contributions to lensfree imaging in three main categorizes: (1) Resolution, I was able to improve the NA of lensfree imaging to 0.8 in air and 0.9 in oil. The quoted NA is equivalent to the NA of a high-quality 40 × objective lens. This improvement enables a wide range of applications that require high resolution in addition to high throughput. (2) Imaging confluent samples, since confluent samples deviate from in-line holography assumptions, imaging and reconstructing these samples using holographic lensfree microscopes is a convoluted problem. By utilizing and sophisticating phase-recovery algorithms, which were borrowed from coherent diffraction imaging, I was able to demonstrate that reconstruction of connected and dense tissue is feasible using lensfree holographic microscopes. This advancement opens many avenues especially in pathology slide imaging, where the sample preparation techniques are well established and modifications to the preparation techniques are not desirable. (3) Color, as coherent imaging system typically record images from one

illumination wavelength, the resulting image is gray scale by nature. Given the additive values of color, such as its importance for perception, in addition to its use in various applications, I attempted to develop a color lensfree holographic microscope. However, a straightforward combination of three illumination wavelength is not sufficient, as the resulting color image is typically corrupted by a spatial color noise. I addressed this problem by using a variety of colorization algorithms, and the resulting images exhibit accurate color reproduction.

The improvement in resolution, sample compatibility, and color advances lensfree imaging to a translational stage. In Chapter 5, I demonstrated that lensfree microscopes can image pathology slides and maintain the spatial features that are required for diagnostics purposes with a virtual depth-of-field experience that a typical bright field microscope cannot provide. This translational application demonstrates the potential of lensfree imaging to address real world problems in an elegant and cost-effective manner/way.

In the long run, I believe that these technological advances will afford complex computational methods to run in real-time on future cellphones or laptops, establishing lensfree microscopy as a powerful point-of-care imaging solution. Consequently, many avenues in the field of preventive medicine and telemedicine will then become significantly more accessible, presenting viable opportunities to reduce health care costs in the developed countries, and improve access to medical diagnostics in developing countries. As of today, lensfree imaging has already begun instigating commercial interest among small as well as large companies, who have formed partnerships to develop a lensfree imager for automated cell inspection systems. This illustrates the future commercial prospects of the method.

References

1. Garcia-Sucerquia, J., Xu, W., Jericho, M. H. & Kreuzer, H. J. Immersion digital in-line holographic microscopy. *Opt. Lett.* **31,** 1211–1213 (2006).

2. Garcia-Sucerquia, J. *et al.* Digital in-line holographic microscopy. *Appl. Opt.* **45,** 836–850 (2006).

3. Kanka, M., Riesenberg, R. & Kreuzer, H. J. Reconstruction of high-resolution holographic microscopic images. *Opt. Lett.* **34,** 1162–1164 (2009).

4. Kanka, M., Riesenberg, R., Petruck, P. & Graulig, C. High resolution (NA=0.8) in lensless in-line holographic microscopy with glass sample carriers. *Opt. Lett.* **36,** 3651–3653 (2011).

5. Mudanyali, O. *et al.* Compact, light-weight and cost-effective microscope based on lensless incoherent holography for telemedicine applications. *Lab Chip* **10,** 1417–1428 (2010).

6. Bishara, W., Su, T.-W., Coskun, A. F. & Ozcan, A. Lensfree on-chip microscopy over a wide field-of-view using pixel super-resolution. *Opt. Express* **18,** 11181–11191 (2010).

7. Bishara, W. *et al.* Holographic pixel super-resolution in portable lensless on-chip microscopy using a fiber-optic array. *Lab Chip* **11,** 1276–1279 (2011).

8. Bishara, W., Zhu, H. & Ozcan, A. Holographic opto-fluidic microscopy. *Opt. Express* **18,** 27499–27510 (2010).

9. Mudanyali, O., Bishara, W. & Ozcan, A. Lensfree super-resolution holographic microscopy using wetting films on a chip. *Opt. Express* **19,** 17378–17389 (2011).

10. Stybayeva, G. *et al.* Lensfree Holographic Imaging of Antibody Microarrays for High-Throughput Detection of Leukocyte Numbers and Function. *Anal. Chem.* **82,** 3736–3744 (2010).

11. Su, T.-W., Erlinger, A., Tseng, D. & Ozcan, A. Compact and Light-Weight Automated Semen Analysis Platform Using Lensfree on-Chip Microscopy. *Anal. Chem.* **82,** 8307–8312 (2010).

12. Isikman, S. O., Bishara, W., Zhu, H. & Ozcan, A. Optofluidic tomography on a chip. *Appl Phys Lett* **98,** 161109 (2011).

13. Brady, D. J., Choi, K., Marks, D. L., Horisaki, R. & Lim, S. Compressive Holography. *Opt. Express* **17,** 13040–13049 (2009).

14. Hahn, J., Lim, S., Choi, K., Horisaki, R. & Brady, D. J. Video-rate compressive holographic microscopic tomography. *Opt. Express* **19,** 7289–7298 (2011).

15. Lee, M., Yaglidere, O. & Ozcan, A. Field-portable reflection and transmission microscopy based on lensless holography. *Biomed. Opt. Express* **2,** 2721–2730 (2011).

16. Cui, X. *et al.* Lensless high-resolution on-chip optofluidic microscopes for Caenorhabditis elegans and cell imaging. *PNAS* **105,** 10670–10675 (2008).

17. Pang, S. *et al.* Implementation of a color-capable optofluidic microscope on a RGB CMOS color sensor chip substrate. *Lab on a Chip* **10,** 411–414 (2010).

18. Zheng, G., Lee, S. A., Antebi, Y., Elowitz, M. B. & Yang, C. The ePetri dish, an on-chip cell imaging platform based on subpixel perspective sweeping microscopy (SPSM). *PNAS* **108,** 16889–16894 (2011).

19. Lee, S. A. *et al.* Color Capable Sub-Pixel Resolving Optofluidic Microscope and Its Application to Blood Cell Imaging for Malaria Diagnosis. *PLoS ONE* **6,** e26127 (2011).

20. Maiden, A. M., Humphry, M. J., Zhang, F. & Rodenburg, J. M. Superresolution imaging via ptychography. *J. Opt. Soc. Am. A* **28,** 604–612 (2011).

21. Maiden, A. M., Rodenburg, J. M. & Humphry, M. J. Optical ptychography: a practical implementation with useful resolution. *Opt. Lett.* **35,** 2585–2587 (2010).

22. Martínez-León, L. & Javidi, B. Synthetic aperture single-exposure on-axis digital holography. *Opt. Express* **16,** 161–169 (2008).

23. Kikuchi, Y., Barada, D., Kiire, T. & Yatagai, T. Doppler phase-shifting digital holography and its application to surface shape measurement. *Opt. Lett.* **35,** 1548–1550 (2010).

24. Greenbaum, A., Sikora, U. & Ozcan, A. Field-portable wide-field microscopy of dense samples using multi-height pixel super-resolution based lensfree imaging. *Lab Chip* **12,** 1242–1245 (2012).

25. Isikman, S. O. *et al.* Lens-free optical tomographic microscope with a large imaging volume on a chip. *Proceedings of the National Academy of Sciences* **108,** 7296–7301 (2011).

26. Coskun, A. F., Sencan, I., Su, T.-W. & Ozcan, A. Lensless wide-field fluorescent imaging on a chip using compressive decoding of sparse objects. *Opt. Express* **18,** 10510–10523 (2010).

27. Coskun, A. F., Sencan, I., Su, T.-W. & Ozcan, A. Wide-field lensless fluorescent microscopy using a tapered fiber-optic faceplate on a chip. *Analyst* **136,** 3512–3518 (2011).

28. Pang, S., Han, C., Lee, L. M. & Yang, C. Fluorescence microscopy imaging with a Fresnel zone plate array based optofluidic microscope. *Lab Chip* **11,** 3698–3702 (2011).

29. Coskun, A. F., Sencan, I., Su, T.-W. & Ozcan, A. Lensfree fluorescent on-chip imaging of transgenic Caenorhabditis elegans over an ultra-wide field-of-view. *PLoS ONE* **6,** e15955 (2011).

30. Chapman, H. N. & Nugent, K. A. Coherent lensless X-ray imaging. *Nat Photon* **4,** 833–839 (2010).

31. Nugent, K. A. Coherent methods in the X-ray sciences. *Advances in Physics* **59,** 1–99 (2009).

32. Abbey, B. *et al.* Lensless imaging using broadband X-ray sources. *Nat Photon* **5,** 420–424 (2011).

33. Miao, J., Kirz, J. & Sayre, D. The oversampling phasing method. *Acta Crystallographica Section D Biological Crystallography* **56,** 1312–1315 (2000).

34. Chen, C.-C., Miao, J., Wang, C. W. & Lee, T. K. Application of optimization technique to noncrystalline x-ray diffraction microscopy: Guided hybrid input-output method. *Phys. Rev. B* **76,** 064113 (2007).

35. Humphry, M. J., Kraus, B., Hurst, A. C., Maiden, A. M. & Rodenburg, J. M. Ptychographic electron microscopy using high-angle dark-field scattering for sub-nanometre resolution imaging. *Nature Communications* **3,** 730 (2012).

36. Szameit, A. *et al.* Sparsity-based single-shot subwavelength coherent diffractive imaging. *Nature Materials* **11,** 455–459 (2012).

37. Thibault, P. & University, C. *Algorithmic methods in diffraction microscopy*. (Cornell University, 2007).

38. Miao, J., Sayre, D. & Chapman, H. N. Phase retrieval from the magnitude of the Fourier transforms of nonperiodic objects. *Journal of the Optical Society of America A* **15,** 1662 (1998).

39. Millane, R. P. Phase retrieval in crystallography and optics. *Journal of the Optical Society of America A* **7,** 394 (1990).

40. Allen, L. J. & Oxley, M. P. Phase retrieval from series of images obtained by defocus variation. *Optics Communications* **199,** 65–75 (2001).

41. Zhang, F., Pedrini, G. & Osten, W. Phase retrieval of arbitrary complex-valued fields through aperture-plane modulation. *Phys. Rev. A* **75,** 043805 (2007).

42. Repetto, L., Piano, E. & Pontiggia, C. Lensless digital holographic microscope with light-emitting diode illumination. *Opt. Lett.* **29,** 1132–1134 (2004).

43. Dubois, F., Joannes, L. & Legros, J.-C. Improved Three-Dimensional Imaging with a Digital Holography Microscope With a Source of Partial Spatial Coherence. *Appl. Opt.* **38,** 7085–7094 (1999).

44. Sung Cheol Park, Min Kyu Park & Moon Gi Kang. Super-resolution image reconstruction: a technical overview. *IEEE Signal Processing Magazine* **20,** 21– 36 (2003).

45. Hardie, R. C., Barnard, K. J., Bognar, J. G., Armstrong, E. E. & Watson, E. A. High-resolution image reconstruction from a sequence of rotated and translated frames and its application to an infrared imaging system. *Optical Engineering* **37,** 247–260 (1998).

46. Elad, M. & Hel-Or, Y. A fast super-resolution reconstruction algorithm for pure translational motion and common space-invariant blur. *IEEE Transactions on Image Processing* **10,** 1187–1193 (2001).

47. Fienup, J. R. Phase retrieval algorithms: a comparison. *Appl. Opt.* **21,** 2758–2769 (1982).

48. Denis, L., Fournier, C., Fournel, T. & Ducottet, C. Numerical suppression of the twin image in in-line holography of a volume of micro-objects. *Meas. Sci. Technol.* **19,** 074004 (2008).

49. Charrière, F. *et al.* Living specimen tomography by digital holographic microscopy: morphometry of testate amoeba. *Opt. Express* **14,** 7005–7013 (2006).

50. Dierolf, M. *et al.* Ptychographic X-ray computed tomography at the nanoscale. *Nature* **467,** 436–439 (2010).

51. Rivenson, Y., Stern, A. & Javidi, B. Compressive Fresnel holography. *J. Display Technol.* **6,** 506–509 (2010).

52. Saini, A. New lens offers scientist a brighter outlook. *Science* **335,** 1562–1563 (2012).

53. Srigunapalan, S., Eydelnant, I. A., Simmons, C. A. & Wheeler, A. R. A digital microfluidic platform for primary cell culture and analysis. *Lab on a Chip* **12,** 369–375 (2012).

54. Schnars, U. & Jüptner, W. P. O. Digital recording and numerical reconstruction of holograms. *Measurement Science and Technology* **13,** R85–R101 (2002).

55. Greenbaum, A., Feizi, A., Akbari, N. & Ozcan, A. Wide-field computational color imaging using pixel super-resolved on-chip microscopy. *Opt. Express* **21,** 12469–12483 (2013).

56. Cuche, E., Marquet, P. & Depeursinge, C. Spatial filtering for zero-order and twin-image elimination in digital off-axis holography. *Appl. Opt.* **39,** 4070–4075 (2000).

57. Khademhosseinieh, B. *et al.* Lensfree on-chip imaging using nanostructured surfaces. *Applied Physics Letters* **96,** 171106–171106–3 (2010).

58. Shimobaba, T. *et al.* Computational wave optics library for C++: CWO++ library. *Computer Physics Communications* **183,** 1124–1138 (2012).

59. Trelles, O., Prins, P., Snir, M. & Jansen, R. C. Big data, but are we ready? *Nature Reviews Genetics* **12,** 224–224 (2011).

60. Greenbaum, A. *et al.* Imaging without lenses: achievements and remaining challenges of wide-field on-chip microscopy. *Nat Meth* **9,** 889–895 (2012).

61. Mudanyali, O. *et al.* Wide-field optical detection of nanoparticles using on-chip microscopy and self-assembled nanolenses. *Nat Photon* **7,** 247–254 (2013).

62. Mudanyali, O., Oztoprak, C., Tseng, D., Erlinger, A. & Ozcan, A. Detection of waterborne parasites using field-portable and cost-effective lensfree microscopy. *Lab Chip* **10,** 2419–2423 (2010).

63. Pelagotti, A. *et al.* An automatic method for assembling a large synthetic aperture digital hologram. *Opt Express* **20,** 4830–4839 (2012).

64. Biggs, D. S. C. & Andrews, M. Acceleration of iterative image restoration algorithms. *Appl. Opt.* **36,** 1766–1775 (1997).

65. Holmes, T. J. Blind deconvolution of quantum-limited incoherent imagery: maximum-likelihood approach. *J. Opt. Soc. Am. A* **9,** 1052–1061 (1992).

66. Levin, A., Weiss, Y., Durand, F. & Freeman, W. T. Understanding and evaluating blind deconvolution algorithms. in *IEEE Conference on Computer Vision and Pattern Recognition, 2009. CVPR 2009* 1964 –1971 (2009).

67. Meisenzahl, E. J. *et al.* 3.2-million-pixel full-frame true 2-phase CCD image sensor incorporating transparent gate technology. *Proc. SPIE* **3965,** 92–100 (2000).

68. Meisenzahl, E. J. *et al.* 31 Mp and 39 Mp full-frame CCD image sensors with improved charge capacity and angle response. *Proc. SPIE* **6069,** 606902 (2006).

69. Fontaine, R. Recent innovations in CMOS image sensors. in *Advanced Semiconductor Manufacturing Conference (ASMC), 2011 22nd Annual IEEE/SEMI* 1 –5 (2011).

70. Gorocs, Z. & Ozcan, A. On-chip biomedical imaging. *Biomedical Engineering, IEEE Reviews in* **6,** 29–46 (2013).

71. Delen, N. & Hooker, B. Free-space beam propagation between arbitrarily oriented planes based on full diffraction theory: a fast Fourier transform approach. *Journal of the Optical Society of America A* **15,** 857 (1998).

72. Goodman, J. W. *Introduction to Fourier Optics*. (Roberts &Company Publishers, 2005).

73. Isikman, S. O., Greenbaum, A., Luo, W., Coskun, A. F. & Ozcan, A. Giga-pixel lensfree holographic microscopy and tomography using color image sensors. *PLoS ONE* **7,** e45044 (2012).

74. Gonzalez, R. C. *Digital image processing*. (Prentice Hall, 2008).

75. Fienup, J. R. Reconstruction of an object from the modulus of its Fourier transform. *Opt. Lett.* **3,** 27–29 (1978).

76. Koren, G., Polack, F. & Joyeux, D. Iterative algorithms for twin-image elimination in in-line holography using finite-support constraints. *J. Opt. Soc. Am. A* **10,** 423–433 (1993).

77. Pech-Pacheco, J. L., Cristóbal, G., Chamorro-Martínez, J. & Fernández-Valdivia, J. Diatom autofocusing in brightfield microscopy: a comparative study. in *Pattern Recognition, International Conference on* **3,** 3318 (IEEE Computer Society, 2000).

78. Fremont-Smith, M., Marino, J., Griffin, B., Spencer, L. & Bolick, D. Comparison of the Surepath^{TM} liquid-based Papanicolaou smear with the conventional Papanicolaou smear in a multisite direct-to-vial study. *Cancer Cytopathology* **102,** 269–279 (2004).

79. Isikman, S. O. *et al.* Color and monochrome lensless on-chip imaging of Caenorhabditis elegans over a wide field-of-view. *Lab Chip* **10,** 1109 (2010).

80. Elser, V. Phase retrieval by iterated projections. *J. Opt. Soc. Am. A* **20,** 40–55 (2003).

81. Faulkner, H. M. L. & Rodenburg, J. M. Movable aperture lensless transmission microscopy: a novel phase retrieval algorithm. *Phys. Rev. Lett.* **93,** 023903 (2004).

82. Waller, L., Tian, L. & Barbastathis, G. Transport of Intensity phase-amplitude imaging with higher order intensity derivatives. *Opt. Express* **18,** 12552–12561 (2010).

83. Paganin, D., Barty, A., McMahon, P. J. & Nugent, K. A. Quantitative phase-amplitude microscopy. III. The effects of noise. *Journal of Microscopy* **214,** 51–61 (2004).

84. Marchesini, S. A unified evaluation of iterative projection algorithms for phase retrieval. *Rev. Sci. Instrum.* **78,** 011301 (2007).

85. Latychevskaia, T. & Fink, H.-W. Solution to the twin image problem in holography. *Phys. Rev. Lett.* **98,** 233901 (2007).

86. Fienup, J. R. & Wackerman, C. C. Phase-retrieval stagnation problems and solutions. *J. Opt. Soc. Am. A* **3,** 1897–1907 (1986).

87. Oh, C., Isikman, S. O., Khademhosseinieh, B. & Ozcan, A. On-chip differential interference contrast microscopy using lensless digital holography. *Opt. Express* **18,** 4717–4726 (2010).

88. Fienup, J. R. & Kowalczyk, A. M. Phase retrieval for a complex-valued object by using a low-resolution image. *J. Opt. Soc. Am. A* **7,** 450–458 (1990).

89. Biener, G. *et al.* Combined reflection and transmission microscope for telemedicine applications in field settings. *Lab Chip* **11,** 2738–2743 (2011).

90. Crimmins, T. R., Fienup, J. R. & Thelen, B. J. Improved bounds on object support from autocorrelation support and application to phase retrieval. *J. Opt. Soc. Am. A* **7,** 3–13 (1990).

91. Paganin, D. & Nugent, K. A. Noninterferometric phase imaging with partially coherent light. *Phys. Rev. Lett.* **80,** 2586 (1998).

92. Zysk, A. M., Schoonover, R. W., Carney, P. S. & Anastasio, M. A. Transport of intensity and spectrum for partially coherent fields. *Opt Lett* **35,** 2239–2241 (2010).

93. Gerchberg, R. W. & Saxton, W. O. A practical algorithm for the determination of phase from image and diffraction plane pictures. *OPTIK* **35,** 237–246 (1971).

94. Zhang, Y., Pedrini, G., Osten, W. & Tiziani, H. J. Reconstruction of in-line digital holograms from two intensity measurements. *Opt. Lett.* **29,** 1787–1789 (2004).

95. Das, B. & Yelleswarapu, C. S. Dual plane in-line digital holographic microscopy. *Opt. Lett.* **35,** 3426–3428 (2010).

96. Paxman, R. G., Schulz, T. J. & Fienup, J. R. Joint estimation of object and aberrations by using phase diversity. *J. Opt. Soc. Am. A* **9,** 1072–1085 (1992).

97. Vogel, C., Chan, T. & Plemmons, R. Fast algorithms for phase diversity-based blind deconvolution. *Proc. SPIE* **3353,** 994–1005 (1998).

98. Noort, M., Voort, L. R. V. & Löfdahl, M. G. Solar image restoration by use of multi-frame blind de-convolution with multiple objects and phase diversity. *Solar Physics* **228,** 191–215 (2005).

99. Ferraro, P. *et al.* Full color 3-D imaging by digital holography and removal of chromatic aberrations. *J. Display Technol.* **4,** 97–100 (2008).

100. Javidi, B. *et al.* Three-dimensional image fusion by use of multiwavelength digital holography. *Opt. Lett.* **30,** 144–146 (2005).

101. Yamaguchi, I., Matsumura, T. & Kato, J. Phase-shifting color digital holography. *Opt. Lett.* **27,** 1108–1110 (2002).

102. Kato, J., Yamaguchi, I. & Matsumura, T. Multicolor digital holography with an achromatic phase shifter. *Opt. Lett.* **27,** 1403–1405 (2002).

103. Garcia-Sucerquia, J. Color lensless digital holographic microscopy with micrometer resolution. *Opt. Lett.* **37,** 1724–1726 (2012).

104. Göröcs, Z., Orzó, L., Kiss, M., Tóth, V. & Tőkés, S. In-line color digital holographic microscope for water quality measurements. *Proc. SPIE* **7376,** 737614 (2010).

105. Xia, P. *et al.* Improvement of color reproduction in color digital holography by using spectral estimation technique. *Appl Opt* **50,** H177–182 (2011).

106. Jack, K. *Video Demystified: A Handbook for the Digital Engineer*. (Elsevier, 2011).

107. Dijkstra, E. W. A note on two problems in connexion with graphs. *NUMER MATH* **1,** 269–271 (1959).

108. Yatziv, L. & Sapiro, G. Fast image and video colorization using chrominance blending. *IEEE Transactions on Image Processing* **15,** 1120–1129 (May).

109. Ahuja, R. K., Mehlhorn, K., Orlin, J. & Tarjan, R. E. Faster algorithms for the shortest path problem. *J. ACM* **37,** 213–223 (1990).

110. Greenbaum, A. & Ozcan, A. Maskless imaging of dense samples using pixel super-resolution based multi-height lensfree on-chip microscopy. *Opt. Express* **20,** 3129–3143 (2012).

111. Almoro, P., Pedrini, G. & Osten, W. Complete wavefront reconstruction using sequential intensity measurements of a volume speckle field. *Appl. Opt.* **45,** 8596–8605 (2006).

112. Zhang, Y., Pedrini, G., Osten, W. & Tiziani, H. Whole optical wave field reconstruction from double or multi in-line holograms by phase retrieval algorithm. *Opt. Express* **11,** 3234–3241 (2003).

113. Schiffman, M., Castle, P. E., Jeronimo, J., Rodriguez, A. C. & Wacholder, S. Human papillomavirus and cervical cancer. *The Lancet* **370,** 890–907 (2007).

114. Levin, A., Lischinski, D. & Weiss, Y. Colorization using optimization. *ACM Trans. Graph.* **23,** 689–694 (2004).

115. Duggan, M. A., Khalil, M., Brasher, P. M. A. & Nation, J. G. Comparative study of the ThinPrep Pap test and conventional cytology results in a Canadian cohort. *Cytopathology* **17,** 73–81 (2006).

116. DeMay, R. M. *The pap test*. (ASCP Press, 2005).

117. C. R. Kjeldsberg & S. L. Perkins. *Practical diagnosis of hematologic disorders*. (ASCP Press, 1989).

118. Mills, S. E. *Histology for pathologists*. (Wolters Kluwer Health/Lippincott Williams & Wilkins, 2012).

119. Baker, J. J. Conventional and liquid-based cervicovaginal cytology: A comparison study with clinical and histologic follow-up. *Diagnostic Cytopathology* **27,** 185–188 (2002).

120. Bain, B. J. Diagnosis from the blood smear. *New England Journal of Medicine* **353,** 498–507 (2005).

121. Allen, L. J., McBride, W., O'Leary, N. L. & Oxley, M. P. Exit wave reconstruction at atomic resolution. *Ultramicroscopy* **100,** 91–104 (2004).

122. Anand, A. & Javidi, B. Three-dimensional microscopy with single-beam wavefront sensing and reconstruction from speckle fields. *Opt. Lett.* **35,** 766–768 (2010).

123. Reed Teague, M. Deterministic phase retrieval: a Green's function solution. *J. Opt. Soc. Am.* **73,** 1434–1441 (1983).

124. Greenbaum, A., Akbari, N., Feizi, A., Luo, W. & Ozcan, A. Field-portable pixel super-resolution colour microscope. *PLoS ONE* **8,** e76475 (2013).

125. De Nicola, S., Finizio, A., Pierattini, G., Ferraro, P. & Alfieri, D. Angular spectrum method with correction of anamorphism for numerical reconstruction of digital holograms on tilted planes. *Opt. Express* **13,** 9935–9940 (2005).

126. Jeong, S. J. & Hong, C. K. Pixel-size-maintained image reconstruction of digital holograms on arbitrarily tilted planes by the angular spectrum method. *Applied Optics* **47,** 3064 (2008).

127. Matsushima, K. Formulation of the rotational transformation of wave fields and their application to digital holography. *Appl. Opt.* **47,** D110–D116 (2008).

128. Goodman, J. W. *Statistical optics*. (Wiley, 2000).

129. Ozcan, A. Educational games for Malaria diagnosis. *Sci Transl Med* **6,** 233ed9–233ed9 (2014).

130. Johnson, C. *Numerical solution of partial differential equations by the finite element method*. (Dover Publications, 2009).

131. Gorthi, S. S. & Schonbrun, E. Phase imaging flow cytometry using a focus-stack collecting microscope. *Opt. Lett.* **37,** 707–709 (2012).

132. Matsushima, K., Schimmel, H. & Wyrowski, F. Fast calculation method for optical diffraction on tilted planes by use of the angular spectrum of plane waves. *J. Opt. Soc. Am. A* **20,** 1755–1762 (2003).

133. Wang, J. Electrochemical biosensors: Towards point-of-care cancer diagnostics. *Biosensors and Bioelectronics* **21,** 1887–1892 (2006).

134. Myers, F. B. & Lee, L. P. Innovations in optical microfluidic technologies for point-of-care diagnostics. *Lab Chip* **8,** 2015–2031 (2008).

135. Ramachandraiah, H. *et al.* Lab-on-DVD: standard DVD drives as a novel laser scanning microscope for image based point of care diagnostics. *Lab Chip* **13,** 1578–1585 (2013).

136. Gallegos, D. *et al.* Label-free biodetection using a smartphone. *Lab Chip* **13,** 2124–2132 (2013).

137. Kim, S. B. *et al.* A cell-based biosensor for real-time detection of cardiotoxicity using lensfree imaging. *Lab on a Chip* **11,** 1801 (2011).

138. Breslauer, D. N., Maamari, R. N., Switz, N. A., Lam, W. A. & Fletcher, D. A. Mobile phone based clinical microscopy for global health applications. *PLoS ONE* **4,** e6320 (2009).

139. Zhu, H., Isikman, S. O., Mudanyali, O., Greenbaum, A. & Ozcan, A. Optical imaging techniques for point-of-care diagnostics. *Lab Chip* **13,** 51–67 (2012).

140. Martinez, A. W. *et al.* Simple telemedicine for developing regions: camera phones and paper-based microfluidic devices for real-time, off-site diagnosis. *Anal. Chem.* **80,** 3699–3707 (2008).

141. Pamplona, V. F. *et al.* CATRA: interactive measuring and modeling of cataracts. *ACM Trans. Graph.* **30,** 1–8 (2011).

142. Kumar, K., Hoshino, K. & Zhang, X. Handheld subcellular-resolution single-fiber confocal microscope using high-reflectivity two-axis vertical combdrive silicon microscanner. *Biomed Microdevices* **10,** 653–660 (2008).

143. Zhu, H., Mavandadi, S., Coskun, A. F., Yaglidere, O. & Ozcan, A. Optofluidic fluorescent imaging cytometry on a cell phone. *Anal Chem* **83,** 6641–6647 (2011).

144. Iftimia, N. V. *et al.* A portable, low coherence interferometry based instrument for fine needle aspiration biopsy guidance. *Review of Scientific Instruments* **76,** 064301–064306 (2005).

145. Goldberg, B. D., Motaghian Nezam, S. M. R., Jillella, P., Bouma, B. E. & Tearney, G. J. Miniature swept source for point of care optical frequency domain imaging. *Opt. Express* **17,** 3619–3629 (2009).

146. Ghosh, K. K. *et al.* Miniaturized integration of a fluorescence microscope. *Nat. Methods* **8,** 871–878 (2011).

147. Miller, A. R. *et al.* Portable, battery-operated, low-cost, bright field and fluorescence microscope. *PLoS ONE* **5,** e11890 (2010).

148. Zhu, H., Yaglidere, O., Su, T.-W., Tseng, D. & Ozcan, A. Cost-effective and compact wide-field fluorescent imaging on a cell-phone. *Lab Chip* **11,** 315–322 (2010).

149. Balsam, J., Ossandon, M., Kostov, Y., Bruck, H. A. & Rasooly, A. Lensless CCD-based fluorometer using a micromachined optical Söller collimator. *Lab Chip* **11,** 941–949 (2011).

150. McLeod, E., Luo, W., Mudanyali, O., Greenbaum, A. & Ozcan, A. Toward giga-pixel nanoscopy on a chip: a computational wide-field look at the nano-scale without the use of lenses. *Lab on a Chip* **13,** 2028–2035 (2013).

151. Greenbaum, A. *et al.* Increased space-bandwidth product in pixel super-resolved lensfree on-chip microscopy. *Sci. Rep.* **3,** 1717 (2013).